Lipidomic profiling reveals age-dependent changes in plasma membrane lipids that impact neural stem cell aging

Xiaoai Zhao[1,2,3,4,*], Ryan M. Feitzinger[1,14], Jeeyoon Na[1,5,14], Xin Yan[6,7,14], Andrew Erickson[2,3,4,14], Kévin Contrepois[1,14], Olivia Y. Zhou[1,8,9], Francesco Vallania[10,11], Mathew Ellenberger[1], Chloe M. Kashiwagi[1], Stephanie D. Gagnon[1], Cynthia J. Siebrand[1], Matias Cabruja[1], Gavin M. Traber[1], Andrew McKay[1], Daniel Hornburg[1], Purvesh Khatri[10,11], Michael P. Snyder[1,15], Richard N. Zare[5,15] and Anne Brunet[1,12,13,*]

[1]Department of Genetics, Stanford University, CA, USA
[2]Present address: Department of Comparative Medicine, Yale University, CT, USA
[3]Present address: Yale Center for Molecular and Systems Metabolism, Yale University, CT, USA
[4]Present address: Wu Tsai Institute, Yale University, CT, USA
[5]Institute for Stem Cell Biology and Regenerative Medicine, Stanford University, CA, USA
[6]Department of Chemistry, Stanford University, CA, USA
[7]Present address: Department of Chemistry, Texas A&M University, TX, USA
[8]Stanford Biophysics Program, Stanford University, Stanford, CA, USA
[9]Stanford Medical Scientist Training Program, Stanford University, Stanford, CA, USA
[10]Institute for Immunity, Transplantation and Infection, Stanford University, Stanford, CA, USA
[11]Stanford Center for Biomedical Informatics Research, Stanford University, CA, USA
[12]Glenn Laboratories for the Biology of Aging, Stanford University, CA, USA
[13]Wu Tsai Neurosciences Institute, Stanford University, CA, USA
[14]These authors contributed equally
[15]These authors contributed equally
*Corresponding authors: abrunet1@stanford.edu, xiaoai.zhao@yale.edu

Abstract

The aging brain exhibits a decline in the regenerative populations of neural stem cells (NSCs), which may underlie age-associated defects in sensory and cognitive functions (*1-6*). While mechanisms that restore old NSC function have started to be identified (*7-27*), the role of lipids – especially complex lipids – in NSC aging remains largely unclear. Using lipidomic profiling by mass spectrometry, we identify age-related lipidomic changes in quiescent NSCs *in vitro* and *in vivo*. These lipidomic analyses reveal remodeling of many membrane lipids, notably phospholipids, in old NSCs. Moreover, several poly-unsaturated fatty acids (PUFAs) increase across lipid classes in quiescent NSCs during aging. Using spatial lipidomics, we find that some of the changes in phospholipids are also observed *in situ* in intact tissues. Several age-related changes in complex lipids and side chain composition are occurring at the plasma membrane, as revealed by lipidomic profiling of isolated plasma membrane vesicles. Experimentally, we find that aging is accompanied by a decrease in plasma membrane order, a key membrane biophysical property, in old quiescent NSCs *in vitro* and *in vivo*. To determine the functional role of plasma membrane lipids in aging NSCs, we performed genetic and supplementation studies. Knockout of *Mboat2*, which encodes a phospholipid acyltransferase, exacerbates age-related lipidomic changes in old quiescent NSCs and impedes their ability to activate. Interestingly, *Mboat2* overexpression reverses age-related lipidomic changes in old quiescent NSCs and boosts their ability to activate *in vitro* and *in vivo*. Moreover, supplementation of plasma membrane lipids derived from young NSCs improves the ability of old quiescent NSCs to activate. Our work could lead to lipid-based strategies for restoring the regenerative potential of NSCs in old individuals, which has important implications for countering brain decline during aging.

Main text

Lipids are extremely diverse, yet our understanding of lipid function is lagging. Complex lipids – lipids containing additional chemical moieties linked to fatty acids (e.g. phospholipids) – are key components of plasma and organelle membranes (*28-31*). Complex lipids serve critical barrier function and play important roles in organellar homeostasis and signal transduction (*28-31*). Lipid dysregulation has been observed during brain aging and in neurodegenerative diseases such as Alzheimer's disease (*32-44*). Age-associated changes in the lipidome have also been identified in several other organs (*45-47*). But the role of complex lipids in cells in the brain – and other organs – during aging is largely unknown.

The adult mammalian brain contains populations of neural stem cells (NSCs) that can generate neurons, astrocytes, and oligodendrocytes (*1, 2, 48-52*). NSCs are organized in two main niches – the dentate gyrus of the hippocampus and the subventricular zone (*50, 51, 53-56*). During aging, the ability of NSCs to transition from quiescence to activation declines (*15, 57-64*), and this deterioration could underlie defects in aspects of cognitive and sensory function (*1, 2, 65, 66*) as well as impaired injury repair in old individuals (*67-70*). Understanding how to maintain NSC regenerative potential during aging could identify strategies to counter age-related decline and facilitate repair after injury in the central nervous system. While lipid energy metabolism has been shown to be important for NSCs and other cells (*71-83*), the contribution of complex lipids to cell function during aging has not been well studied. More generally, a systematic examination of the global lipidome of mammalian cells during aging is still missing.

Lipidomics reveals remodeling of several membrane lipids in old quiescent NSCs (qNSCs) *in vitro*

To unbiasedly determine the age-related changes in complex lipids, we performed untargeted lipidomic profiling of NSCs from young and old mice *in vitro* and *in vivo*. Using liquid chromatography followed by tandem mass spectrometry (LC-MS/MS), we profiled quiescent and activated NSCs (qNSCs and aNSCs) cultured from young (3-5 months) and old (20-22 months) male mice (**Fig. 1A, "*In vitro* #1"**). We performed LC-MS/MS experiments on n=4-5 primary NSC cultures per age group (each derived from an individual mouse) using 14 internal standards (**Fig. 1A, Table S1**). This LC-MS/MS dataset detected 367 unique lipids in aNSCs and in qNSCs, covering all major lipid classes – phospholipids (e.g. phosphatidylcholine [PC], phosphatidylethanolamine [PE]), sphingolipids, triglycerides, cholesterol (**fig. S1, A and B, Table S3**). Principal component analysis (PCA) on the lipidomes showed good separation between qNSCs and aNSCs (**Fig. 1B**) as well as some separation between ages for qNSCs (but not aNSCs) (**Fig. 1C**). We therefore focused the rest of the manuscript on the differences in lipids with age in qNSCs. The lipid composition of young and old qNSCs was generally similar at the lipid class level (including cholesterol) (**fig. S1A**), but several individual lipids significantly changed with age in qNSCs (FDR-adjusted $P<0.1$) – including many membrane lipids (e.g. PC, PE, sphingomyelin) (**Fig. 1D**).

To characterize lipids that consistently change with age across experiments, we generated an independent LC-MS/MS dataset on n=4 young (3-5 months) and n=4 old (20-22 months) primary qNSC cultures using 13 internal standards (**Fig. 1A, "*In vitro* #2" [also used in Figure 4], Table S1 and S3**). This dataset showed similar lipid class composition (except for cholesterol, due to the lack of quantitative cholesterol standard in this experiment, see Methods)

(**fig. S1C**). This experiment detected 259 lipids, and 175 of them overlapped with the first *in vitro* experiment (**fig. S1B**). Importantly, more than 90% of the molar content of the samples was represented by lipids measured in both experiments (**fig. S1B**). Among the lipids that overlapped between both datasets, lipid concentrations were strongly correlated both in young (R=0.91, P<2.2e^{-16}) and old (R=0.9, P<2.2e^{-16}) qNSCs (**fig. S1D**, **Table S3**). Moreover, PCA revealed that age-related changes in qNSCs were consistent in direction across both datasets for lipids that overlapped between the two experiments (**fig. S1E**). We identify 92 lipids that commonly increased with age and 37 lipids that commonly decreased with age in both *in vitro* experiments (**fig. S1B**). There was some variability between experiments, likely reflecting differences in primary cell cultures, cohorts of aging mice, and experimental design (see Methods).

To identify lipids that robustly change with age in qNSCs across both datasets, we calculated effect size (i.e. differences between the group means of young and old samples divided by the pooled standard deviation, with 95% confidence interval and multiple hypothesis correction, see Methods). This type of approach has been used for comparisons across datasets, including lipidomic and metabolomic datasets (*84-86*). Several membrane lipids showed a consistent and significant increase (e.g. PE(P–18:0_18:1) and PE(18:1_20:4)) or decrease with age (e.g. PC(16:0_20:3) and PC(16:0_22:5)) in qNSCs across both *in vitro* datasets (FDR-adjusted P<0.05) (**Fig. 1E, fig. S1F, fig. S3 and Table S3**). Some of these lipids (e.g. PE(18:1_20:4)) were of high abundance, constituting more than 1% of the total lipid molar concentration (**fig. S1G**). Thus, several membrane lipids in qNSCs, including relatively abundant ones, are consistently remodeled with age.

Changes in lipid side chain composition with age in quiescent NSCs *in vitro*

Complex lipids are comprised of one or more fatty acyl side chains, and side chain carbon chain length, degree of unsaturation, and linkage type all contribute to biophysical properties, especially in membranes (*28, 30*). For each lipid class, we quantified the abundance of each unique fatty acyl side chains *in vitro*. The molar concentration of lipids containing a given side chain of each lipid class was strongly correlated in young and old qNSCs across *in vitro* LC-MS/MS datasets (R=0.95, P<2.2e^{-16} in young and R=0.94, P<2.2e^{-16} in old, **fig. S4A**).

Effect size calculation showed that several highly-unsaturated PUFA-containing side chains (e.g. phosphatidylcholine and phosphatidylinositol containing eicosapentaenoic acid [PC(20:5), PI(20:5)] or arachidonic acid [PI(20:4), PE(20:4)]) consistently increased with age in both *in vitro* datasets, whereas phospholipids containing less unsaturated PUFAs (e.g. PC(19:3), PC(21:3)) consistently decreased with age (**Fig. 1F**, **fig. S4B**). We also detected age-related changes in lipids containing monounsaturated fatty acid (MUFA) and saturated fatty acid (SFA) side chains (**Fig. 1F**, **fig. S4B**). Some features that exhibit significant change with age were among side chains that have the highest concentration in cells (e.g. PE(20:4), PI(20:4)), while others such as PI(20:5) and PE(20:5) were less abundant (**fig. S4C**). Hence, qNSCs also show several age-related changes in the composition of membrane-lipid fatty acyl side chains *in vitro*.

Lipidomic analysis shows remodeling of membrane lipids in old qNSCs *in vivo*

Could some of the lipid changes identified in qNSCs *in vitro* be detected *in vivo*? We performed lipidomic profiling on qNSCs freshly isolated by fluorescence-activated cell sorting (FACS) from the subventricular zone (SVZ) neurogenic niche of young (3-5 months) and old (20-22 months) mice (*14, 15, 87*) (**Fig. 1G, fig. S5** for the FACS gating strategy, **Tables S1 and S5**). As qNSCs are relatively rare in the mouse brain (~1,500 per mouse), we pooled cells from five mice

to obtain ~9,000 qNSCs for each of the n=6 biological replicates per age group and we performed untargeted lipidomics using LC-MS/MS with 14 internal standards (**Fig. 1G**). We identified 29 lipids in qNSCs freshly isolated from the brain, encompassing the major lipid classes identified in qNSC primary cultures (there were more lysophosphatidylethanolamine (LPE) lipids detected *in vivo*, perhaps due to systemic influences *in vivo* that are not present *in vitro*) (**fig. S6A, S2B**). Only 15 of these detected lipids overlapped between *in vivo* and *in vitro* datasets (6 increasing with age and 2 decreasing with age) (**fig. S6B**). Moreover, *in vivo* detected lipids only represent ~30% of the molar content of the *in vitro* samples (**fig. S6B**), likely due to the low starting material. Nevertheless, among the lipids that overlapped between *in vitro* and *in vivo* datasets, lipid concentrations were strongly correlated for both young and old qNSCs across a few membrane lipid classes *(R*=0.96, *P*=0.00017 in young, *R*=0.93, *P*=0.00075 in old) (**fig. S6, C and D**). By calculating effect sizes, we identified several lipids (e.g. LPC(O−16:0) and LPC(O−18:1)/LPC(P−18:0)) that tended to increase with age both *in vitro* and *in vivo* as well as a membrane lipid LPE(20:4) that significantly decreased with age both *in vitro* and *in vivo* (**Fig. 1H**).

Quantification of lipids with unique side chains of each class revealed that side chain composition correlated between *in vitro* and *in vivo* datasets in both young (*R*~0.47, *P*=0.022) and old (*R*~0.48, *P*=0.017) qNSCs (**fig. S6E**). Notably, phosphatidylserine (PS) with 18:0 or 22:6 side chain significantly increases with age while PE(22:4) and LPE(20:4) decrease with age both *in vitro* and *in vivo* (**Fig. 1I**). Hence, we could detect some age-dependent changes in membrane lipids in qNSCs *in vivo*, although *in vivo* detection was limited due to the low starting material.

Spatial lipidomic profiling shows changes in membrane lipids in qNSCs *in situ*

We next asked if we could also observe age-related changes to complex membrane lipids in qNSCs in the neurogenic niche *in situ*, without subjecting cells to tissue dissociation and FACS sorting. To this end, we used desorption electrospray ionization mass spectrometry imaging (DESI-MSI) on whole mount sections of SVZ neurogenic niches (**Fig. 2A**, **Table S6**). DESI-MSI is a spatial lipidomics method that allows simultaneous *in situ* detection of lipids and metabolites while preserving tissue integrity (*88-90*) (**Fig. 2A**).

We acquired DESI-MSI spectra on SVZ neurogenic niche sections from n=7 young (3-5 months) and n=7 old (20-22 months) mice (one SVZ wholemount section from each animal). The SVZ neurogenic niche is heterogeneous and comprises several cell types (including qNSCs and aNSCs) (*54, 91-93*). We used sections of SVZ whole mount to assess cell layers that are immediately adjacent to the ventricle, where a high density of NSCs reside. As DESI-MSI has a resolution of 200 μm, the mass spectrum from each individual scan of the SVZ encompasses multiple cell types (**Fig. 2, A-C**). To obtain cell type-specific lipidomic profiles *in situ* in the SVZ, we used a deconvolution method we had previously developed and validated on brain sections with heterogenous composition of neurons and astrocytes (*90*). We first aligned DESI-MSI spectra with immunofluorescence images acquired on the same tissue section stained with cell type-specific markers ($GFAP^+Ki67^-$ for qNSCs/astrocytes, $GFAP^+Ki67^+$ for aNSCs, and $GFAP^-Ki67^+$ for neural progenitor cells, NPCs) (**Fig. 2, A-C**). We then applied our deconvolution method, using linear regression across heterogenous sections (*90, 94*), on each DESI-MSI spectrum with its associated cell type composition from immunofluorescence images (see Methods for details) (**Fig. 2A**). To test whether our previously developed deconvolution method (*90*) could be applied to the SVZ neurogenic niche, we verified that it yielded accurate

estimates of cell type-specific profiles from a reconstituted *in silico* mixture lipidomic data comprised of our own (present study) and published datasets (*33*) (see Methods for details) (**fig. S7, A and B**). We also asked if our deconvolution method could distinguish metabolomic profiles of different cell types (e.g. qNSCs/astrocytes vs. aNSCs). PCA could not separate the metabolomic profiles of qNSCs/astrocytes and aNSCs. We therefore used a supervised dimensionality reduction approach – Orthogonal Partial Least Squares-Discriminant Analysis (OPLS-DA) – to distinguish the metabolomic profiles of qNSCs/astrocytes and aNSCs (as well as young and old qNSCs/astrocytes) (**fig. S7, C-F**). Although supervised and therefore less unbiased than PCA, OPLS-DA is better suited to datasets containing highly correlated features – such as co-regulated metabolites within the same pathway – a pattern that is prevalent in DESI-MSI given its broad metabolic coverage (*95, 96*). We examined the performance of the OPLS-DA models and assessed potential over-fitting – a common concern for a supervised approach. We observed that OPLS-DA separated the metabolomic profiles of qNSCs/astrocytes and aNSCs following deconvolution of DESI-MSI data, and that the model performance was good (**fig. S7, C and D**). OPLS-DA could also distinguish qNSCs/astrocytes from young and old animals, although the model performance was not good in this case (**fig. S7, E and F**), likely due to a lack of sensitivity.

While the DESI-MSI approach was not sensitive enough to allow a global analysis of the lipidome with age *in situ*, we used it to identify specific lipids that significantly change with age in qNSCs/astrocytes in the neurogenic niche. We performed an additional tandem mass spectrometry on the same samples and annotated 11 highly abundant membrane lipid species (**fig. S8**). We then compared the age-associated effect sizes of these lipids from DESI-MSI to those obtained *in vitro* or *in vivo* from LC-MS/MS. Several membrane lipids exhibited consistent

208 age-dependent abundance changes in qNSCs/astrocytes by DESI-MSI and in qNSCs across *in*
209 *vitro* or *in vivo* LC-MS/MS datasets, including PE(P−18:1_18:1), which showed a trend toward
210 increased abundance with age, and PI(18:0_20:3), which showed a significant decreased
211 abundance with age (**Fig. 2D**). Hence, DESI-MSI could detect membrane lipid species that
212 consistently change with age in qNSCs in the context of intact SVZ neurogenic niches.

213 We next examined the spatial pattern of membrane lipids that show age-related changes.
214 We focused on PE(P-18:1_18:1) and PI(18:0_20:3), which show an increased or decreased
215 abundance with age, respectively, in qNSCs/astrocytes (**Fig. 2D**). We divided the SVZ into 3
216 equally-sized regions along the rostral-caudal axis, as it is known that qNSCs are more numerous
217 in the rostral region of the SVZ than niche astrocytes (*91-93*) (**Fig. 2E**). We quantified lipid
218 intensity for these specific lipids in each region overall (which encompasses multiple cell types)
219 (see Methods for details). Spatially, we found that PE(P-18:1_18:1) abundance increased with
220 age whereas PI(18:0_20:3) decreased with age in the rostral region of the SVZ – the region that
221 contains the highest density of qNSCs (*91-93*) (**Fig. 2, F and G**). Age-related changes of these
222 two lipids were also detected outside of the rostral region (and in a different direction for
223 PE(P-18:1_18:1)), likely due to changes in other cell types (**fig. S7, G and H**). Thus, spatial
224 lipidomic profiling by DESI-MSI was able to detect complex membrane lipids that change with
225 age in qNSCs in the intact SVZ neurogenic niche.

226

227 **Plasma membrane lipids are affected during aging**

228 Membrane lipids are major components of the plasma membrane and organelle membrane
229 (endoplasmic reticulum, Golgi apparatus, lysosome, mitochondrion, etc.) (*97, 98*). As the plasma

membrane is one of the largest membrane compartments in the cell, we asked if some of the lipid changes in old qNSCs could indeed occur at the level of the plasma membrane. We isolated the plasma membrane of qNSCs by generating giant plasma membrane vesicles (GPMVs) (**Fig. 3A**). GPMVs do not contain organellar lipids and represent mostly plasma membrane lipids in cells (*99, 100*). We verified that GPMVs from qNSCs were depleted in organelles and other cellular compartments by western blot (**fig. S9A**). We then performed untargeted lipidomics using LC-MS/MS with 14 internal standards on GPMVs generated from qNSCs from n=8 young (3-5 months) and n=8 old (20-22 months) mice (**Fig. 3A, Tables S1 and S7**). Our lipidomic analysis confirmed that GPMVs contained prominent plasma membrane lipid species, including PC, PE, PS, and cholesterol (**fig. S9B**). Overall, we detected 267 lipids in the GPMV dataset, 186 of which overlapped with the *in vitro* #1 (whole cell extract) dataset (**fig. S9C**). Of these overlapping lipids, 78 lipids increased with age and 46 lipids decreased with age (**fig. S9C**).

To identify consistent changes between GPMVs and *in vitro* datasets, we calculated effect sizes for these datasets. We found that lipids such as PE(P–18:1_18:1) and PE(18:1_20:4) significantly increased with age whereas PC(16:1_19:3) significantly decreased with age in both whole cell extracts and GPMVs (**Fig. 3B, fig. S9D**). Some of the lipids that change with age in GPMVs were abundant lipids (**fig. S9E**).

We also examined the side chain profiles of GPMV lipids. Similar to whole cell *in vitro* datasets, phospholipids containing highly unsaturated PUFAs significantly increased with age in both whole cell extracts and GPMVs, including PE(22:5), PE(20:4) and PE(20:5) (**Fig. 3C, fig. S9F**). Lipids with less unsaturated PUFA side chains, including PE(18:3), PC(19:3) and PC(20:3), significantly decreased with age in both whole cell extracts and GPMVs (**Fig. 3C, fig. S9F**). We also detected age-related changes in lipids containing monounsaturated fatty acid

(MUFA) and saturated fatty acid (SFA) side chains (**Fig. 3C, fig. S9F**). Some features that exhibit significant change with age were among side chains that have the highest concentration in GPMV and whole cells (e.g. PE(20:4), PE(18:1)), while others such as PE(18:3) were less abundant (**fig. S9G**). Together, these data raise the possibility that several of the lipid changes in old qNSCs occur at the level of the plasma membrane (although some lipid changes may also occur in other organelles).

Plasma membrane order is impacted by age

Age-associated changes in plasma membrane lipids could impact several biophysical properties of plasma membranes, including plasma membrane order (i.e. rigidity or fluidity), which is important for barrier function and signaling (*31, 101*). Unsaturation level, cholesterol, and phospholipid composition all contribute to plasma membrane order (*31, 101-104*). The accumulation of highly unsaturated PUFA side chains in old qNSC plasma membranes (see **Fig. 3C, fig. S9F**) and the trend toward decreased cholesterol levels in old qNSCs (**fig. S9H**) suggested that plasma membrane order may decrease during aging in old qNSCs. To experimentally test this prediction and measure plasma membrane order in qNSCs, we used the polarity-sensitive dye Laurdan, which is commonly used to measure plasma membrane order (*105-108*) (**Fig. 3D**). Laurdan can incorporate into membranes and can shift its emission spectrum from ~450nm (green, in ordered lipid environment) to ~500nm (red, in less ordered lipid environment.) (**Fig. 3D**), and the ratiometric quantification of Laurdan at the plasma membrane provides a measure of membrane order (*108*) (**Fig. 3D**). We stained young and old qNSCs *in vitro* with Laurdan and developed an automated image analysis pipeline to segment and outline the plasma membrane of individual qNSCs for unbiased ratiometric quantification

(see Methods for details) (**Fig. 3D**). Automated ratiometric quantification of Laurdan staining at the plasma membrane revealed that the plasma membranes of old qNSC cultures had a lower normalized generalized polarization ratio (GP ratio), indicative of a lower plasma membrane order, compared to young counterparts (**Fig. 3E**), consistent with predictions based on lipidomics. We also stratified our automated ratiometric Laurdan quantification based on cell density (**fig. S10A**) and cell size (**fig. S10B**), as these factors might influence plasma membrane order. We observed that old qNSCs exhibited a consistent decrease in plasma membrane order, regardless of cell density or size (**fig. S10, A and B**).

To independently assess plasma membrane order in young and old qNSC cultures, we performed fluorescence lifetime imaging (FLIM) (**Fig. 3F**). FLIM enables the quantification of fluorescence decay time – a metric that increases when membrane order is higher (*109, 110*) (**Fig. 3F**). Our FLIM analysis confirmed that old qNSCs have decreased fluorescence decay time compared to young counterparts (**Fig. 3F**), regardless of density (**fig. S10C**), consistent with a lower plasma membrane order. These data corroborate that old qNSCs exhibit lower plasma membrane order *in vitro*.

We then examined plasma membrane order in qNSCs *in vivo* using Laurdan staining because this fluorescent dye is compatible with cell marker analysis. To this end, we stained brain sections with the Laurdan fluorescent dye and performed immunostaining with antibodies to cell type markers to identify qNSCs/astrocytes ($GFAP^+EGFR^-$). For quantification, we only included $GFAP^+EGFR^-$ cells that were immediately adjacent to the ventricular wall and that contained a long basal process that is characteristic to qNSCs to minimize the inclusion of niche astrocytes (**Fig. 3G, fig. S10E**). We then performed ratiometric quantification of Laurdan fluorescence at the plasma membrane of identified qNSC using an automated pipeline (**Fig. 3G**,

fig. S10D) (see Methods for details). This analysis of Laurdan staining on brain sections from young and old mice showed that qNSCs from old mice exhibited decreased normalized GP ratio, indicative of a lower plasma membrane order (**Fig. 3H**), and this decrease in plasma membrane order was observed both around the cell body and at the basal process (**fig. S10E**). Thus, qNSCs exhibit decreased plasma membrane order with age *in vivo*, consistent with our *in vitro* findings.

Together, these results indicate that specific age-related lipidomic changes in qNSCs occur at the level of plasma membrane and are associated with changes in one key biophysical property – a less ordered (more fluid) plasma membrane (though other properties of plasma membranes such as strength, permeability, curvature, surface potential, transmembrane protein clustering may also be affected by lipid changes).

Identification of enzymes that impact the lipidome of young and old qNSCs

Could enzymes involved in remodeling the lipids that change with age in qNSCs impact the lipidome of these cells, and could they be used to test the functional significance of lipid changes in qNSCs with age? We focused on five lipid metabolic enzymes belonging to two classes known to regulate some of the lipid changes we observed in old qNSCs: i) phospholipid remodeling enzymes: MBOAT (membrane bound glycerophospholipid O-acyltransferase), AGPAT (1-acylglycerol-3-phosphate O-acyltransferase) and PLA2G4 (phospholipase A2 group IV); ii) PUFA biosynthesis enzymes: ELOVL (elongation of very long chain fatty acids-like) and FADS (fatty acid desaturase) (**Fig. 4A**). Among the different family members for these enzymes, we chose members that satisfy 2 of these 3 criteria: i) high expression in qNSCs/astrocytes based on our single-cell RNA-seq data (*14*), ii) significant changes in gene expression with age in

single-cell RNA-seq, and iii) substrate specificity of PUFA side chain remodeling in membrane lipid classes (**fig. S11**) (see Methods for details). Based on these criteria, the 5 enzyme family members we selected were MBOAT2, AGPAT3, PLA2G4E, ELOVL5, and FADS2.

To determine how manipulating these 5 enzymes affects the lipidome of young and old qNSCs, we knocked out their respective genes in primary cultures of qNSCs from n=4 young (3-5 months) and n=4 old (20-22 months) mice using a lentiviral-mediated CRISPR/Cas9 approach (**Fig. 4B, Table S8**). We verified that the knockout of each enzyme gene was efficient, with a frameshift editing of 44-69% of the alleles for each gene in both young and old qNSCs (except *Agpat3*) (**fig. S12A**). We then examined the lipidomic profile of these knockouts by performing LC-MS/MS with 13 standards on young and old qNSCs with respective knockouts and control (same experiment as "***In vitro* #2**" used in **Fig. 1**, see Methods for details) (**Table S1 and S9**). We quantified the concentration changes of specific lipids from our lipidomic data and confirmed that the knockouts of *Elovl5*, *Mboat2*, *Fads2*, and *Pla2g4e* in qNSCs led to the expected increase in lipid substrate and/or decrease in product levels (**fig. S12, B and C, Table S9**) (*Agpat3* knockout did not significantly affect its known substrate and product levels, perhaps due to lower knockout efficiency). Hence, the knockout of most of these enzymes is generally efficient in qNSCs.

We then compared the effects of different enzyme knockouts on the global lipidomic profiles. Each enzyme gene knockout (*Elovl5*, *Fads2*, *Mboat2*, *Agpat3*, or *Pla2g4e* knockout) led to a relatively specific lipidomic profile that could be mostly distinguished in PCA (**Fig. 4C**). Comparison between different knockouts indicated that more lipid species were uniquely enriched in individual knockouts than shared in 2 or more knockouts (**fig. S12D, Table S9**). PCA on individual gene knockouts revealed that the cellular lipidome of *Mboat2* and *Agpat3* knockout

exhibited a shift toward an "older" lipidome, in both young and old qNSCs (**Fig. 4D**, **fig. S2A**). Thus, the knockout of two lipid remodeling enzymes, *Mboat2* and *Agpat3*, shifts the lipidome of qNSCs toward an older lipidome.

Mboat2* knockout alters specific lipids and impairs old qNSC function *in vitro

We focused on *Mboat2* because *Mboat2* gene expression significantly decreased in old qNSCs/astrocytes in single cell RNA-seq datasets (**fig. S11**). *In situ* RNA hybridization also showed that *Mboat2* expression generally decreased in old brain sections (**Fig. 4E**, **Table S10**).

We determined if *Mboat2* knockout modulates specific lipids that also change with age. By analyzing our lipidomics datasets, we found that *Mboat2* knockout in old qNSCs led to an increase in several lipid species that normally accumulate with age in qNSCs, notably PUFA-containing PE and ether PC species such as PE(18:0_22:6), PE(18:1_20:4), and PC(O-18:1_22:6) (**Fig. 4F**). Conversely, *Mboat2* knockout in old qNSCs led to a decrease in several lipid species that normally decrease with age in qNSCs, notably MUFA-containing PC species such as PC(17:0_18:1), PC(16:0_17:1), and PC(17:1_18:1) (**Fig. 4F**). We also observe that *Mboat2* knockout led to side chain composition changes that mimic age-associated remodeling in old qNSCs. For example, *Mboat2* knockout and aging both led to an increase in PE(20:5) and a decrease in PC(17:1) (**fig. S12E**).

We asked if *Mboat2* knockout could have functional consequences on the ability of qNSCs to activate (i.e. transition from quiescence to proliferation) – a main biological function of qNSCs that deteriorates with age (*15, 27, 57, 58, 111*). We knocked out *Mboat2* in young and old qNSCs and measured the proportion of qNSCs that activate in response to growth factors,

using FACS analysis with the proliferation marker Ki67 (**fig. S13** for the FACS gating strategy). We verified that qNSCs activation ability decreased with age (~40% decrease, P=0.003) (**Fig. 4G**). *Mboat2* knockout in old qNSCs led to further impairment in old qNSC activation ability (~50% decrease, P<0.001) (**Fig. 4G**). By contrast, *Mboat2* knockout in young qNSCs did not impact their activation level (**Fig. 4G**), despite impacting the young lipidome (see **Fig. 4D**) – perhaps because young qNSCs have a better 'buffering capacity' for activation than old qNSCs. We next tested whether *Mboat2* knockout affects plasma membrane order. Our Laurdan staining and automated ratiometric quantification pipeline showed that *Mboat2* knockout was not sufficient to affect plasma membrane order in qNSCs (young or old) (**fig. S12F**). Thus, *Mboat2* deficiency exacerbates the decrease in qNSCs activation with age (but does not overtly affect plasma membrane order).

Mboat2 overexpression modulates qNSC lipidome and boosts old qNSC activation _in vitro_

We next tested the impact of overexpressing *Mboat2* on young and old qNSCs (**Table S11**). Lentiviral-mediated overexpression of *Mboat2* led to a 5-fold increase in *Mboat2* mRNA level in both young and old qNSCs (with a similar transduction efficiency in young and old of 53-55%, **fig. S12, G and H**). We performed LC-MS/MS with 14 internal standards on n=4 young and n=4 old qNSCs with overexpression of *Mboat2* (see Methods for details) (**fig. S12I, Table S1 and S12**). Analysis of this lipidomic dataset showed the expected decrease and increase in substrate level and product/substrate ratio of MBOAT2 (**fig. S12J, Table S12**). PCA suggests that *Mboat2* overexpression led to a lipidomic shift towards the direction of 'young' in both young and old qNSCs (**Fig. 4H**), opposite to what was observed in cells with *Mboat2* knockout (**Fig. 4D**).

We asked whether overexpressing *Mboat2* results in changes of lipids that exhibit age-associated differences (**Fig. 1E**). *Mboat2* overexpression in old qNSCs led to the accumulation of PC(16:0_22:5), a lipid that normally decreases with age. Conversely, *Mboat2* overexpression in old qNSCs led to a decreased level of PE(16:0_16:0), a lipid that normally increases with age (**Fig. 4I**). At side chain composition level, *Mboat2* overexpression led to a decrease in 3 side chain features that contain highly unsaturated fatty acids (PE(20:4), PE(20:5) and PI(20:5)), which normally accumulate with age (**fig. S12K**). These results suggest that increasing the level of *Mboat2* reverses some of the age-associated lipidomic changes.

We next assessed the effect of *Mboat2* overexpression on the ability of young and old qNSCs to activate *in vitro*. We verified that qNSCs activation ability decreased with age (~10% decrease, P=0.046) (**Fig. 4J**). *Mboat2* overexpression significantly boosted the activation of young and old qNSCs (~9% and 32% increase, P=0.038 and P=0.00049, respectively) (**Fig. 4J**). These data indicate that *Mboat2* overexpression can boost old NSC function *in vitro*.

Mboat2* overexpression boosts the number of activated NSCs in old mice *in vivo

What is the impact of *Mboat2* overexpression *in vivo*? To address this question, we stereotaxically injected lentivirus expressing *Mboat2* in the lateral ventricles of young and old mice, in the vicinity of NSCs (**Fig. 4K**). We verified that these injections led to increased *Mboat2* transcripts in SVZ cells (including qNSCs) by *in situ* RNA hybridization on brain sections from young and old mice (**fig. S12L**). There was a decrease in the number of aNSCs between young and old mice (35% decrease, P=0.013) (**Fig. 4L**). *Mboat2* overexpression led to a significant increase in the proportion of actively proliferating NSCs (aNSCs) in the SVZ of old

410 mice (but not young mice) *in vivo* (97% increase, *P*=0.001) (**Fig. 4L**). Hence, overexpression of
411 *Mboat2* also boosts the activation potential of old NSCs *in vivo*.

412

413 **Supplementation with plasma membrane lipids from young NSCs**

414 To assess the effects of plasma membrane lipids on old qNSC function, we supplemented old
415 qNSCs with lipids extracted from the plasma membrane of young qNSCs. For these
416 supplementation experiments, we first extracted plasma membrane lipids from GPMVs of young
417 or old qNSCs ("donor cells"), and we used these extracted plasma membrane lipids to
418 supplement young and old qNSC cultures ("recipient cells") (**Fig. 5A**). Exogenous phospholipids
419 have been shown to incorporate into the plasma membrane via fusion or lipid exchange between
420 lipid vesicles and cells (*112*). Once incorporated, a portion of the exogenous phospholipids can
421 be internalized via the endocytic pathway for subsequent delivery to intracellular compartments
422 (*113*). To verify lipid uptake, we used the lipophilic dye Vybrant™ DiI to fluorescently label the
423 plasma membrane lipid extracts. We observed that labeled supplemented lipids were found in
424 puncta inside NSCs, suggesting uptake through the endocytic system (**fig. S14A,** see also below
425 for verification of membrane lipid enrichment).

426 To examine the global lipidome of young or old qNSCs supplemented with young plasma
427 membrane lipids, we performed LC-MS/MS with 14 internal standards on n=4 young or n=4 old
428 qNSCs supplemented for 72 hours with young plasma membrane lipids (**fig. S14B, Table S1**
429 **and S13**). We verified that the majority of the lipids that increased upon supplementation were
430 indeed plasma membrane lipids (as defined by enrichment in GPMVs vs. whole cell extracts)
431 (**fig. S14C, Table S13**), corroborating that the supplementation was successful. We did not

observe global changes in recipient qNSCs (young or old) upon young plasma lipid supplementation (**fig. S14D**). However, old recipient qNSCs supplemented with young plasma membrane lipids exhibited a higher proportion of plasma membrane lipids that are enriched in young GPMVs compared to young recipient counterparts (23.3% in old recipient qNSCs vs. 15.1% in young recipient qNSCs) (**fig. S14E**, yellow slice), including PC(17:1_18:1) and PC(16:0_22:5) (**Fig. 5B**, right panel, lower right quadrant). Thus, while supplementation with young plasma membrane lipids is not sufficient to impact the global lipidome of old recipient qNSCs, it restores some plasma membrane lipids normally more abundant in young plasma membrane in old qNSCs (and to a greater extent than in young counterparts).

Supplementation with young plasma membrane lipids boosts old NSC function

We next assessed the effect of plasma membrane lipid supplementation on young and old qNSC activation. As expected, there was a 44% decrease in qNSC activation with age (P=0.034). Notably, supplementation with plasma membrane lipids from young donor qNSCs led to a small, significant increase in the ability of old recipient qNSCs (but not young recipient qNSCs) to activate (23% increase, P=0.031) (**Fig. 5C**). Supplementation with plasma membrane lipids from old donor qNSCs did not significantly affect the ability of recipient young or old qNSC to activate (**Fig. 5C**). Hence, supplementation with young plasma membrane lipids can ameliorate the function of old quiescent NSCs.

Finally, we determined the effects of plasma membrane lipid supplementation on plasma membrane order by performing Laurdan staining (**Fig. 5D**). As we have previously found, plasma membrane order was significantly decreased in old qNSCs compared to young

454 counterpart (*P*=0.031) (**Fig. 5D**). Supplementation with young plasma membrane lipids did not
455 significantly affect plasma membrane order in old recipient qNSCs compared to unsupplemented
456 old qNSCs. However, plasma membrane order was significantly higher in old recipient qNSCs
457 supplemented with young plasma membrane lipids than in those supplemented with old plasma
458 membrane lipids (*P*=0.031) (**Fig. 5D**). Overall, there was a positive correlation between recipient
459 cells' ability to activate and their plasma membrane order (**fig. S14F**).

460 Thus, supplementation with lipids extracted from young plasma membranes improves the
461 function of old qNSCs, and this may be linked to increased membrane order.

Discussion

Our global lipidomic study shows that several complex lipids change with age in old qNSCs *in vitro* and *in vivo*. We find that specific membrane lipids are remodeled with age and exhibit a shift in the side chain composition, including lipids with a higher PUFA content, in qNSCs. Our spatial lipidomic profiling using DESI-MSI indicates that some of these age-related changes in membrane lipids occur in intact neurogenic niches *in situ*. By performing lipidomic analysis on isolated plasma membrane, we find that plasma membrane lipids contribute to these age-related lipidomic changes. Our study, together with other datasets in different organs (*46, 47*), highlight lipid changes in cells and organs as a key hallmark of aging.

Prior lipidomics analyses have been conducted in cultured mammalian cells (e.g. oligodendrocytes, neurons, microglia, etc.) (*33, 76, 97, 114-119*), but not in the context of aging. In flies, lipidomic analysis indicates lipid changes related to energy metabolism in senescent glia (*83*). Lipidomics studies have also been performed on whole organisms or organs (e.g. whole brains) in aging or Alzheimer's disease (*35, 36, 38, 39, 42, 43, 46, 47, 120-131*), but without cellular resolution. Overall, our lipidomics datasets represent the first systematic examination of the lipidome of aging NSCs, and more generally of aging mammalian cells, *in vitro* and *in vivo*.

We observe a reduced plasma membrane order (more fluid) in old qNSCs. Membrane order has been shown to impact a broad range of biological processes, including immune signaling, virus infection, and signal transduction (*28, 29, 132*). Reduced membrane order has also been observed in lymphocytes and neutrophils with age (*133, 134*), whereas increase in membrane order was shown in hippocampal neurons with age (*135*). These different changes in membrane properties with age may be directly linked to the function of the cell, its proliferative status (*136*), and cell-cell contacts (*137*). In old qNSCs, a reduced membrane order may impair

activation efficiency through disrupting the localization of transmembrane proteins important for proliferation. Indeed, plasma membrane lipids directly interact with a vast number of membrane proteins (*28, 138, 139*), including transmembrane receptors, and aging may disproportionally affect membrane proteins (*140-143*). Changes in plasma membrane properties may also affect other key aspects of membranes (e.g. strength, permeability, curvature, membrane potential, etc.) that could be important for qNSC function, including endocytosis and phagocytosis.

We identify interventions that affect plasma membrane lipids and find that they regulate the ability of qNSCs to activate during aging (**Fig. 5E**). For example, deficiency in the phospholipid acyltransferase MBOAT2 exacerbates aging defects in qNSCs and overexpression of MBOAT2 boosts the ability of old qNSCs to activate. As MBOAT2 has been shown to inhibit ferroptosis by remodeling phospholipids in the context of cancer cells (*144*), the beneficial effect of MBOAT2 on old NSC activation could also be due to its ability to decrease ferroptosis. Dysregulation of phospholipid acyltransferases has previously been linked to aberrant intestinal stem cell proliferation (*145*), tumorigenesis (*145, 146*) and liver disease (*147-149*). Our results now implicate a phospholipid acyltransferase in aging. Other enzymes, such as fatty acid elongases (*150*), may also contribute to aging defects. We also show that supplementing young plasma membrane lipids boosts activation in old qNSCs and that plasma membrane order correlates with the ability of qNSCs to activate. Thus, restoring specific lipids to a young lipid profile – either genetically or by affecting lipids themselves – could be an effective strategy to slow cellular aging and counter age-related diseases, including neurodegenerative diseases.

While our study identified specific lipids that changed during NSC aging, we were not able to observe strong changes in lipid class composition. It will be interesting to perform targeted lipidomic studies to determine if aging is accompanied with changes in sub-classes of

lipids (e.g. glycolipids (*151*)). In addition, the total number of lipids we detected from NSCs freshly isolated from the brain was low and the overlap with *in vitro* NSC cultures was limited. Thus, in addition to increasing sensitivity for lipid detection for *in vivo* NSCs, it will be important to benchmark and optimize the NSC culture models to better reflect the *in vivo* conditions. Finally, it will be interesting to examine if overexpression of MBOAT2 or supplementation with lipid membranes *in vivo* can boost neurogenesis and improve behavior in old mice.

Acknowledgments

We thank Jingxun Chen, Rahul Nagvekar, Param P. Singh, Katharina Papsdorf, Lucy Xu, Jason W. Miklas and all Brunet lab members for their input on the project and for providing feedback on the manuscript. We thank Itay Budin and Bianxiao Cui for helpful discussion on membrane lipid assays and Jonathan Z. Long for functional lipid experiment designs. We also thank members of the Cui lab and Snyder lab for advice on the project. We thank Monther Abu-Remaileh, Peter J. Mullen, Sarah E. Hancock, Jace W. Jones, and Ngoc Vu for advice on lipidomics. This work was supported by NIH P01AG036695 (A.B.), a generous gift from Timothy and Michele Barakett, AFOSR FA9550-21-1-0170 (R.N.Z), and a postdoctoral fellowship from American Federation for Aging Research (X.Z.). Schematic diagrams were created with BioRender.com.

Author contributions

X.Z. designed the project with help from A.B.. X.Z. performed all experiments and computational analyses unless otherwise indicated. R.M.F. performed immunofluorescence and HCR experiments and automated quantification to test *Mboat2* expression and function *in vivo*. J.N. assessed the impact of *Mboat2* overexpression on NSC activation *in vitro*. X.Y. performed DESI-MSI lipidomic profiling and structural validation under the supervision of R.N.Z.. A.E. performed lipidomic data processing and manual validation of all LC-MS/MS datasets. K.C. helped optimize and run lipidomic studies on LC-MS/MS, provided input on data validation and analysis under the supervision of M.P.S., and helped with independent code-checking. O.Y.Z. performed stereotaxic surgery on a subset of animals in *Mboat2 in vivo* overexpression experiment. F.V. performed cell type-specific deconvolution on DESI-MSI data, and provided input on lipidomic aging signatures under the supervision of P.K.. M.E. helped run LC-MS/MS lipidomic samples and data analysis under the supervision of M.P.S.. C.M.K. helped with CRISPR/Cas9 knockout in NSCs and data analysis on Laurdan staining. S.D.G. performed western blot experiments. C.J.S. helped optimize CRISPR/Cas9 knockout and activation assay in NSCs. M.C. helped with *in vivo* sorted lipidomic samples, data analysis, and independent code checking under the supervision of M.P.S.. G.M.T. helped optimizing and running LC-MS/MS lipidomic samples under the supervision of M.P.S.. A.M. performed image analysis for DESI-MSI dataset and helped with independent code-checking. D.H. helped run and analyze data from Lipidyzer platform under the supervision of M.P.S.. M.P.S. and R.N.Z. gave intellectual input on the study. X.Z. wrote the manuscript with A.B.. All authors provided intellectual input and commented on the manuscript.

Competing interests

The authors declare no competing interests.

Data and material availability

Raw lipidomics data were uploaded to Metabolomicsworkbench.org under Study ID ST002258 (DatatrackID:3406), Study ID ST002259 (DatatrackID:3407) and Study ID ST002260 (DatatrackID:3408), Study ID ST004116 (DatatrackID:6214) and Study ID ST004117 (DatatrackID:6232). Processed lipidomics data are included as **Tables S3-S7, S9, S12 and S13**. Reagents generated in this study are available from the corresponding authors.

Code availability

The code used to analyze lipidomics data in the current study is available in the Github repository for this paper (https://github.com/xiaoaizhao/Neural-stem-cell-NSC-aging-lipidomics).

References

1. A. M. Bond, G. L. Ming, H. Song, Adult Mammalian Neural Stem Cells and Neurogenesis: Five Decades Later. *Cell Stem Cell* **17**, 385-395 (2015).
2. F. H. Gage, S. Temple, Neural stem cells: generating and regenerating the brain. *Neuron* **80**, 588-601 (2013).
3. M. Faiz *et al.*, Adult Neural Stem Cells from the Subventricular Zone Give Rise to Reactive Astrocytes in the Cortex after Stroke. *Cell Stem Cell* **17**, 624-634 (2015).
4. Z. Chaker, P. Codega, F. Doetsch, A mosaic world: puzzles revealed by adult neural stem cell heterogeneity. *Wiley Interdiscip Rev Dev Biol* **5**, 640-658 (2016).
5. A. Denoth-Lippuner, S. Jessberger, Mechanisms of cellular rejuvenation. *FEBS Lett* **593**, 3381-3392 (2019).

6. J. Ninkovic, M. Gotz, Signaling in adult neurogenesis: from stem cell niche to neuronal networks. *Curr Opin Neurobiol* **17**, 338-344 (2007).
7. G. Kalamakis *et al.*, Quiescence Modulates Stem Cell Maintenance and Regenerative Capacity in the Aging Brain. *Cell* **176**, 1407-1419 e1414 (2019).
8. Z. Chaker, S. Aid, H. Berry, M. Holzenberger, Suppression of IGF-I signals in neural stem cells enhances neurogenesis and olfactory function during aging. *Aging Cell* **14**, 847-856 (2015).
9. A. V. Molofsky *et al.*, Increasing p16INK4a expression decreases forebrain progenitors and neurogenesis during ageing. *Nature* **443**, 448-452 (2006).
10. H. Yousef *et al.*, Age-Associated Increase in BMP Signaling Inhibits Hippocampal Neurogenesis. *Stem Cells* **33**, 1577-1588 (2015).
11. R. Zhang *et al.*, Id4 Downstream of Notch2 Maintains Neural Stem Cell Quiescence in the Adult Hippocampus. *Cell Rep* **28**, 1485-1498 e1486 (2019).
12. E. G. Wheatley *et al.*, Neuronal O-GlcNAcylation Improves Cognitive Function in the Aged Mouse Brain. *Curr Biol* **29**, 3359-3369 e3354 (2019).
13. C. W. White, 3rd *et al.*, Age-related loss of neural stem cell O-GlcNAc promotes a glial fate switch through STAT3 activation. *Proc Natl Acad Sci U S A* **117**, 22214-22224 (2020).
14. B. W. Dulken *et al.*, Single-cell analysis reveals T cell infiltration in old neurogenic niches. *Nature* **571**, 205-210 (2019).
15. D. S. Leeman *et al.*, Lysosome activation clears aggregates and enhances quiescent neural stem cell activation during aging. *Science* **359**, 1277-1283 (2018).
16. G. Gontier *et al.*, Tet2 Rescues Age-Related Regenerative Decline and Enhances Cognitive Function in the Adult Mouse Brain. *Cell Rep* **22**, 1974-1981 (2018).
17. R. Beckervordersandforth *et al.*, Role of Mitochondrial Metabolism in the Control of Early Lineage Progression and Aging Phenotypes in Adult Hippocampal Neurogenesis. *Neuron* **93**, 1518 (2017).
18. S. A. Villeda *et al.*, The ageing systemic milieu negatively regulates neurogenesis and cognitive function. *Nature* **477**, 90-94 (2011).
19. E. Carrasco-Garcia, O. Arrizabalaga, M. Serrano, R. Lovell-Badge, A. Matheu, Increased gene dosage of Ink4/Arf and p53 delays age-associated central nervous system functional decline. *Aging Cell* **14**, 710-714 (2015).
20. S. Manzanero *et al.*, Intermittent fasting attenuates increases in neurogenesis after ischemia and reperfusion and improves recovery. *J Cereb Blood Flow Metab* **34**, 897-905 (2014).
21. S. Brandhorst *et al.*, A Periodic Diet that Mimics Fasting Promotes Multi-System Regeneration, Enhanced Cognitive Performance, and Healthspan. *Cell Metabolism* **22**, 86-99 (2015).
22. L. Katsimpardi *et al.*, Vascular and neurogenic rejuvenation of the aging mouse brain by young systemic factors. *Science* **344**, 630-634 (2014).
23. S. A. Villeda *et al.*, Young blood reverses age-related impairments in cognitive function and synaptic plasticity in mice. *Nat Med* **20**, 659-663 (2014).
24. T. A. Bedrosian *et al.*, Lamin B1 decline underlies age-related loss of adult hippocampal neurogenesis. *EMBO J* **40**, e105819 (2021).
25. A. M. Horowitz *et al.*, Blood factors transfer beneficial effects of exercise on neurogenesis and cognition to the aged brain. *Science* **369**, 167-173 (2020).

26. K. M. McAvoy *et al.*, Modulating Neuronal Competition Dynamics in the Dentate Gyrus to Rejuvenate Aging Memory Circuits. *Neuron* **91**, 1356-1373 (2016).
27. T. J. Ruetz *et al.*, CRISPR-Cas9 screens reveal regulators of ageing in neural stem cells. *Nature* **634**, 1150-1159 (2024).
28. G. van Meer, D. R. Voelker, G. W. Feigenson, Membrane lipids: where they are and how they behave. *Nat Rev Mol Cell Bio* **9**, 112-124 (2008).
29. E. Sezgin, I. Levental, S. Mayor, C. Eggeling, The mystery of membrane organization: composition, regulation and roles of lipid rafts. *Nat Rev Mol Cell Biol* **18**, 361-374 (2017).
30. T. Harayama, H. Riezman, Understanding the diversity of membrane lipid composition. *Nat Rev Mol Cell Biol* **19**, 281-296 (2018).
31. J. C. Holthuis, A. K. Menon, Lipid landscapes and pipelines in membrane homeostasis. *Nature* **510**, 48-57 (2014).
32. K. Bozek *et al.*, Organization and evolution of brain lipidome revealed by large-scale analysis of human, chimpanzee, macaque, and mouse tissues. *Neuron* **85**, 695-702 (2015).
33. D. Fitzner *et al.*, Cell-Type- and Brain-Region-Resolved Mouse Brain Lipidome. *Cell Rep* **32**, 108132 (2020).
34. N. M. Giusto, G. A. Salvador, P. I. Castagnet, S. J. Pasquare, M. G. Ilincheta de Boschero, Age-associated changes in central nervous system glycerolipid composition and metabolism. *Neurochem Res* **27**, 1513-1523 (2002).
35. X. Han, M. H. D, D. W. McKeel, Jr., J. Kelley, J. C. Morris, Substantial sulfatide deficiency and ceramide elevation in very early Alzheimer's disease: potential role in disease pathogenesis. *J Neurochem* **82**, 809-818 (2002).
36. X. Han, D. M. Holtzman, D. W. McKeel, Jr., Plasmalogen deficiency in early Alzheimer's disease subjects and in animal models: molecular characterization using electrospray ionization mass spectrometry. *J Neurochem* **77**, 1168-1180 (2001).
37. S. I. Lee *et al.*, APOE4-carrying human astrocytes oversupply cholesterol to promote neuronal lipid raft expansion and Abeta generation. *Stem Cell Reports* **16**, 2128-2137 (2021).
38. A. S. Mutlu, J. Duffy, M. C. Wang, Lipid metabolism and lipid signals in aging and longevity. *Dev Cell* **56**, 1394-1407 (2021).
39. A. Naudi *et al.*, Lipidomics of human brain aging and Alzheimer's disease pathology. *Int Rev Neurobiol* **122**, 133-189 (2015).
40. N. Ollen-Bittle *et al.*, Co-registration of MALDI-MSI and histology demonstrates gangliosides co-localize with amyloid beta plaques in Alzheimer's disease. *Acta Neuropathol* **147**, 105 (2024).
41. M. Savini *et al.*, Lysosome lipid signalling from the periphery to neurons regulates longevity. *Nat Cell Biol* **24**, 906-916 (2022).
42. D. Tan *et al.*, A class of anti-inflammatory lipids decrease with aging in the central nervous system. *Nat Chem Biol* **19**, 187-197 (2023).
43. J. Tu, Y. Yin, M. Xu, R. Wang, Z. J. Zhu, Absolute quantitative lipidomics reveals lipidome-wide alterations in aging brain. *Metabolomics* **14**, 5 (2017).
44. R. Smidak, H. C. Kofeler, H. Hoeger, G. Lubec, Comprehensive identification of age-related lipidome changes in rat amygdala during normal aging. *PLoS One* **12**, e0180675 (2017).

45. Y. Dai, H. Tang, S. Pang, The Crucial Roles of Phospholipids in Aging and Lifespan Regulation. *Front Physiol* **12**, 775648 (2021).
46. D. Latumalea, M. Unfried, D. Barardo, J. Gruber, B. K. Kennedy, DoliClock: a lipid-based aging clock reveals accelerated aging in neurological disorders. *Aging (Albany NY)* **17**, (2025).
47. M. Unfried *et al.*, LipidClock: A Lipid-Based Predictor of Biological Age. *Front Aging* **3**, 828239 (2022).
48. A. Ernst *et al.*, Neurogenesis in the striatum of the adult human brain. *Cell* **156**, 1072-1083 (2014).
49. G. Pellegrino *et al.*, A comparative study of the neural stem cell niche in the adult hypothalamus of human, mouse, rat and gray mouse lemur (Microcebus murinus). *J Comp Neurol* **526**, 1419-1443 (2018).
50. F. Doetsch, I. Caille, D. A. Lim, J. M. Garcia-Verdugo, A. Alvarez-Buylla, Subventricular zone astrocytes are neural stem cells in the adult mammalian brain. *Cell* **97**, 703-716 (1999).
51. G. L. Ming, H. Song, Adult neurogenesis in the mammalian brain: significant answers and significant questions. *Neuron* **70**, 687-702 (2011).
52. M. Bolborea, N. Dale, Hypothalamic tanycytes: potential roles in the control of feeding and energy balance. *Trends Neurosci* **36**, 91-100 (2013).
53. M. S. Kaplan, J. W. Hinds, Neurogenesis in the adult rat: electron microscopic analysis of light radioautographs. *Science* **197**, 1092-1094 (1977).
54. K. Obernier, A. Alvarez-Buylla, Neural stem cells: origin, heterogeneity and regulation in the adult mammalian brain. *Development* **146**, (2019).
55. F. H. Gage, Neurogenesis in the adult brain. *J Neurosci* **22**, 612-613 (2002).
56. P. Navarro Negredo, R. W. Yeo, A. Brunet, Aging and Rejuvenation of Neural Stem Cells and Their Niches. *Cell Stem Cell* **27**, 202-223 (2020).
57. V. Capilla-Gonzalez, A. Cebrian-Silla, H. Guerrero-Cazares, J. M. Garcia-Verdugo, A. Quinones-Hinojosa, Age-related changes in astrocytic and ependymal cells of the subventricular zone. *Glia* **62**, 790-803 (2014).
58. E. Enwere *et al.*, Aging results in reduced epidermal growth factor receptor signaling, diminished olfactory neurogenesis, and deficits in fine olfactory discrimination. *J Neurosci* **24**, 8354-8365 (2004).
59. L. Bondolfi, F. Ermini, J. M. Long, D. K. Ingram, M. Jucker, Impact of age and caloric restriction on neurogenesis in the dentate gyrus of C57BL/6 mice. *Neurobiol Aging* **25**, 333-340 (2004).
60. A. Y. Maslov, T. A. Barone, R. J. Plunkett, S. C. Pruitt, Neural stem cell detection, characterization, and age-related changes in the subventricular zone of mice. *J Neurosci* **24**, 1726-1733 (2004).
61. N. M. Ben Abdallah, L. Slomianka, A. L. Vyssotski, H. P. Lipp, Early age-related changes in adult hippocampal neurogenesis in C57 mice. *Neurobiol Aging* **31**, 151-161 (2010).
62. A. Ibrayeva *et al.*, Early stem cell aging in the mature brain. *Cell Stem Cell* **28**, 955-966 e957 (2021).
63. J. Luo, S. B. Daniels, J. B. Lennington, R. Q. Notti, J. C. Conover, The aging neurogenic subventricular zone. *Aging Cell* **5**, 139-152 (2006).

64. V. Tropepe, C. G. Craig, C. M. Morshead, D. van der Kooy, Transforming growth factor-alpha null and senescent mice show decreased neural progenitor cell proliferation in the forebrain subependyma. *J Neurosci* **17**, 7850-7859 (1997).
65. G. Gheusi, P. M. Lledo, Adult neurogenesis in the olfactory system shapes odor memory and perception. *Prog Brain Res* **208**, 157-175 (2014).
66. V. Silva-Vargas, A. R. Maldonado-Soto, D. Mizrak, P. Codega, F. Doetsch, Age-Dependent Niche Signals from the Choroid Plexus Regulate Adult Neural Stem Cells. *Cell Stem Cell* **19**, 643-652 (2016).
67. W. Zheng *et al.*, Neurogenesis in adult human brain after traumatic brain injury. *J Neurotrauma* **30**, 1872-1880 (2013).
68. A. Arvidsson, T. Collin, D. Kirik, Z. Kokaia, O. Lindvall, Neuronal replacement from endogenous precursors in the adult brain after stroke. *Nat Med* **8**, 963-970 (2002).
69. K. Jin *et al.*, Evidence for stroke-induced neurogenesis in the human brain. *Proc Natl Acad Sci U S A* **103**, 13198-13202 (2006).
70. S. G. Kernie, J. M. Parent, Forebrain neurogenesis after focal Ischemic and traumatic brain injury. *Neurobiol Dis* **37**, 267-274 (2010).
71. S. Beyaz *et al.*, High-fat diet enhances stemness and tumorigenicity of intestinal progenitors. *Nature* **531**, 53-58 (2016).
72. M. Bowers *et al.*, FASN-Dependent Lipid Metabolism Links Neurogenic Stem/Progenitor Cell Activity to Learning and Memory Deficits. *Cell Stem Cell* **27**, 98-109 e111 (2020).
73. M. Clemot, R. Senos Demarco, D. L. Jones, Lipid Mediated Regulation of Adult Stem Cell Behavior. *Front Cell Dev Biol* **8**, 115 (2020).
74. M. Knobloch *et al.*, Metabolic control of adult neural stem cell activity by Fasn-dependent lipogenesis. *Nature* **493**, 226-230 (2013).
75. M. Knobloch *et al.*, A Fatty Acid Oxidation-Dependent Metabolic Shift Regulates Adult Neural Stem Cell Activity. *Cell Rep* **20**, 2144-2155 (2017).
76. K. R. Levental *et al.*, omega-3 polyunsaturated fatty acids direct differentiation of the membrane phenotype in mesenchymal stem cells to potentiate osteogenesis. *Sci Adv* **3**, eaao1193 (2017).
77. S. Madsen *et al.*, A fluorescent perilipin 2 knock-in mouse model reveals a high abundance of lipid droplets in the developing and adult brain. *Nat Commun* **15**, 5489 (2024).
78. M. D. Mana *et al.*, High-fat diet-activated fatty acid oxidation mediates intestinal stemness and tumorigenicity. *Cell Rep* **35**, 109212 (2021).
79. R. Mancini *et al.*, Metabolic features of cancer stem cells: the emerging role of lipid metabolism. *Oncogene* **37**, 2367-2378 (2018).
80. M. M. Mihaylova *et al.*, Fasting Activates Fatty Acid Oxidation to Enhance Intestinal Stem Cell Function during Homeostasis and Aging. *Cell Stem Cell* **22**, 769-778 e764 (2018).
81. P. S. Minhas *et al.*, Restoring metabolism of myeloid cells reverses cognitive decline in ageing. *Nature* **590**, 122-128 (2021).
82. M. Ramosaj *et al.*, Lipid droplet availability affects neural stem/progenitor cell metabolism and proliferation. *Nat Commun* **12**, 7362 (2021).
83. C. N. Byrns *et al.*, Senescent glia link mitochondrial dysfunction and lipid accumulation. *Nature* **630**, 475-483 (2024).

84. T. E. Sweeney, W. A. Haynes, F. Vallania, J. P. Ioannidis, P. Khatri, Methods to increase reproducibility in differential gene expression via meta-analysis. *Nucleic Acids Res* **45**, e1 (2017).
85. F. M. Feringa *et al.*, The Neurolipid Atlas: a lipidomics resource for neurodegenerative diseases *Nature Metabolism* **7**, 2142–2164 (2024).
86. H. Yu *et al.*, MassCube improves accuracy for metabolomics data processing from raw files to phenotype classifiers. *Nat Commun* **16**, 5487 (2025).
87. P. Codega *et al.*, Prospective identification and purification of quiescent adult neural stem cells from their in vivo niche. *Neuron* **82**, 545-559 (2014).
88. Z. Takats, J. M. Wiseman, B. Gologan, R. G. Cooks, Mass spectrometry sampling under ambient conditions with desorption electrospray ionization. *Science* **306**, 471-473 (2004).
89. J. M. Wiseman, D. R. Ifa, A. Venter, R. G. Cooks, Ambient molecular imaging by desorption electrospray ionization mass spectrometry. *Nat Protoc* **3**, 517-524 (2008).
90. X. Yan *et al.*, Cell-Type-Specific Metabolic Profiling Achieved by Combining Desorption Electrospray Ionization Mass Spectrometry Imaging and Immunofluorescence Staining. *Anal Chem* **92**, 13281-13289 (2020).
91. Q. Shen *et al.*, Adult SVZ stem cells lie in a vascular niche: a quantitative analysis of niche cell-cell interactions. *Cell Stem Cell* **3**, 289-300 (2008).
92. M. Tavazoie *et al.*, A specialized vascular niche for adult neural stem cells. *Cell Stem Cell* **3**, 279-288 (2008).
93. Z. Mirzadeh, F. T. Merkle, M. Soriano-Navarro, J. M. Garcia-Verdugo, A. Alvarez-Buylla, Neural stem cells confer unique pinwheel architecture to the ventricular surface in neurogenic regions of the adult brain. *Cell Stem Cell* **3**, 265-278 (2008).
94. S. S. Shen-Orr *et al.*, Cell type-specific gene expression differences in complex tissues. *Nat Methods* **7**, 287-289 (2010).
95. B. Worley, R. Powers, Multivariate Analysis in Metabolomics. *Curr Metabolomics* **1**, 92-107 (2013).
96. J. Bartel, J. Krumsiek, F. J. Theis, Statistical methods for the analysis of high-throughput metabolomics data. *Comput Struct Biotechnol J* **4**, e201301009 (2013).
97. A. Y. Andreyev *et al.*, Subcellular organelle lipidomics in TLR-4-activated macrophages. *J Lipid Res* **51**, 2785-2797 (2010).
98. G. van Meer, A. I. de Kroon, Lipid map of the mammalian cell. *J Cell Sci* **124**, 5-8 (2011).
99. T. Baumgart *et al.*, Large-scale fluid/fluid phase separation of proteins and lipids in giant plasma membrane vesicles. *P Natl Acad Sci USA* **104**, 3165-3170 (2007).
100. E. Sezgin *et al.*, Elucidating membrane structure and protein behavior using giant plasma membrane vesicles. *Nat Protoc* **7**, 1042-1051 (2012).
101. I. Budin *et al.*, Viscous control of cellular respiration by membrane lipid composition. *Science* **362**, 1186-1189 (2018).
102. W. J. Vanblitterswijk, B. W. Vandermeer, H. Hilkmann, Quantitative Contributions of Cholesterol and the Individual Classes of Phospholipids and Their Degree of Fatty Acyl (Un)Saturation to Membrane Fluidity Measured by Fluorescence Polarization. *Biochemistry-Us* **26**, 1746-1756 (1987).
103. G. M'Baye, Y. Mely, G. Duportail, A. S. Klymchenko, Liquid ordered and gel phases of lipid bilayers: fluorescent probes reveal close fluidity but different hydration. *Biophys J* **95**, 1217-1225 (2008).

104. G. van Meer, W. L. Vaz, Membrane curvature sorts lipids. Stabilized lipid rafts in membrane transport. *EMBO Rep* **6**, 418-419 (2005).
105. S. Mazeres, E. Joly, A. Lopez, C. Tardin, Characterization of M-laurdan, a versatile probe to explore order in lipid membranes. *F1000Res* **3**, 172 (2014).
106. D. M. Owen, C. Rentero, A. Magenau, A. Abu-Siniyeh, K. Gaus, Quantitative imaging of membrane lipid order in cells and organisms. *Nat Protoc* **7**, 24-35 (2011).
107. S. A. Sanchez, M. A. Tricerri, E. Gratton, Laurdan generalized polarization fluctuations measures membrane packing micro-heterogeneity in vivo. *Proc Natl Acad Sci U S A* **109**, 7314-7319 (2012).
108. P. Carravilla *et al.*, Measuring plasma membrane fluidity using confocal microscopy. *Nat Protoc* **20**, 1976-2004 (2025).
109. D. M. Owen *et al.*, Fluorescence lifetime imaging provides enhanced contrast when imaging the phase-sensitive dye di-4-ANEPPDHQ in model membranes and live cells. *Biophys J* **90**, L80-82 (2006).
110. Y. Wu *et al.*, Molecular rheometry: direct determination of viscosity in Lo and Ld lipid phases via fluorescence lifetime imaging. *Phys Chem Chem Phys* **15**, 14986-14993 (2013).
111. C. Giachino *et al.*, Molecular diversity subdivides the adult forebrain neural stem cell population. *Stem Cells* **32**, 70-84 (2014).
112. R. E. Pagano, L. Huang, Interaction of phospholipid vesicles with cultured mammalian cells. II. Studies of mechanism. *J Cell Biol* **67**, 49-60 (1975).
113. E. Farge, D. M. Ojcius, A. Subtil, A. Dautry-Varsat, Enhancement of endocytosis due to aminophospholipid transport across the plasma membrane of living cells. *Am J Physiol* **276**, C725-733 (1999).
114. X. Lu *et al.*, Integrated Lipidomics and Transcriptomics Characterization upon Aging-Related Changes of Lipid Species and Pathways in Human Bone Marrow Mesenchymal Stem Cells. *J Proteome Res* **18**, 2065-2077 (2019).
115. C. B. Merrill *et al.*, Patch clamp-assisted single neuron lipidomics. *Sci Rep* **7**, 5318 (2017).
116. A. A. Nugent *et al.*, TREM2 Regulates Microglial Cholesterol Metabolism upon Chronic Phagocytic Challenge. *Neuron* **105**, 837-854 e839 (2020).
117. C. Z. Ulmer, R. A. Yost, J. Chen, C. E. Mathews, T. J. Garrett, Liquid Chromatography-Mass Spectrometry Metabolic and Lipidomic Sample Preparation Workflow for Suspension-Cultured Mammalian Cells using Jurkat T lymphocyte Cells. *J Proteomics Bioinform* **8**, 126-132 (2015).
118. Y. Zou *et al.*, Plasticity of ether lipids promotes ferroptosis susceptibility and evasion. *Nature* **585**, 603-608 (2020).
119. P. Rusu *et al.*, GPD1 Specifically Marks Dormant Glioma Stem Cells with a Distinct Metabolic Profile. *Cell Stem Cell* **25**, 241-257 e248 (2019).
120. T. D. Admasu *et al.*, Lipid profiling of C. elegans strains administered pro-longevity drugs and drug combinations. *Sci Data* **5**, 180231 (2018).
121. K. Contrepois *et al.*, Cross-Platform Comparison of Untargeted and Targeted Lipidomics Approaches on Aging Mouse Plasma. *Sci Rep* **8**, 17747 (2018).
122. J. de Costa, G. Barja, P. F. Almaida-Pagan, Membrane peroxidation index and maximum lifespan are negatively correlated in fish of the genus Nothobranchius. *J Exp Biol* **223**, (2020).

123. V. Gonzalez-Covarrubias *et al.*, Lipidomics of familial longevity. *Aging Cell* **12**, 426-434 (2013).
124. D. Hornburg *et al.*, Dynamic lipidome alterations associated with human health, disease and ageing. *Nat Metab* **5**, 1578-1594 (2023).
125. A. J. Hulbert, Explaining longevity of different animals: is membrane fatty acid composition the missing link? *Age (Dordr)* **30**, 89-97 (2008).
126. G. E. Janssens *et al.*, A conserved complex lipid signature marks human muscle aging and responds to short-term exercise. *Nat Aging* **4**, 681-693 (2024).
127. M. Jove *et al.*, New insights into human prefrontal cortex aging with a lipidomics approach. *Expert Rev Proteomics* **18**, 333-344 (2021).
128. J. W. Pettegrew, K. Panchalingam, G. Withers, D. McKeag, S. Strychor, Changes in brain energy and phospholipid metabolism during development and aging in the Fischer 344 rat. *J Neuropathol Exp Neurol* **49**, 237-249 (1990).
129. O. S. Ademowo, M. R. Wenk, A. B. Maier, Advances in clinical application of lipidomics in healthy ageing and healthy longevity medicine. *Ageing Res Rev* **100**, 102432 (2024).
130. M. Kadyrov, L. Whiley, B. Brown, K. I. Erickson, E. Holmes, Associations of the Lipidome with Ageing, Cognitive Decline and Exercise Behaviours. *Metabolites* **12**, (2022).
131. D. Liu, N. A. Aziz, E. N. Landstra, M. M. B. Breteler, The lipidomic correlates of epigenetic aging across the adult lifespan: A population-based study. *Aging Cell* **22**, e13934 (2023).
132. I. Levental, K. R. Levental, F. A. Heberle, Lipid Rafts: Controversies Resolved, Mysteries Remain. *Trends Cell Biol* **30**, 341-353 (2020).
133. E. Alvarez, V. Ruiz-Gutierrez, F. Sobrino, C. Santa-Maria, Age-related changes in membrane lipid composition, fluidity and respiratory burst in rat peritoneal neutrophils. *Clin Exp Immunol* **124**, 95-102 (2001).
134. J. M. Noble, T. H. Thomas, G. A. Ford, Effect of age on plasma membrane asymmetry and membrane fluidity in human leukocytes and platelets. *J Gerontol A Biol Sci Med Sci* **54**, M601-606 (1999).
135. A. Martin-Segura *et al.*, Age-associated cholesterol reduction triggers brain insulin resistance by facilitating ligand-independent receptor activation and pathway desensitization. *Aging Cell* **18**, e12932 (2019).
136. G. E. Atilla-Gokcumen *et al.*, Dividing cells regulate their lipid composition and localization. *Cell* **156**, 428-439 (2014).
137. T. C. von Erlach *et al.*, Cell-geometry-dependent changes in plasma membrane order direct stem cell signalling and fate. *Nat Mater* **17**, 237-242 (2018).
138. J. H. Lorent, I. Levental, Structural determinants of protein partitioning into ordered membrane domains and lipid rafts. *Chem Phys Lipids* **192**, 23-32 (2015).
139. T. Sych, K. R. Levental, E. Sezgin, Lipid-Protein Interactions in Plasma Membrane Organization and Function. *Annu Rev Biophys*, (2022).
140. G. S. Roth, J. A. Joseph, R. P. Mason, Membrane alterations as causes of impaired signal transduction in Alzheimer's disease and aging. *Trends Neurosci* **18**, 203-206 (1995).
141. A. Flohr Svendsen *et al.*, A comprehensive transcriptome signature of murine hematopoietic stem cell aging. *Blood* **138**, 439-451 (2021).

142. A. J. Hulbert, The links between membrane composition, metabolic rate and lifespan. *Comp Biochem Physiol A Mol Integr Physiol* **150**, 196-203 (2008).
143. C. Fabiani, S. S. Antollini, Alzheimer's Disease as a Membrane Disorder: Spatial Cross-Talk Among Beta-Amyloid Peptides, Nicotinic Acetylcholine Receptors and Lipid Rafts. *Front Cell Neurosci* **13**, 309 (2019).
144. D. Liang *et al.*, Ferroptosis surveillance independent of GPX4 and differentially regulated by sex hormones. *Cell* **186**, 2748-2764 e2722 (2023).
145. B. Wang *et al.*, Phospholipid Remodeling and Cholesterol Availability Regulate Intestinal Stemness and Tumorigenesis. *Cell Stem Cell* **22**, 206-220 e204 (2018).
146. J. Bi *et al.*, Oncogene Amplification in Growth Factor Signaling Pathways Renders Cancers Dependent on Membrane Lipid Remodeling. *Cell Metab* **30**, 525-538 e528 (2019).
147. B. Wang, P. Tontonoz, Phospholipid Remodeling in Physiology and Disease. *Annu Rev Physiol* **81**, 165-188 (2019).
148. K. Thabet *et al.*, MBOAT7 rs641738 increases risk of liver inflammation and transition to fibrosis in chronic hepatitis C. *Nat Commun* **7**, 12757 (2016).
149. M. Meroni, M. Longo, A. L. Fracanzani, P. Dongiovanni, MBOAT7 down-regulation by genetic and environmental factors predisposes to MAFLD. *EBioMedicine* **57**, 102866 (2020).
150. D. Chen *et al.*, The lipid elongation enzyme ELOVL2 is a molecular regulator of aging in the retina. *Aging Cell* **19**, e13100 (2020).
151. H. Tsugawa *et al.*, A lipidome landscape of aging in mice. *Nat Aging* **4**, 709-726 (2024).

Methods

Laboratory animals

Male C57BL/6JN mice (hereafter C57BL/6) obtained from the NIA Aged Rodent colony were used in all experiments. NIA C57BL/6JN mice were habituated for more than two weeks at Stanford before use. All mice were housed in the Comparative Medicine and Neuroscience-ChemH building vivarium at Stanford, and their care was monitored by the Veterinary Service Center at Stanford University under IACUC protocol 8661.

Primary cultures of quiescent and activated NSCs

For primary cultures of mouse NSCs, NSCs were isolated from male C57BL/6 mice as previously described (*1-5*). Briefly, subventricular zones (SVZs) from each brain were microdissected and finely minced. Tissue suspension was then digested for 35min at 37°C with gentle agitation in HBSS media (Corning, 21-021-CV) containing 2U/ml Papain (Worthington LS003124), 1U/ml Dispase II (STEMCELL Technologies, 07913), and 0.1mg/ml DNase I (Sigma, DN25-100mg), and mechanically dissociated. Isolated cells were expanded as neurospheres in culture in "Proliferative NSC media" (NeuroBasal-A medium (Gibco, 10888-022) with penicillin-streptomycin-glutamine diluted 1X (Gibco, 10378-016), 2% B27 minus vitamin A (Gibco, 12587-010), 20ng/ml bFGF (Peprotech, 100-18B) and 20ng/ml EGF (Peprotech, AF-100-15)) at 37°C in 5% CO_2 and 20% O_2 at 95% humidity.

We then generated quiescent NSCs (qNSCs) and activated NSCs (aNSCs) following published protocol (*6*). The number of plated cells for qNSCs and aNSCs was optimized to ensure similar cell number ($1x10^6$) at the time of harvesting (see below). We also verified NSC

culture purity by immunofluorescence staining with the NSC/astrocyte marker glial fibrillary acidic protein (GFAP).

To generate primary cultures of quiescent NSCs (qNSCs) (*6*), tissue culture plates were pre-treated with PBS (Corning, 21-040-CV) containing 50ng/ml Poly-D-Lysine (Sigma-Aldrich, P6407) for 2 hours in 37°C tissue culture incubator, and then washed 3 times with PBS prior to plating cells. Next, 900,000 NSCs (passage 3 to passage 5) were plated in each well of a 6-well plate (~94,000 cells/cm^2) and were cultured in "Quiescence NSC media" (NeuroBasal-A (Gibco, 10888-022), penicillin-streptomycin-glutamine 1X (Gibco, 10378-016), 2% B27 minus vitamin A (Gibco, 12587-010), 20ng/ml bFGF (Peprotech, 100-18B) and 50ng/ml BMP4 (Biolegend, 595302). qNSC cultures were incubated in this quiescence media for 7 days, with media change every 2 days before being used for lipidomics experiment. These conditions led to ~$1x10^6$ qNSCs at the time of harvesting.

To generate primary cultures of aNSCs, 700,000 NSCs (passage 3 to passage 5) were plated in each well of a 6-well plate (~74,000 cells/cm^2) pre-treated with poly-D-lysine as described above. Cells were then incubated in "Proliferative NSC media" (see above) for 2 days before being used for lipidomic analysis. These conditions led to ~$1x10^6$ aNSCs at the time of harvesting.

Primary qNSC and aNSC sample preparation for lipidomics

For lipidomics of primary qNSCs and aNSCs, cells were washed twice with PBS before incubating in "Quiescent NSC media" minus B27 supplement and "Proliferative NSC media" minus B27 supplement, respectively. Cells were incubated for 3 hours in these media at 37°C incubator with 5% CO_2 and 20% oxygen at 95% humidity to remove exogenous lipids contained

in B27 supplement. At the end of the incubation period, cells were washed once with PBS (Corning, 21-040-CV) and scraped into 500µl of ice-cold PBS using cell lifter (Fisher Scientific 07-200-364). The cell suspension was collected in 2ml amber glass vials (Thermo Scientific, 03-FISVA) sealed with polyethylene cap with PTFE/silicone septum (Waters, 186000274). All samples were immediately snap-frozen in liquid nitrogen and stored at -80°C.

Design of the "*In vitro* #1" lipidomic experiment

The "*In vitro* #1" lipidomic LC-MS/MS experiment was conducted on n=4-5 young and n=4-5 old primary cultures of qNSCs and aNSCs (each originating from an individual mouse), each at $1x10^6$ cells per sample at collection time. A mixture of 14 internal standards was used and added prior to extraction (see "*Lipid extraction*" below). This mixture consisted in 13 deuterated standards (EquiSPLASH® mix, Avanti Polar Lipids, 330731) (1µl/sample) and Cholesterol (d7) (Avanti Polar Lipids, 700041) (0.2µl/sample). See **Table S3** (lipids identified in this lipidomic experiment).

Lipid extraction

Lipids were extracted from cell suspension thawed on ice using a 2-phase, liquid-liquid extraction system – a modified Folch method (*7*). Internal standards were added prior to extraction. All chemical reagents used were LC-MS grade unless indicated otherwise. Specifically, 300µl of cold 100% methanol (Fisher Scientific, A456-500) containing 14 deuterated internal lipid standards was added to the cell suspension. Homogenates were sonicated three times for 30s each time at room temperature in a water bath sonicator (VWR, 97043-960). Samples were placed on ice for 30s between each cycle. Following this step, 600µl of cold chloroform (Acros Organics, AC610281000, stored at -20°C) was added to the homogenates. Samples were then subjected to vigorous vortex at 4°C for 30min. Biphasic

separation was achieved after centrifugation at 3000rpm for 10min at 4°C. The lower organic phase containing the lipids was collected and dried down under a nitrogen stream using a TurboVap Classic LV (Biotage) at a flow rate of 0.5l/min for 15min until no visible solution remained and a dried lipid film formed at the bottom. Dried lipids were then resolubilized in 200µl 100% methanol at room temperature before moving to -20°C for storage for 1-7 days before analysis. On the day of the lipidomic analysis, each sample's lipid extract was dried down under a nitrogen stream and resolubilized in 200µl of methanol:toluene (90:10, vol:vol).

LC-MS/MS lipidomics

Lipidomics workflow, including sample preparation, experimental platform and detailed lipid identification, and quantification parameters for each lipid class are included in the accompanying reporting checklist (**Table S1**) recommended by the Lipidomics Standard Initiative (LSI) (*8*). Lipid extracts were analyzed by untargeted LC-MS/MS in a randomized order using an Ultimate 3000 RSLC system coupled with a Q Exactive mass spectrometer (Thermo Scientific) as previously described (*9*). Data from each sample was acquired in positive and negative ionization modes. Lipids were separated using an Accucore C18 column 2.1 x 150mm, 2.6µm (Thermo Scientific, 17126-152130).

A 31-minute chromatography gradient with the following mobile phase was used as previously reported (*9*). Specifically, we used mobile phase of 10mM ammonium acetate and 0.1% formic acid in 60/40 acetonitrile/water (A) and 10mM ammonium acetate and 0.1% formic acid in 90/10 isopropanol/acetonitrile (B). The gradient profile used was 30% B for 3min (0-3min), 30-43% in 2min (3-5min), 43-55% B in 0.1min (5-5.1min), 55-65% in 9.9min (5.1-15min), 65-85% B in 6min (15-21min), 85-100% B in 2min (21-23min), 100% B for 5min (23-28min), return to 30% B in 0.1min (28-28.1min) and 30% B for another 2.9mins (28.1-31min).

Lipids were eluted from the column at 0.4ml/min, the oven temperature was set at 45°C, and the injection volume was 5µl. Autosampler temperature was set at 20°C to prevent lipid aggregation.

Each sample was run in full MS mode. The mass resolution at *m/z* 200 was 70,000 in full MS mode. Scan range was set at 100 to 1500 *m/z*, with AGC target set at $1x10^6$, maximum injection time at 100ms. MS/MS spectra were acquired on pooled samples on Q Exactive mass spectrometer equipped with a HESI-II probe and operated in data-dependent acquisition (DDA) mode. DDA tandem mass spectrometry was set with the following parameters: mass resolution at 35,000, scan range at 200 to 2000 *m/z*, with AGC target set at $1x10^5$, maximum injection time at 50ms. Minimum AGC target set at $1x10^3$ and intensity threshold set at $2x10^4$. Loop count and TopN both set at 10. A stepped normalized collision energy was set at 25% and 30%. Dynamic exclusion was set at 12s. Mass window for precursor ion isolation was set at 1 Da.

Quality control

Data quality was ensured by 1) injecting pooled sample with deuterated standards 6 times to equilibrate the LC-MS system prior to running the sequence, 2) checking mass accuracy, retention time, and peak shape of deuterated standards in each injection of pooled sample, 3) ensuring that pooled samples with deuterated standards were injected after every 10-15 sample acquisitions throughout the entire experiment to ensure the stability of the instrument. Precision of the method was evaluated by calculating the coefficient of variation (CV) of all deuterated standards from pooled samples after every 10-15 sample acquisitions throughout each experiment. Calculated CVs of all internal standards in reported studies were <10%. Retention time drift was monitored by plotting the retention time of internal standards in pooled samples in the order of acquisition. Calculated retention time drift was between 0.1-0.15 minutes.

Lipid identification

MS-DIAL version 5.5.250221 software was used for deconvolution, peak picking, alignment, and compound identification (*10*). The parameter settings were: MS1 tolerance, 0.01 Da; MS2 tolerance, 0.025 Da; minimum peak height, 1,000 amplitude; mass slice width, 0.05 Da; smoothing method, linear weighted moving average; smoothing level, 3 scans; minimum peak width, 5 scans. Positive ion mode adducts included: $[M+H]^+$, $[M+NH4]^+$, $[M+Na]^+$ and $[M+H-H2O]^+$. Negative ion mode adducts included: $[M-H]^-$, $[M+HCOO]^-$ and $[M+CH3COO]^-$. Although both ammonium acetate and formic acid were used in our mobile phase, we predominantly used formate adduct $[M+HCOO]^-$ for lipid identification as it is more stable and provide cleaner spectra for identifying complex lipid classes. Similar observations were made in another study using the same mobile phase modifiers (*11*). Only metabolic features present in >2/3 of all samples were kept for further analysis. Lipids were identified by matching the precursor ion mass and tandem mass spectra to a spectral library included in MS-DIAL (Msp20250218112233_NCDK_conventional_converted_dev) with settings listed above.

All identified lipids were reported at the molecular species level. The most abundant ion adduct was selected for each lipid class for downstream analysis and quantification. Specifically, in positive mode, $[M+H]^+$ for Lysophosphatidylcholine (LPC), Phosphatidylcholine (PC), Phosphatidylethanolamine (PE), Sphingomyelin (SM), $[M+NH4]^+$ for Monoacylglycerol (MG), Diacylglycerol (DG) and Triacylglycerol (TG), $[M+H-H2O]^+$ for Ceramide (Cer) and Cholesterol. In negative mode, $[M-H]^-$ for Lysophosphatidylethanolamine (LPE), Phosphatidylinositol (PI), Phosphatidylserine (PS), Phosphatidylglycerol (PG). All reported lipids were quantified at level 2 according to the Lipidomics Standard Initiative (LSI) guideline.

To reduce the risk of misidentification, MS/MS spectra from all lipids were manually investigated to validate lipid annotation. See **Table S2** for spectra ions used in the manual

validation of all lipid classes. The manual validation consisted in verifying that: 1) both positive and negative mode MS/MS spectra matched the expected fragments, 2) the main lipid adduct forms detected in positive and negative modes were in an agreement with the lipid class identified, 3) the retention time was compatible with the lipid class identified, 4) the peak shape shows symmetrical, Gaussian pattern and 5) the fragmentation pattern of each lipid class detected was experimentally validated using lipid internal standards. Accurate mass and MS/MS spectra from pooled samples were used for lipid identification and manual validation. Lipid species from individual samples were annotated based on accurate mass and retention time alignment to validated lipids identified from pooled samples.

Lipid quantification

Endogenous lipids were reported in molar concentrations based on the intensity ratio between endogenous lipids and the deuterated lipid standard within the same lipid class with known concentration. The inclusion of 14 internal standards from the EquiSPLASH® deuterated lipid standard mix (see above) allowed us to obtain relative quantification in molar concentration in 14 lipid classes (PC, LPC, PE, LPE, PG, PI, PS, TG, DG, MG, ChE, Cer, SM, cholesterol). As all samples have a similar number of input cells ($1x10^6$ cells for both qNSCs and aNSCs at the time of harvesting) (see "*Primary cultures of quiescent and activated NSCs*"), each lipid concentration was normalized using the median lipid molar concentration (instead of total or average concentration to reduce sensitivity to outlier high-abundance lipids) from all lipids of each sample. Prior to the lipidomic quantification, we conducted an optimization experiment on a mix from young and old qNSC and aNSC samples (to represent sample matrices) with a serial dilution of EquiSPLASH and Cholesterol (d7) deuterated standards spanning 5 orders of

magnitude to ensure that the introduced concentration of all standards were within the linear detection range of endogenous lipids in qNSCs and aNSCs.

Reporting

Raw lipidomic data were uploaded to Metabolomicsworkbench.org under StudyID: ST002258, ST002259, ST002260, ST004116 and ST004117. The metadata and the summary of quantification and identification data are all available for download.

Nomenclature

Lipid nomenclature used followed the guideline of LIPID MAPS (*12*). The number of C=C bonds was indicated by the number after the carbon number in the acyl chain and was separated by ":". The separator "_" was used between the two acyl chains if sn-position of the fatty acids was not known. The separator "/" was used when sn-position of fatty acids was proven (e.g., sn-1/ sn-2 or sn-2/ sn-3 for glycerophospholipids). Using our mass spectrometry setup, alkyl-linked LPE and LPC species (e.g. LPE(O-18:1)) exhibited the same tandem mass spectra as alkenyl-linked LPE and LPC species with 1 less double bond (e.g. LPE(P-18:0), as previously reported (*13*). For those species, both annotations are listed and separated by "/" (e.g. LPE(O-18:1)/LPE(P-18:0)). To distinguish between isomeric lipids, lipids with identical molecular formulas but different structures, an identifier (a, b, or c) was added at the end of each lipid annotation. Only isomer lipids within the same retention time window of (+/- 0.1 minute) across different experiments were considered to have the same identification and included in cross-study experiments.

Design of "*In vitro* #2" lipidomic experiment

The "*In vitro* #2" lipidomic LC-MS/MS experiment was conducted on n=4 young and n=4 old primary cultures of qNSCs, each originating from an individual mouse, for a total of $1x10^6$ cells per sample at collection time. In this experiment, qNSCs were transduced with control lentivirus or lentivirus expressing sgRNA targeting genes of interest (*Elovl5*, *Mboat2*, *Agpat3*, *Pla2g4e* and *Fads2*). See below "Lipidomic dataset of CRISPR/Cas9-mediated knockouts *in vitro* of *Mboat2*, *Elovl5*, *Agpat3*, *Fads2*, *Pla2g4e* in young and old qNSCs". This experiment was used both in Figure 1 (control) and Figure 4 (control vs. lipid enzyme gene knockouts). See **Table S1** (internal standards) and **Tables S3 and S9** (lipids identified in this lipidomic experiment). This experiment was conducted as described above for "*In vitro* lipidomic experiment", with the following modifications:

1. For standards, we included a mixture containing the same 13 deuterated standards (EquiSPLASH® mix, Avanti Polar Lipids, 330731), but we also included a deuterated oleic acid standard (Cayman Chemical, 9000432) (1µl/sample) and no cholesterol standard. We refer to it as "13 lipid classes".
2. For this experiment, each sample was run in full MS mode and MS/MS spectra were acquired in individual samples (instead of in pooled samples as in all other studies) on a Q Exactive mass spectrometer equipped with a HESI-II probe and operated in data-dependent acquisition mode.
3. Free fatty acids were analyzed in a randomized order using an Ultimate 3000 RSLC system coupled with a Q Exactive mass spectrometer (Thermo Scientific). The Q Exactive was operated in data-dependent acquisition mode in negative ionization mode. Free fatty acids were separated on a Zorbax StableBond aq column (dimension: 2.1mm x 50mm, particle size: 1.8µm) (Agilent technologies, 827700–914) at 0.6ml/min using a mobile phase solvent consisted of

0.06% acetic acid in water (A) and 0.06% acetic acid in acetonitrile (B). The gradient was set with 1-90%B in 9min, the oven temperature was set at 60°C, the autosampler temperature was set at 4°C, and the injection volume was 15µl. Single-point internal standard calibration with deuterated oleic acid (Cayman Chemical, 9000432) was used to estimate absolute concentrations for all free fatty acids in this experiment.

Overlapping lipids between *in vitro* lipidomic datasets

Overlapping detected lipids between *in vitro* lipidomic datasets were identified using the annotated molecule identification (see "*Lipid identification*" for details). A lipid species was labelled as "overlapping" if it was detected in independent datasets. A Venn diagram was drawn with the size of each area proportional to the number of lipids using function "euler" with R package "eulerr" v7.0.2.

To determine the abundance of overlapping detected lipids based on molar concentration, we calculated the percentage of molar concentration of commonly identified lipids (summing the concentration of overlapping lipids and dividing this sum by the total lipid concentration of each sample) as well as of lipids that were uniquely detected in individual datasets. We presented these percentages of molar concentration of lipids using a stacked bar plot.

We also assessed overlapping lipids that show the same direction of age-related changes. Lipids from the different datasets were first divided into "up with age" or "down with age" groups based on the age-related log2 fold change, calculated as the log2-transformed ratio between the mean lipid concentration of old vs. young samples. Lipids are categorized as "up with age" or "down with age" have a positive or negative age-related log2 fold change,

respectively. Overlapping lipids were then identified as described above from the "up with age" or "down with age" groups. All overlapping lipids are included in **Table S4**.

There was some variability between *in vitro* datasets, for detected lipids and for age-related changes. Some of the variability could be biological and originate from the fact that experiments were conducted with primary cells and with different cohorts of aging mice. The variability could also be technical and due to differences in design (i.e. presence or absence of lentiviral infection), the fact that experiments were run at different times, and differences in the LC-MS/MS analysis (see above).

Comparison of lipid concentrations between *in vitro* lipidomic datasets

To compare lipid concentrations detected across both *in vitro* lipidomic datasets, we first identified overlapping lipids that were identified in these datasets (described above). We then plotted the normalized lipid concentration of each individual lipid from each dataset. Correlation coefficients and *P*-values were obtained from Pearson correlation analysis in R version 4.4.2.

Principal Component Analysis (PCA) of lipidomic datasets

Principal component analysis (PCA) was done on lipids with quantified concentration using log2 transformed normalized lipid concentration. PCA was generated using function "prcomp()" with R version 4.4.2. All PCA plots were made to visualize samples on principal component 1 (PC1) and principal component 2 (PC2) or principal component 3 (PC3). The differences between young and old qNSCs were smaller than the differences between cell states (quiescent and activated), similar to what has been observed for other molecular features (*1, 2, 5*).

PCA on combined samples from "*In vitro* #1" and "*In vitro* #2" was performed on the 175 overlapping lipids that were detected in both datasets (see "*Overlapping lipids between in vitro lipidomic datasets*" section). Z-score – a numerical value that indicates how many standard deviations a data point is away from the mean of a distribution – was calculated for each lipid based on the log2 transformed normalized concentration of both studies.

Heatmap visualization of lipids with age-related changes *in vitro*

Lipids with age-related changes in quiescent NSCs were identified by a Wilcoxon rank sum test, followed by multiple hypothesis correction using FDR (Benjamini-Hochberg correction for multiple comparisons). Lipids that change with age with FDR-adjusted $P<0.1$ were included in the "*In vitro* #1" and "*In vitro* #2" heatmaps. Heatmaps were generated from differential lipids with Pearson correlation using the R package "ComplexHeatmap" v2.22.0.

Analysis of the magnitude of age-related changes in two independent *in vitro* lipidomic experiments by calculating "effect size"

To analyze the magnitude of the changes with age across two independent *in vitro* lipidomic datasets, we used "effect size" to calculate the difference between young and old samples. Effect size is a stringent metric that integrates both fold change (numerator of the calculation) and variability within datasets (denominator of the calculation). Calculating effect size enables to compare across independent experiments, and it has been previously used for lipidomics and metabolomics (*14-16*). Hedges' *g* statistics was used to evaluate the standardized mean difference between two groups (e.g. young vs. old) for a given measurement (*17, 18*). Specifically, if one group is 1 (e.g. old) and the other group is 2 (e.g. young):

g = correction factor * ((Mean$_1$-Mean$_2$)/SD_weighted_pooled, where

SD_weighted_pooled = sqrt(((n$_1$-1)*SD$_1^2$ + (n$_2$-1)*SD$_2^2$)/(n$_1$+n$_2$-2))

A correction factor was applied to experiment with small sample size (<50 samples).

correction factor = 1-3/(4*(n$_1$+n$_2$)-9)

Throughout our study, positive values in age-related effect size calculation represented features that increased with age, and negative values represented features that decreased with age. We note that differences with age within a cell type are typically not large, and smaller than changes between cell types.

Plotting effect size means and s.e.m. and confidence intervals of specific lipids

Age-related effect sizes of individual lipids from each experiment (g) were used to calculate the mean effect size and the standard error of the mean (s.e.m.). The mean effect sizes across both *in vitro* lipidomic datasets, individual effect sizes from each dataset, and the standard errors of the mean were visualized using forest plots. Next, the 95% confidence interval was calculated as the range from (mean effect size - 1.96 * s.e.m.) to (mean effect size + 1.96 * s.e.m.). Statistical significance was assessed based on the P-value from test statistics using the 95% confidence interval of the data, and multiple hypothesis correction was done by FDR (Benjamini-Hochberg correction for multiple comparisons). Lipids that changed with age with FDR-adjusted P<0.05 were noted to be significant across both experiments.

Abundance of lipids with significant age-associated changes

Lipids were ranked based on the normalized concentration. Lipids that showed significant age-related changes in "*In vitro* #1" and "*In vitro* #2" lipidomic experiments were highlighted. Lipids that significantly changed with age spanned a range of concentration and included high abundance lipids. We note that the changes with age in low abundance lipids should be taken with caution.

Side chain composition analysis

We used the lipid class followed by side chain carbon and double bond number to indicate the composition of a given lipid class containing a specific side chain. We considered each lipid class/side chain combination as a side chain composition feature, e.g. PE(20:4). For each individual lipid class, we grouped lipids based on the presence of each unique side chain within a given class and calculated the total concentration (μM) of each side chain composition feature. Alkyl-linked LPE/LPC species and the corresponding alkenyl-linked LPE/LPC species with 1 less double bond were excluded from this analysis, due to multiple possible side chain annotations (see "*Nomenclature"*). Normalized lipid concentration was used for "*In vitro* #1" (which had 14 internal standards) and "*In vitro* #2" (which had 13 internal standards).

Comparison of molar percentage of side chain composition between 2 datasets

To compare side chain composition detected in the two *in vitro* lipidomic datasets, we first identified overlapping side chain composition features (described above) in both datasets. We then plotted the molar concentration of each side chain feature from each dataset. Correlation coefficients and *P*-values were obtained from Pearson correlation analysis in R version 4.4.2.

Plotting effect size means and s.e.m. and confidence intervals of specific side chain features

Age-related effect sizes of side chain features from each experiment (g) were used to calculate the mean effect size and the standard error of the mean (s.e.m.). The mean effect sizes across both *in vitro* lipidomic datasets, individual effect sizes from each dataset, and the standard errors of the mean were visualized using forest plots. Next, 95% confidence interval was determined as the range from (mean effect size - 1.96 * s.e.m.) to (mean effect size + 1.96 * s.e.m.). Statistical significance was assessed based on the P-value from test statistics using the 95% confidence interval of the data, and multiple hypothesis correction was done by FDR (Benjamini-Hochberg correction for multiple comparisons). Side chain features that changed with age with FDR-adjusted $P<0.05$ were noted to be significant across both experiments.

Abundance of side chain composition features with significant age-associated changes

Features were ranked based on molar concentration of each feature across all lipid classes. Features that showed significant age-related changes in "*In vitro* #1" and "*In vitro* #2" lipidomic experiments were highlighted. The side chain composition features that showed significant changes with age included features that spanned a range of molar concentrations within each experiment.

Design of "*In vivo*" qNSC lipidomic experiment

To isolate qNSCs directly from mouse brain, we used fluorescence-activated cell sorting (FACS) (*1, 2*). This experiment was performed on n=6 young and n=6 old qNSC samples. For each of these 6 samples, we pooled 5 young mice or 5 old mice to obtain ~7,500-9,000 freshly isolated qNSCs for each biological replicate. Briefly, the subventricular zones (SVZs) of young (3-5 month-old) and old (20-22 month-old) C57BL/6 male mice were micro-dissected following a previously published protocol (*19*). Single cell suspension was obtained and then stained with

1:50 CD31 (BioLegend, 102405), 1:50 CD45 (BioLegend, 103108), 1:50 CD24 (BioLegend, 101805), 1:300 Prominin-1-biotin (Thermo Scientific, 13-1331-82) and 1:300 EGF-Alexa 647 (Molecular probes, E35351) for 30min on ice. Cells were then stained with 1:1000 Streptavidin-PEcy7 (eBioscience, 25-4317) for 30min on ice. Quiescent NSCs ($CD31^-CD45^-CD24^-$ Prominin-1$(CD133)^+EGFR^-$) were sorted. All FACS sorting was performed at the Stanford FACS facility on a BD Aria sorter, using a 100μm nozzle at a pressure of 13 psi. We note that the tandem dye PE-Cy7 we used (conjugated to Prominin-1 antibody) has a broad emission spectrum and extends into the far-red range (~660 nm), which overlaps with the AF647 (EGF) detection channel even though they are excited by different lasers. Correlated signal between PE-Cy7 and AF647 still persisted even after spectral compensation was applied. Signal correlation between PE-Cy7-conjugated Prominin-1 and AF647-conjugated EGF was also observed, albeit in a less pronounced manner, in previous studies (*2, 19*). The greater spill-over we observed in our experiments may due to the fact that we used FITC for all 3 lineage-specific markers (CD45, CD31 and CD24), whereas prior studies used a distinct fluorophore for each marker (*2, 19*). Because FITC and PE-Cy7 are excited by the same 488nm laser on the BD Aria sorter, FITC emission can spill into the PE-Cy7 detector, which may exacerbate the correlated signal between PE-Cy7 and AF647. We also note that all compensations were done on single-color staining controls of SVZ cells, and we then used FMO (fluorescence minus one) controls to take into account the residual spectral spillover and inform us on the gating of populations of interests. qNSCs of each sample (pooled from 5 young or old mice) were sorted into 500μl of ice-cold PBS, and the cell suspension was immediately snap-frozen in liquid nitrogen and then transferred to -80°C for storage.

As described above, a mixture containing 13 deuterated standards (EquiSPLASH® mix, Avanti Polar Lipids, 330731) was added to each sample (0.5µl/sample), together with 0.1µl/sample of Cholesterol (d7) (Avanti Polar Lipids, 700041) (**Table S1**).

This experiment followed the exact same procedures as outlined for "*In vitro* #1*"* lipidomics. The low number of cells for the *in vivo* lipidomic dataset led to a smaller number of total detected lipids, and thereby fewer significant lipids between young and old. For the *in vivo* lipidomic heatmap, all identified lipids were included (no multiple hypothesis correction).

Overlapping lipids between *in vitro* and *in vivo* experiments were evaluated as described above for different *in vitro* lipidomic experiments (we used "*In vitro* #1" for the overlap with "*In vivo*"). We note that the low overlap between *in vivo* and *in vitro* lipidomic studies likely originate from the low cell number in *in vivo* experiments. In addition, *in vitro* qNSC cultures might not recapitulate all features of freshly isolated qNSCs (especially non-cell intrinsic or compensatory features).

Identification of lipid and side chain composition changes with age in qNSCs *in vitro* and *in vivo*

Effect sizes with age from lipidomic data of "*In vitro* #1" and "*In vivo*" were used to compute the mean overall effect size and the standard error of the mean from *in vitro* and *in vivo* studies. Next, 95% confidence interval was determined as the range from (mean effect size - 1.96 * s.e.m.) to (mean effect size + 1.96 * s.e.m.). Statistical significance was assessed based on the *P*-value from test statistics using the 95% confidence interval of the data, and multiple hypothesis correction was done by FDR (Benjamini-Hochberg correction for multiple comparisons). Lipids

and side chain features that change with age with FDR-adjusted $P<0.05$ were noted to be significant across *in vitro* and *in vivo* studies.

SVZ sample preparation for Desorption Electrospray Ionization Mass Spectrometry Imaging (DESI-MSI)

For lipidomics *in situ* (in the context of intact tissue), we used Desorption Electrospray Ionization Mass Spectrometry Imaging (DESI-MSI). For these experiments, SVZ neurogenic niches were micro-dissected from n=7 young (3-5 month-old) and n=7 old (20-22 month-old) C57BL/6 male mice brains. Each microdissected SVZ niche was oriented on a cryomold (Fisher scientific, NC9511236) such that the lateral wall of the SVZ faced down to flatten the tissue, and then each sample was immediately snap-frozen on dry ice. For cutting, SVZs were not embedded in optimal cutting temperature (OCT) polymeric compound to avoid background compound peaks from residual OCT during tissue sectioning. Instead, a minimal amount of OCT was applied to attach the caudoputamen, which is adjacent to the lateral wall of the SVZ, to the mounting plate before sectioning. Unfixed SVZs were cut into 16µm sections parallel to the lateral wall of the SVZ at -20°C on a Leica CM3050S cryostat. Sections were thaw-mounted onto slides (Fisher scientific, 12-550-15) without fixation, before transferring to -80°C for storage. Tissue slides were dried for 20min at room temperature using a vacuum desiccator (Thermo scientific, 5311-0250) before DESI-MSI experiments.

DESI-MSI

We used Desorption Electrospray Ionization Mass Spectrometry Imaging (DESI-MSI) to determine if some of the lipid changes with age were also observed *in situ*, in intact neurogenic niches. For DESI-MSI, we used a procedure that we previously published (*20*) on sections of

SVZ whole mount to assess cell layers that are immediately adjacent to the ventricle, where a high density of NSCs reside. Briefly, a custom-built DESI imaging stage was coupled to a hybrid LTQ-Orbitrap mass spectrometer (Thermo Fisher Scientific) for DESI-MSI. The mass spectra were acquired in the negative ion mode from *m/z* 50−1000 using the Orbitrap mass analyzer with the resolving power set at 60,000. The spray voltage was set to −3.5kV, and the capillary voltage was set to −65V. The tube lens voltage was set to −120V. Ion injection time was 100ms, and one microscan was performed. The solvent system used was *N*,*N*-dimethylformamide (DMF)/ acetonitrile (ACN) = 1:1 (vol/vol) and was provided at a flow rate of 0.8µl/min. Assisted by a nebulizing gas (N_2) at a pressure of 150psi, molecules of interest from tissues are desorbed and ionized. DESI spray tip-to-surface distance was 2mm; spray incident angle was 56°, and spray-to-inlet distance was 6.5µm. Step size in the moving stage was set to 200µm, and automatic gain control of mass spectrometer was switched off. These parameters were empirically found to yield the optimal MS signal from brain tissues. Tandem mass spectra were obtained using collision-induced dissociation from the ion trap mass analyzer to validate lipid structures based on their characteristic fragment ions. All experiments were carried out under identical experimental conditions to allow comparison between measurements.

Immunofluorescence staining and imaging for DESI-MSI

To gain cellular resolution, we performed immunofluorescence staining on the exact same sections used for DESI-MSI. After each DESI scan, tissue sections were fixed with 4% paraformaldehyde (Electron Microscopy Science, 15714) diluted in phosphate-buffered saline for 20min at −20°C. Antibodies against Glial Fibrillary Acidic Protein (GFAP) (Abcam, ab53554, RRID:AB_880202) were used at 1:1000 dilution, antibodies against Ki67 (eBioscience, SolA15, RRID:AB_10854564) were used at 1:500 dilution at 4°C overnight.

Donkey anti-goat antibodies conjugated with Alexa Fluor 647 (Thermo Fisher Scientific, A-21447, RRID:AB_141844), and donkey anti-rat antibodies with Alexa Fluor 488 (Thermo Fisher Scientific, A-21208, RRID:AB_2535794) was used at 1:250 dilution at room temperature for 1.5h for a secondary staining. All sections were mounted with 50µl of ProLong Gold Antifade mounting media containing a fluorescent nucleic acid dye 4′,6- diamidino-2-phenylindole (DAPI) (Thermo Fisher Scientific, P36931) before imaging. Confocal microscopy was carried out using a Nikon Eclipse Ti confocal microscope equipped with a Zyla sCMOS camera (Andor) and NIS-Elements software (AR 4.30.02, 64-bit) using a 10X objective. A tiled image covering the entire area of SVZ was taken for each mouse.

Image quantification for DESI-MSI

To quantify the immunofluorescence images in order to obtain cell type composition for downstream lipidomic deconvolution, we used a Julia language script, as we have previously reported in our previous publication (*20*). Briefly, detection of nuclei was performed for immunofluorescence-stained regions of tissue using DAPI as a nuclear marker and blob detection algorithms provided by the Julia package Images.jl. After nuclei detection, cells were classified as either GFAP-positive and Ki67-positive (activated NSCs), GFAP-positive and Ki67-negative (qNSCs/astrocytes), GFAP-negative and Ki67-positive (neural progenitor cells) and GFAP-negative and Ki67-negative (likely neurons), based upon the staining in the region immediately surrounding the detected nuclei. To threshold between these binary designations, we used Otsu's method (*21*) on the summed staining intensity for a given channel by cell. After each cell was classified and binned into a category based upon the calculated threshold, each region's proportion of cell types was calculated and presented as a percentage of total cells in that region for downstream analysis.

Cell type-specific deconvolution of DESI-MSI mass spectra

To perform cell-type specific deconvolution of DESI-MSI mass spectra, we used a similar method to that we previously published to obtain astrocyte- and neuron-specific lipidomic profiles in brain sections with cell heterogeneity, validating it with signature metabolites that are known to be characteristic to each cell type (*20*). DESI-MSI scans of the SVZ have a resolution of 200μm x 200μm and these areas in general contain a mixed population of 150-250 cells (qNSCs, aNSCs, neural progenitor cells, astrocytes, and other cell types). For cell type-specific deconvolution, peak intensity of each individual DESI scan was normalized by dividing each peak by the intensity value of an exogenous standard (4-methoxybenzoic acid) introduced by the solvent system. We then aggregated all normalized peak intensities by rounding their *m/z* value by its first significant digit to reduce data sparsity prior to deconvolution. We estimated cell-type specific intensity values using the csSAM package (version 1.2.4) (*22*) by pairing normalized DESI data with cellular proportions quantified by immunofluorescent staining on the same sample of the 4 cell types (qNSCs/astrocytes, activated NSCs, neural progenitor cells and likely neurons), as described in the section above. Specifically, we grouped all scans obtained from the same animal to estimate mean and standard error of the mean (s.e.m.) across all peaks for each mouse. We then used cell-type specific mean intensities for statistical comparisons and downstream analyses between SVZ niches, each from an individual mouse. Fold change differences between old and young mice were estimated by computing Hedges' *g* effect size (described above) using age groups as class labels.

Evaluation of cell type-specific lipidomic deconvolution accuracy

To validate the accuracy of cell type-specific deconvolution by csSAM, we generated a reconstituted *in silico* mixture lipidomic dataset. To mimic the 4-way deconvolution applied to our DESI-MSI data, we used lipidomic data from 4 different cell types: qNSCs and aNSCs (from *In vitro* #1 lipidomic dataset) as well as neurons and oligodendrocytes from an untargeted lipidomic data from a previously published paper (*23*). We then reconstituted mixture lipidomic data to simulate our DESI-MSI data samples. Specifically, we grouped one spectra from each cell type to generate an unique *in silico* lipidomic profile representing an individual mouse. We then created 10 mixtures for each mouse by combining the spectra of 4 cell types using a different vector of cell-type proportion for each mixture. We performed deconvolution on these reconstituted mixture lipidomic data, and obtained estimated mean levels of cell-type specific metabolite intensity for each individual mouse. Finally, we compared mean estimated metabolite intensity after deconvolution to the measured metabolite intensity prior to mixing by Pearson correlation. As a negative control, we also performed deconvolution using the same set of reconstituted *in silico* mixture but with mismatched cell type proportions instead. Specifically, we performed deconvolution with randomly generated cell type compositions from 100 permutation experiments. We then analyzed the distribution of the Pearson correlation coefficient between the measured and estimated lipid intensity for each cell type of each individual mouse after deconvolution.

Orthogonal partial least squares - discriminant analysis (OPLS-DA) and assessment of model performance

OPLS-DA is a supervised statistical method used to analyze multivariate data with the goal of identifying differences between predefined groups (*24*). This supervised dimensionality reduction model is often used in metabolomics because it is well suited to handle highly

correlated metabolites (e.g. metabolites in the same pathway) (*24*). After obtaining cell type-specific lipidomic data from each individual mouse by DESI-MSI followed by *in silico* deconvolution, we performed OPLS-DA to identify cell type-specific lipidomic changes between qNSCs/astrocytes and aNSCs, and in a separate analysis, between young and old qNSCs/astrocytes *in situ*. We used 'opls' function from ropls package (version 1.22.0) with the following parameters: predI = 1, orthoI = 1, crossvalI = 6, permI = 100, scaleC = 'standard'. OPLS-DA model was visualized by plotting each individual data point using the predictive score which captures the variation in the data that is correlated with sample classification (cell type or age), and the orthogonal predictive score that captures the variation in the data that is uncorrelated with sample classification (i.e., structured noise).

Model predictability was assessed by performing 100 permutation tests with sample classification randomly assigned. The predictability (Q^2) was plotted, and the *P*-value was calculated between the original and permutated models. Low Q^2 in permuted models, in combination with a significant *P*-value, indicates that the original model is significantly better than permuted models in identifying features that are predictive in separating samples of different classes. We observed that this was the case for the OPLS-DA model to distinguish qNSCs/astrocytes vs. aNSCs (**fig. S7D**), validating that our data acquired on DESI-MSI and the accompanying analysis pipeline is able to detect cell type-specific changes. However, the OPLS-DA model to distinguish young vs. old qNSCs/astrocytes did not have a lower Q^2 for permuted models or significant *P*-value (**fig. S7F**), suggesting that this model, while able to distinguish young and old qNSCs/astrocytes, was overfitted and therefore not reliable for global analysis (though analysis of specific lipids is still feasible).

Quantification on specific lipids from DESI-MSI data in a spatially defined manner

The SVZ neurogenic niche exhibits spatial heterogeneity, with qNSCs being localized in the rostral region (*25-27*) (**Fig. 2E**). To gain a spatially-defined view of the SVZ, we obtained a large rectangular area containing all scans covering the entire SVZ area (with minimal numbers of scans without tissue coverage) for each individual SVZ (**Fig. 2E**). We then divided this large rectangular area into 3 equally-sized smaller rectangles along the rostral-caudal axis of the SVZ (**Fig. 2E**). We then quantified the total normalized intensity of a given lipid from all scans of each smaller rectangle. The lipid intensity represents the metabolite abundance from all cells (not just qNSCs) contained in the scan.

Giant plasma membrane vesicle (GPMV) generation and design of "GPMV" lipidomic experiment

To determine if plasma membrane lipids contributed to complex lipid changes with age, we performed lipidomics on giant plasma membrane vesicles (GPMVs), which are mostly made of plasma membranes (without internal organelles) (*28, 29*). GPMVs were generated from primary qNSC cultures from n=8 young or n=8 old mice (each culture originating from one mouse), following a previously described protocol (*28, 29*). Specifically, $13x10^6$ qNSCs (passage 5 to passage 6) were plated in a 15cm plate (~90,000 cells/cm^2) and quiescence was induced for 7 days (as described above in "*Primary cultures of quiescent and activated NSCs*"). Cells were washed twice with "GPMV vesiculation buffer" (150mM NaCl, 2mM $CaCl_2$, and 20mM HEPES (Sigma-Aldrich, 54457) in water, pH7.4) at 37°C. GPMV generation was then induced by adding 2mM of *N*-ethylmaleimide (Sigma-Aldrich, 04259) for 1.5h in 37°C incubator with 5% CO_2 and 20% O_2, with gentle agitation every 30min. At the end of the incubation, the cell supernatants (containing GPMVs) were first subjected to a low speed centrifugation at 200g for 5min at room temperature to remove cellular debris. Supernatants (containing GPMVs) were then carefully

collected, followed by ultracentrifugation at 30,000g for 30min at 4°C using a Beckman Coulter, Optima XE-90 ultracentrifuge. After removing supernatant, pelleted GPMVs and ~500µl of residual buffer were snap frozen in liquid nitrogen and transferred to -80°C for storage.

We extracted lipids using the modified Folch method, exactly as described above for the "*In vitro* #1" lipidomic experiment. Prior to extraction, we mixed lipid extracts with internal standards mixture containing 13 deuterated standards (EquiSPLASH® mix, Avanti Polar Lipids, 330731) (0.5µl/sample), together with 0.1µl of Cholesterol (d7) (Avanti Polar Lipids, 700041) for quantification and normalization (**Table S1**). This experiment followed identical procedures as those outlined for the "*In vitro* #1*"* lipidomic experiment.

Western blot analysis

We verified the enrichment of GPMVs in plasma membrane (and depletion in internal organelle) by western blot analysis. For whole cell lysate, $13x10^6$ qNSCs (passage 5 to passage 6) were plated in a 15cm plate (~90,000 cells/cm^2) and quiescence was induced for 7 days (see above in "*Primary cultures of quiescent and activated NSCs*"). Cells were then lysed directly in the culture plates using 3ml of ice-cold 1X RIPA buffer diluted from 5X RIPA buffer (Thermo Scientific, J62524AD) with ultrapure water (Invitrogen, 10977-015) and supplemented with 1x protease inhibitor cocktail (Roche, 04693159001). Cell lysates were then scraped and transferred to Eppendorf tubes. GPMV were generated from $13x10^6$ qNSCs (passage 5 to passage 6) as described above in "*Giant plasma membrane vesicle (GPMV) generation and design of 'GPMV' lipidomic experiment*". GPMV protein lysates were obtained by lysing GPMV pellet with 50µl of 1x RIPA buffer with 1x protease inhibitor cocktail. Following the addition of Laemmli sample buffer (Alfa, Aesar, J61337), all lysates were resolved on NuPAGE 4-12% gradient Bis-Tris gel

(Invitrogen, NP0321BOX), transferred onto nitrocellulose membranes (BioRad, 162-0115) and immunoblotted. For each sample, equal amounts of total protein was loaded based on protein quantification using Ponceau S staining (see below). Primary antibodies used were: 1:25,000 Beta-actin (Abcam, Ab6276, RRID:AB_2223210), 1:5000 Calnexin (Abcam, Ab22595, RRID:AB_2069006) and 1:5000 Cox4 (Abcam, Ab16056, RRID:AB_443304). Membranes were then incubated with secondary antibody IRDye 680RD donkey anti-mouse IgG (LI-COR, 926-68072, RRID:AB_10953628), IRDye 800CW goat anti-rabbit IgG (LI-COR, 926-32211, RRID:AB_621843), or IRDye 680RD goat anti-rat IgG (LI-COR, 926-68076, RRID:AB_10956590). All secondary antibodies were used at 1:5000 dilution. Blots were imaged on Odyssey XF Imager (LI-COR).

Ponceau S staining and total protein quantification

Following protein gel transfer onto nitrocellulose membranes, the membranes were incubated in Ponceau S solution (Sigma-Aldrich, P7170-1L) for 5min at room temperature and then washed 3 times (1min each time) with Milli-Q water. The membrane was immediately scanned on an Epson perfection V300 photo scanner (model #J232B) for densitometry quantification. Using ImageJ (version 2.1.0/1.53c), the images were split into red, blue, and green channels. Equal sized rectangles were drawn around each lane, and the mean integrated density from each lane of each channel was measured. The sum of the mean integrated density from all three channels was compared to verify the same amount of protein was loaded into each lane.

Overlap, effect size, and abundance between lipids with significant age-associated changes in whole cell extracts and GPMVs

We identified the overlap between lipids in our "GPMV" lipidomic dataset (enriched for plasma membrane) and "*In vitro* #1" lipidomic dataset (whole cell extract) using the same method as described above in "*Overlapping lipids between in vitro lipidomic datasets*". We also compared the effect size of lipids and side chain features that change with age between "GPMV" and "*In vitro* #1" lipidomic datasets as described above for the comparison across *in vitro* lipidomic datasets.

For abundance, lipids were ranked based on the normalized concentration. Significant lipids in both GPMV and whole cell lipidomic data were highlighted. Many of these lipids were of high abundance, with concentration in the top 50 percentile of all lipids.

Laurdan staining and quantification of plasma membrane order *in vitro*

Membrane order was assessed by staining with the polarity-sensitive membrane probe Laurdan (6-Dodecanoyl-2-Dimethylaminonaphthalene) (Thermo Fisher Scientific, D250) (*30*-*33*). Ratiometric quantification of Laurdan at the plasma membrane provides a measure of membrane order (*33*). The Laurdan probe is excited at 405nm. The Laurdan dye fluoresces with a peak emission wavelength around 450nm (visualized in green throughout the study) when present in the ordered phase of membrane lipids and ~500nm (visualized in red throughout the study) when present in the disordered phase of membrane lipids (*33*) (**Fig. 3D**).

Specifically, 90,000 qNSCs from primary culture of young and old mice were plated in each well of 8-well chamber coverslip (90,000 cells/cm^2) (Ibidi, 80826). After 7 days of induced quiescence in quiescence media, cells were stained with Laurdan at a final concentration of 30μg/ml in culture media for 30min in 37°C tissue culture incubator. Cells were then washed once with media. DNA stain DRAQ5^{TM} (Thermo Fisher Scientific, 62251) was added at a final

concentration of 5μM in media, immediately before imaging. Live cell imaging was carried out in 37°C imaging chamber with 5% CO_2 using a Zeiss LSM980 microscope. When capturing the intensity of membrane lipids in the ordered phase, BP (bandpass) 420-480 was used. Signal obtained is referred to as $I_{420-480}$ below. When capturing the intensity of membrane lipid in the disordered phase, BP (bandpass) 465-505 and LP (longpass) 525 was used. Signal obtained is referred to as $I_{465-505}$ below. Next, 5 images from each condition were taken using 60x objective with Airyscan 2 in Multiplex mode.

We generated an automated pipeline to perform ratiometric quantification of the Laurdan data in an unbiased manner. Image analysis was performed using CellProfiler 4.1.3. Briefly, nuclei were identified with the 'IdentifyPrimaryObjects' module using global Otsu thresholding. Cellular boundaries were then identified with labelled nuclei as seeds, using propagation method within the 'IdentifySecondaryObjects' module. The outermost 10 pixels of each cellular boundary were saved as plasma membrane specific masks. Plasma membrane masks were then applied to each individual cells in Fiji (v2.1.0/1.53c).

Normalized generalized polarization ratio (GP ratio) of plasma membrane was quantified as described (*31*).

Normalized GP ratio = $(I_{420-480} - G*I_{465-505}) / (I_{420-480} + G*I_{465-505})$, where

$G = (GP_{ref} + GP_{ref}*GP_{mes} - GP_{mes} - 1) / (GP_{mes} + GP_{ref}*GP_{mes} - GP_{ref} - 1)$

$GP_{ref} = 0.207$ (*34*)

GP_{mes} was obtained from a reference image with media containing the identical concentration of Laurdan (30μg/ml) without any cells and represents the background signal intensity in both

imaging channels ($I_{420-480}$ and $I_{465-505}$). Reference images were taken in the same imaging session with identical parameters in all samples of the same experiment.

Fluorescence lifetime imaging (FLIM) *in vitro*

Membrane order was also assessed by an orthogonal approach, fluorescence lifetime imaging (FLIM) by staining of primary NSC cultures with the polarity-sensitive membrane probe di-4-ANEPPDHQ (Invitrogen, D36802) (*35, 36*). Specifically, 90,000 qNSCs (90,000 cells/cm^2) from primary culture of young and old mice were plated in each well of 8-well chamber coverslip (Ibidi, 80826). After 7 days of induced quiescence, cells were stained with di-4-ANEPPDHQ at a final concentration of 5μM in culture media for 1 hour in 37°C tissue culture incubator. FLIM imaging was carried out using a Zeiss LSM780 microscope using 60X objective. Excitation was set at 475 nm by a frequency-doubled, Mai Tai® DeepSee™ laser oscillator (Spectra-Physics). Fluorescence lifetime is the average time a fluorophore remains in the excited state before emitting a photon and returning to the ground state. It was measured using a time-correlated single photon counting (TCSPC) card (Becker & Hickl GmbH) and fitted using an incomplete multiexponential model on the SPCM software (Becker & Hickl GmbH). A longer lifetime is associated with more ordered (rigid) membrane, whereas a shorter lifetime is associated with more disordered (fluid) membrane (*37-39*).

Stratification of plasma membrane order quantification *in vitro* by cell density

As plasma membrane order assessment could be impacted by cell density, we examined this parameter in more depth. We ensured that equal number of qNSCs (90,000 cells per well of 8-well chamber coverslips, 90,000 cells/cm^2) for each condition were seeded at the beginning of all Laurdan and FLIM experiments *in vitro*. For plasma membrane order quantification by Laurdan

staining and by FLIM: 60x images were taken from different areas on the plate with varying cell density. Confocal images were then stratified based on the number of cells per image into low density (5-10 cells) and high density (15-20 cells) images. Plasma membrane order quantification on each single cell from low and high density images was assessed between young and old qNSCs.

Stratification of plasma membrane order quantification *in vitro* by cell size

As plasma membrane order assessment could be impacted by cell size, we also examined this parameter in more depth. Individual cells size was obtained using the "Area" output from CellProfiler on previously identified cell boundary (see "*Laurdan staining and quantification In vitro"* above). The median cell size from all quantified cells were identified. Each individual cell was then stratified into "small" or "large" based on whether the measured cell size is smaller or bigger than the median of all cells. Plasma membrane order quantification of individual cells from each stratified group was assessed between young and old qNSCs.

***In vivo* Laurdan staining and quantification**

For assessment of plasma membrane order in the SVZ neurogenic niche *in vivo*, we also used Laurdan – a standard approach to measure plasma membrane order (*33*). Although other imaging technologies (e.g. electron microscopy) might provide higher spatial resolution, the ability to simultaneously detect cell types with antibody staining and to perform Laurdan quantification by confocal microscopy is critical in assessing NSC-specific membrane order in the SVZ neurogenic niche. For Laurdan staining and quantification, n=5 young (3-5 month-old) and n=5 old (20-22 month-old) C57BL/6 male mice were subjected to transcardiac perfusion with 4% paraformaldehyde (Electron Microscopy Sciences, 15714) in PBS (Corning, 21-040-CV). Brains

were post-fixed overnight in 4% paraformaldehyde (Electron Microscopy Sciences, 15714) and then dehydrated in 30% sucrose (Sigma-Aldrich, S3929) for 72 hours. Brains were embedded in Tissue-Tek optimal cutting temperature (O.C.T.) compound (Electron Microscopy Sciences, 62550), sectioned into 16μm coronal slices using a cryostat (Leica CM3050S), and then mounted on glass slides (Fisher Scientific, 12-550-15). Coronal sections between Bregma 0.5mm to 1mm were generated for each mouse. We used Laurdan staining in combination with cell type markers GFAP and EGFR to quantify plasma membrane order in qNSCs/astrocytes *in vivo* and we used localization in the SVZ and morphology to focus on qNSCs (compared to niche astrocytes). Antibodies against Glial Fibrillary Acidic Protein (GFAP) (Abcam, ab53554, RRID:AB_880202) were used at 1:1000 dilution, antibodies against Epidermal Growth Factor Receptor (EGFR) (Millipore, 06-847, RRID:AB_2096607) were used at 1:200 dilution at 4°C overnight. Donkey anti-goat antibodies conjugated with Alexa Fluor 647 (Thermo Fisher Scientific, A-21447, RRID:AB_141844), and donkey anti-rabbit antibodies with Alexa Fluor 568 (Thermo Fisher Scientific, A-10042, RRID:AB_2534017) were used at 1:250 dilution at room temperature for 1.5 hours. Sections were subsequently stained with Laurdan at a final concentration of 30μg/ml for 30min at room temperature. Sections were then washed with PBS before being mounted with 50μl of Vectashield anti-fade mounting media (Vector Laboratories, H-1000-10) before being imaged. We performed single-antibody staining to verify that other stains did not interfere with Laurdan spectra. We could not evaluate the potential interference from other stains on Laurdan by performing *in viv*o Laurdan staining alone without antibody staining because cell type markers (GFAP and EGFR) were required for qNSC (and astrocyte) identification *in vivo*. Nevertheless, when we changed GFAP and EGFR antibody staining to different fluorescence channels, the quantification results on Laurdan remained the same.

Confocal imaging was carried out using a Zeiss LSM980 microscope using 60X objective with Airyscan 2 in Multiplex mode. When capturing the intensity of membrane lipids in the ordered phase, BP (bandpass) 420-480 and BP (bandpass) 495-550 was used. When capturing the intensity of membrane lipids in the disordered phase, BP (bandpass) 465-505 and LP (longpass) 525 was used. For quantification, 5 to 7 z-stacks were taken for each individual animal with 10-15 images in each stack using 0.3μm intervals between images. We first used maximum intensity projection for preliminary identification of qNSCs based on cell type markers ($GFAP^+$ $EGFR^-$) as well as spatial localization in the SVZ niche and morphology. qNSCs were identified manually using the following criteria: 1) Positive GFAP staining surrounding the entire cell body in at least two consecutive single-plane images in the stack, 2) Positive GFAP staining partially detected throughout the rest of the z-stack for the same cell, 3) Negative EGFR staining throughout all images for the same cell, 4) Localization immediately adjacent to ependymal cells that line the ventricular wall, 5) Presence of long basal process that is characteristic to qNSCs (**Fig. 3G** and **fig. S10, D and E)**. Once qNSCs were identified, plasma membrane-specific masks were hand-traced based on the GFAP staining signal immediately surrounding the cell body and apical process using Fiji (v2.1.0/1.53c). Ratiometric quantification of Laurdan staining was performed using our automated pipeline (see "*Laurdan staining and quantification in vitro*"). A normalized generalized polarization ratio (GP ratio) of plasma membrane was then generated as described in "*Laurdan staining and quantification in vitro*".

Choice of lipid-modifying enzymes for CRISPR/Cas9-based functional perturbations

For CRISPR/Cas9-based functional perturbations, we focused on 5 lipid metabolic enzymes (MBOAT2, AGPAT3, PLA2G4E, ELOVL5 and FADS2) because they are involved in the two age-dependent lipid changes we observed in our lipidomic data in qNSCs: remodeling of specific

phospholipids (MBOAT2, AGPAT3, PLA2G4E) and accumulation of PUFA-containing lipids (ELOVL5 and FADS2). All 5 enzymes satisfy 2 of the 3 following criteria: i) highly expressed in qNSCs based on our single-cell RNA-seq data (*1*), ii) significant change in expression with age (**fig. S11**), or iii) substrate specificity in support of PUFA side chain remodeling in membrane lipid classes.

Specifically:

We chose MBOAT2 because it is a phospholipid acyl transferase that remodels phospholipids, several of which significantly changed with age. In addition, among the 3 *Mboat* genes, *Mboat2* was highly expressed in qNSCs/astrocytes and showed a significant age-related decrease in gene expression with age in qNSCs/astrocytes (**fig. S11**), and we have validated this decrease with age by *in situ* hybridization (**Fig. 4E**).

We chose AGPAT3 because it plays a crucial role in the synthesis of phospholipids, several of which significantly changed with age. In addition, *Agpat3* is the only isoform in the family that satisfies the combined criteria of i) relatively high expression level in qNSCs/astrocytes (though it did not change with age) (**fig. S11**) and ii) substrate specificity for PUFA-containing lipids.

We chose PLA2G4E because it has phospholipase activity, corresponding to several phospholipids that significantly changed with age in qNSCs. In addition, *Pla2g4e*, while not highly expressed in qNSCs/astrocytes (**fig. S11**), has an N-acyltransferase activity that produces N-acyl-ethanolamine phospholipids and those lipids have been shown to accumulate in brain aging (*40*).

We chose ELOVL5 because, together with FADS2, it works sequentially in PUFA biosynthesis pathway through stepwise elongation (ELOVL5) and desaturation (FADS2). Several PUFAs were remodeled with age in qNSCs/astrocytes (**Fig. 1E, 1H, 3B**). Moreover, ELOVL5 (together with FADS2) is involved in generating the most abundant PUFA species in the brain (e.g. 18:3, 20:3, 20:4, 20:5), based on studies on different regions of the brain (*41*). In addition, *Elovl5* had the highest expression level in qNSCs/astrocytes compared to other family members (*Elovl1, 2, 3, 4, 6, 7*) and showed decreased expression with age (**fig. S11**).

We chose FADS2 because, together with ELOVL5, it works sequentially in PUFA biosynthesis pathway through stepwise elongation (ELOVL5) and desaturation (FADS2). Several PUFAs were remodeled with age in qNSCs (**Fig. 1E, 1H, 3B**). Moreover, FADS2 (together with ELOVL5) is involved in generating the most abundant PUFA species in the brain (e.g. 18:3, 20:3, 20:4, 20:5), based on studies on different regions of the brain (*41*). FADS2 is also required for the synthesis of PUFA 22:6, another major PUFA species in the brain. In addition, *Fads2* exhibited a slight but significant decrease in gene expression in qNSCs/astrocytes with age (**fig. S11**).

Analysis of gene expression from single cell RNA-seq

Normalized gene counts from our previously published single cell RNA-seq data (*1*) was used to plot the expression level of the 5 genes of interest and genes encoding same family of enzymes (listed below).

Elovl1, *Elovl2*, *Elovl3*, *Elovl4*, *Elovl5*, *Elovl6*, *Elovl7*

Mboat1, *Mboat2*, *Lpcat3 (Mboat5)*, *Mboat7*

Fads1, *Fads2*

Agpat1, *Agpat2*, *Agpat3*, *Agpat4*, *Agpat5*

Pla2g4a, *Pla2g4b*, *Pla2g4c*, *Pla2g4d*, *Pla2g4e*, *Pla2g4f*

sgRNA cloning for *in vitro* gene knockouts of *Mboat2*, *Elovl5*, *Agpat3*, *Fads2*, *Pla2g4e*

LentiCRISPR v2 was a gift from Dr. Feng Zhang (Addgene plasmid # 52961; http://n2t.net/addgene:52961; RRID:Addgene_52961). psPAX2 was a gift from Didier Trono (Addgene plasmid # 12260; http://n2t.net/addgene:12260; RRID:Addgene_12260). pCMV-VSV-G was a gift from Dr. Robert Weinberg (Addgene plasmid # 8454; http://n2t.net/addgene:8454; RRID:Addgene_8454). sgRNAs targeting (*Mboat2*, *Elovl5*, *Agpat3*, *Fads2*, *Pla2g4e*) together with non-targeting and safe-targeting sgRNAs were selected from previously published genome-wide sgRNA library (*42*). For a list of sgRNAs used for *in vitro* gene knockouts, see **Table S8**. sgRNA oligos were ordered from Integrated DNA Technologies and subcloned into lentiCRISPR v2 plasmid using the *BsmB*I restriction site as described (*43*). Sanger sequencing was performed to verify the constructs. One sequencing primer verifying the insertion of sgRNA and the 5' end of the Cas9 sequence was used in conjunction with a second sequencing primer verifying the 3' end of the Cas9 sequence.

Lentiviral production and transduction for *in vitro* CRISPR/Cas9-mediated knockouts of *Mboat2*, *Elovl5*, *Agpat3*, *Fads2*, *Pla2g4e*

For lentiviral production, human embryonic kidney 293T (HEK 293T) cells (ATCC, CRL-3216) were seeded at a density of $13x10^6$ cells per 15cm plate in DMEM (Thermo Fisher, 11965092) with 10% fetal bovine serum (Gibco, 10099-141, lot 1751896) and penicillin-streptomycin-

glutamine 1X (Gibco, 10378-016). Two days after plating, HEK293T media was changed and the cells were transfected using 1mg/ml of polyethylenimine (PEI) (Polysciences, 23966-2).

LentiCRISPR v2 (45µg) was transfected together with the lentiviral packaging plasmids psPAX2 (28.35µg), and pCMV-VSV-G (8.325µg) per 15cm plate. One day (20-24 hours) after transfection, the media was changed to NeuroBasal-A with penicillin-streptomycin-glutamine. After another 20-24 hours, lentivirus-containing supernatant was collected and stored at 4°C and fresh media was added to the HEK293T cells for another collection after 24 hours. Both supernatants were then combined, filtered through a 0.45µm polyvinylidene fluoride (PVDF) filter (Millipore Sigma, SE1M003M00), and frozen at -80°C in 3ml aliquots.

For lentiviral transduction, 900,000 NSCs (passage 3 to passage 5) were plated in each well of a 6-well plate (~94,000 cells/cm2) maintained in "Quiescence NSC media" for 4 days (with media change every other day) before transduction. Next, 750µl of lentiCRISPR v2 supernatant was thawed on ice and mixed with 250µl of NeuroBasal-A + penicillin-streptomycin-glutamine with 8% of B27 minus vitamin A, bFGF (80ng/ml) and BMP4 (200ng/ml) and added to each well of a 6-well plate. qNSC cultures were incubated with viral media for 24 hours. The viral media was removed and a second lentiviral transduction was repeated for another 24 hours. Next, cells were washed once with NeuroBasal-A media and cells were kept in "Quiescence NSC media" for 7 days to allow CRISPR editing. Fresh "Quiescence NSC media" was replaced every 2 days. This 7-day period ensures a time window for both target gene editing and effect on the phenotype of interest (lipidomics, qNSC activation). To assess the efficiency of viral transduction and reproducibility, a positive control lentiviral construct pLJM1-EGFP (Addgene, 19319) was used in parallel. The fraction of transduced cells was quantified as $EGFP^+$ cells using an LSR-II flow

cytometer (BD Biosciences) 48 hours after transduction. The lentiviral construct we used did not include any tag or reporter that could be readily used as a readout for transduction. We therefore used the knockout score generated by Inference of CRISPR Edits (ICE) on harvested genomic DNA as a proxy to assess transduction efficiency (see "*CRISPR editing efficiency of individual knockouts in vitro of Mboat2, Elovl5, Agpat3, Fads2, Pla2g4e by Inference of CRISPR Edits (ICE) analysis*" below). We verified that the knockout of each enzyme gene was efficient in both young and old qNSCs, with a frameshift editing of 44-69% of the alleles for each gene in both young and old qNSCs (except *Agpat3*) (**fig. S12A**)."

CRISPR editing efficiency of individual knockouts *in vitro* of *Mboat2*, *Elovl5*, *Agpat3*, *Fads2*, *Pla2g4e* by Inference of CRISPR Edits (ICE) analysis

CRISPR editing efficiency of individual knockouts was assessed by analyzing genomic DNA. Briefly, genomic DNA was collected from qNSCs 7 days following lentiviral transduction. Genomic DNA was extracted after lysing qNSCs with 200µl of DirectPCR lysis reagent (Viagen biotech, 102-T) for 15min at room temperature. Lysates were then incubated with 0.2mg/ml Protease K (Invitrogen, 25530049) for 25min at 65°C, followed by protease deactivation for 15min at 95°C. We then amplified genomic DNA with primer pairs roughly 150-250bp upstream and 450-500bp downstream of sgRNA editing site, with 30s of annealing step at 55°C and 1min of extending step at 72°C for 40 cycles total. See **Table S10** for a complete list of primers.

We used the knockout score generated by Inference of CRISPR Edits (ICE) (Synthego Performance Analysis, ICE Analysis. 2019. v2.0. Synthego) to assess editing efficiency, according to the vendor's instruction. Knockout score was calculated by ICE based on the fraction of alleles from the genomic DNA of edited samples with either a frameshift or 21+ bp

indel, using an unedited sample as control. All knockouts had an editing efficiency between 55-70%, except the *Agpat3* knockout which had an efficiency at 27%.

Lipidomic dataset of CRISPR/Cas9-mediated knockouts *in vitro* of *Mboat2*, *Elovl5*, *Agpat3*, *Fads2*, *Pla2g4e* in young and old qNSCs

We generated a lipidomic LC-MS/MS dataset on n=4 primary qNSC cultures (each with $1x10^6$ qNSCs) from young and old mice, each with either control lentivirus or lentivirus expressing sgRNAs to the gene of interests (*Mboat2*, *Agpat3*, *Pla2g4e*, *Elovl5*, and *Fads2*). This dataset was the same as "*In vitro* #2" already described above (**Tables S1 and S9**).

Quantification of substrate and product level in *Mboat2*, *Elovl5*, *Agpat3*, *Fads2*, *Pla2g4e* knockouts *in vitro*

To evaluate the effectiveness of each gene knockout at the metabolite level, we quantified the lipid concentration of known substrates and products of each enzyme in cells with knockout for each gene with high efficiency knockouts (*Elovl5*, *Mboat2*, *Fads2*, *Pla2g4e* knockouts). Specifically,

Substrates:

ELOVL5: concentration of free fatty acid 18:2 and 18:3

MBOAT2: concentration of LPE(16:0)

FADS2: concentration of free fatty acid 18:2 and 20:2

PLA2G4E: summary concentration of all PC containing 16:0

Products:

ELOVL5: concentration of free fatty acid 20:2 and 20:3

MBOAT2: summary concentration of all PE containing 16:0

FADS2: concentration of free fatty acid 18:3 and 20:3

PLA2G4E: concentration of LPC(16:0)

Lipidomic similarity and differences between *Mboat2*, *Elovl5*, *Agpat3*, *Fads2*, *Pla2g4e* knockouts *in vitro*

To evaluate the similarity and differences in lipidomic profile as a result of knockouts, we first quantified effect size on all lipids between each knockout compared to control samples (**Table S9**). We separated lipids into "Lipids enriched in gene knockout (effect size > 0 when compared to control)" or "Lipids depleted in gene knockout (effect size < 0 when compared to control)" groups. We then took lipids from the top 20 percentile of each group and compared the overlap between different knockout conditions using an upset plot with R package "UpSetR" v1.4.0.

NSC activation assay *in vitro*

To determine the effect of different interventions (e.g. genetic perturbations, plasma membrane lipid supplementation) on qNSC function, we examined the ability of qNSCs to activate out of quiescence *in vitro*. We assessed qNSC activation efficiency by FACS to quantify the proportion of cells expressing proliferation marker Ki67, upon re-introduction of growth factors (*3*). qNSCs were washed twice with PBS (Corning, 21-040-CV) at 37°C before switching to "Proliferative

NSC media" for 4 days. Media was replaced every 2 days. Cells were dissociated with Accutase (Stemcell Technologies, 07920) for 5min, collected into conical tubes, and centrifuged at 300g for 5min. Next, $1x10^6$ cells were resuspended in 500µl FACS buffer (PBS with 2% fetal bovine serum (Gibco, 10099-141, lot 1751896)). Following this step, 500µl of 3.2% formaldehyde, diluted from 16% formaldehyde (Thermo Scientific, 28906), was added to the suspension dropwise under agitation to achieve a final concentration of 1.6% formaldehyde. Cells were fixed in 1.6% formaldehyde for 10min at room temperature before spinning down at 700g for 5min. Cells were washed once with FACS buffer before permeabilizing with 1ml of ice-cold 100% methanol (Thermo Fisher Scientific, A4121). Following a period of 20min incubation on ice, cells were then washed again and resuspended in 200µl of FACS buffer for staining. Ki67-APC (eBioscience, 17-5698-82, RRID:AB_2688057) antibody was used at 1:300 dilution. Samples were incubated in the dark for 30min at room temperature with gentle agitation. Cells were washed again before adding DAPI (Thermo Scientific, 62248) at a final concentration of 0.2µg/ml in FACS buffer. Each sample was filtered with FACS-strainer cap tubes (Falcon, 352235), just prior to FACS analysis. Cells were analyzed on a BD LSR II flow cytometer, and Flowjo (v10) software was used for data analysis.

For samples with *Mboat2* overexpression, an anti-FLAG antibody was also used to identify cells with overexpression construct. 3X-FLAG antibody (Cell Signaling Technology, 87537S, lot 1, RRID not available) was used at 1:200 dilution. Cells were washed again, followed by incubation with a secondary antibody of donkey anti-rabbit 568 (Invitrogen, A-10042, lot 2306809, RRID:AB_2534017) used at 1:250 dilution.

Generation of an *Mboat2* overexpression construct

To overexpress *Mboat2* in qNSCs, we generated an overexpression construct containing the full-length coding sequence of mouse *Mboat2* transcript variant 1(NM_026037.3) tagged with a 3X FLAG tag (DYKDDDDK) and 3X GGGGS linker at the N-terminus of the MBOAT2. The overexpression construct was driven by a human *EF1α* promoter in a lentiviral vector (pLV). The lentiviral vector used to overexpress *Mboat2* in our study, pLV[Exp]-EF1A>3xFLAG/3xGGGGS/mMboat2[NM_026037.3], was synthesized by VectorBuilder. The vector ID is VB230119-1418wdg, which can be used to retrieve detailed information about the vector on vectorbuilder.com. See **Table S11** for the complete sequence of the construct. A control construct with the same lentiviral backbone expressing enhanced green fluorescent protein (EGFP) under the same *EF1α* promoter was used.

Lentiviral production and transduction for *Mboat2* overexpression *in vitro*

To generate lentiviruses overexpressing *Mboat2*, we transfected 45µg of *Mboat2* overexpression (*Mboat2* OE) construct or the EGFP control construct, together with the lentiviral packaging plasmids psPAX2 (Addgene plasmid # 12260) (28.35µg), and pCMV-VSV-G (Addgene plasmid # 8454) (8.325µg) in HEK293T cells in 15cm plate, using the same method as described in *"Lentiviral production and transduction for in vitro CRISPR/Cas9-mediated knockouts of Mboat2, Elovl5, Agpat3, Fads2, Pla2g4e"*.

For lentiviral transduction, qNSCs (900,000 seeded in each well of 6-well plates, ~94,000 cells/cm^2) were maintained in "Quiescence NSC media" for 4 days (with media change every 2 days) before transduction. For transduction, 750µl of *Mboat2* OE or EGFP control supernatant was thawed on ice and mixed with 250µl of NeuroBasal-A + penicillin-streptomycin-glutamine with 8% of B27 minus vitamin A, bFGF (80ng/ml) and BMP4 (200ng/ml) ("Viral media").

qNSC cultures were incubated with viral media for 24 hours. Cells were then washed once with NeuroBasal-A media and then kept in "Quiescence NSC media" for 3 additional days before being harvested for lipidomic analysis or used for NSC activation assay (see "*NSC activation assay in vitro*"). We used the GFP reporter and the FLAG-tag to assess transduction of the control (GFP) and *Mboat2* overexpression (FLAG) lentivirus, respectively. We verified that the transduction efficiency by the *Mboat2* overexpression lentivirus was similar in both young and old qNSCs (53-55%) (**fig. S12H**).We validated that this experimental timeline (4 days in quiescence, one-time viral transduction, and 3-day incubation in quiescent media for a total of 8 days in quiescence) led to a 5-fold increase in *Mboat2* mRNA level in cells transduced with *Mboat2* overexpression virus (**fig. S12G**).

Design of "*Mboat2* overexpression" lipidomic experiments

To assess the effects of *Mboat2* overexpression on the lipidome of qNSCs, we generated a lipidomic LC-MS/MS dataset on n=4 primary qNSC cultures ($1x10^6$ qNSCs) from young and old mice, each with either control lentivirus or lentivirus overexpressing *Mboat2* as described above in "*Mboat2* overexpression". This experiment and analysis was done as outlined for our "*In vitro* #1" lipidomic experiment, with the only difference being the use of new column with the same catalog number.

Lentiviral production for *in vivo Mboat2* overexpression

For producing lentivirus used in *in vivo Mboat2* overexpression experiments, 45µg of *Mboat2* overexpression (*Mboat2* OE) or EGFP control plasmid was transfected together with the lentiviral packaging plasmids psPAX2 (28.35µg), and pCMV-VSV-G (8.325µg), identical to *Mboat2* overexpression experiments *in vitro*. All transfections were done in human embryonic

kidney HEK293T cells (ATCC, CRL-3216) plated in 15cm plates. We plated four 15cm plates of 293T cells ($13x10^6$ cells per 15cm plate) for a total of 200 ml of collected virus after 3 days of collecting at 4 °C, followed by ultracentrifugation to concentrate the virus. For ultracentrifugation, we sterilized 30ml ultraclear tubes (Beckman Coulter 344058) under UV (TC room biosafety cabinet) for 15min. We placed these tubes on ice, allowing them to cool for 15min. We then added 30ml of virus and centrifuged at 16,500 r.p.m. for 1 hour at 4 °C. We carefully decanted the supernatant using serological pipettes, leaving 1ml medium in the bottom of the tube, adding 30ml more virus-containing medium and centrifuging again. We repeated the decanting, refilling and centrifugation of the same tube, concentrating a total of 180ml of virus supernatant into a single tube. After the last ultracentrifugation, we removed most of the supernatant with a serological pipette, and the last 1 ml with a P1000 pipet tip from the side of the tilted tube, so as not to disturb the viral pellet. The viral pellet was usually visible in center of all of the tubes. We resuspend in 60µl ice-cold PBS (1/3,000th original volume) by pipetting up and down about 60 times, being careful not to produce air bubbles. The concentrated resuspended virus was then aliquoted into PCR strip tubes in 5µl aliquots and placed onto dry ice. After 15 min, the concentrated virus preparation was transferred to −80 °C for storage. For each experiment, the concentrated virus preparation was thawed on ice and injected into the brain within 30min of thawing. We assessed virus infectivity of each batch by performing serial dilution (3µl, 1µl, 0.5µl) infections of $2x10^5$ HEK293T cells in 24-well culture plates for 16 hours of infection and then performing FACS analysis 48 hours later to detect the percentage of cells expressing FLAG tag and EGFP. For each experiment, we normalized virus infectivity (viral titer) across treatments by adjusting the concentrations of virus added in PBS.

Surgeries for genetic perturbations *in vivo*

To perform genetic overexpression *in vivo*, stereotaxic surgeries were performed to inject lentivirus into the lateral ventricle of mice. Male C57BL/6JN mice were used for *in vivo Mboat2* overexpression experiment, and assigned to receive either EGFP control or *Mboat2* overexpression lentiviral particles in a randomized manner. Surgeries were performed on heating pads with isoflurane-induced anesthesia, with a Kopf (Model 940) stereotaxic frame, World Precision Instruments (UMP3T-1) UltraMicroPump3, Hamilton 1710RN 100µl syringe with 30g Small Hub RN needle with a point 2 beveled end. Injections were made at the following coordinates, relative to bregma: lateral 0.8mm, anterior 0.3mm and ventral depth 2.5mm from the skull surface. After drilling the skull and inserting the needle into position, we waited 5min before injecting the virus. We injected 3µl of equal titer virus at a rate of 10nl/s. We waited 7min after injection before removing the needle and suturing the skin. Animals were administered a single dose of buprenorphine SR (0.5mg/kg) for postoperative pain management and monitored for 1 week after surgery until full recovery. For these experiments, n=3-5 young or old animals were injected with either *Mboat2* overexpression virus or control virus. Brains were harvested 10 days after surgery.

Brain section preparation for *in vivo* immunofluorescent staining and RNA *in situ* hybridization

Young and old anaesthetized mice were first subjected to intracardiac perfusion with 4ml of heparin (Sigma Aldrich, H3149-50KU) and then 25ml of 4% paraformaldehyde (PFA) (Electron Microscopy Science, 15714) in PBS. Brain tissue was dissected, and post-fixed overnight in 4% PFA at 4°C. Brains were then washed three times for 10min each in 1x PBS at 4°C, followed by dehydration in 30% sucrose (Sigma-Aldrich, S3929-1KG) in PBS for 2-3 days at 4°C or until

brains sink to the bottom of the tube. Prior to embedding, all remaining liquid from brain tissue was removed with a Kimwipe. Samples were then embedded in O.C.T. compound (Fisher Scientific #23-730-571), flash frozen in a dry ice and ethanol bath, and were stored at -80°C until sectioning. Brains were sectioned at 16µm thickness using a LEICA cryostat (CM3050S). Sections were immobilized on Superfrost plus slides (Fisher Scientific, #12-550-15) in sets of five slides with four sections each alternating slides such that neighboring sections on each slide were 80µm apart from each other in the sample tissue (e.g. slide 1 has the 1^{st}, 6^{th}, 11^{th}, and 16^{th} section of that set, slide 2 has the 2^{nd}, 7^{th}, 12^{th}, and 17^{th} section of that set, etc.) to capture a broader range of the SVZ within each slide. Slides were stored at -20°C until staining. Slides covering a range of roughly 320-640µm deep into the SVZ for each animal were selected for staining and imaging.

***In vivo* immunofluorescent staining on brain section**

Slides were warmed to room temperature and washed for 5min in 1x PBS and permeabilized in cold (-20°C) methanol with 0.1% Triton X-100 (Thermo Fisher Scientific, #BP151-500) for 15min. Slides were then washed 3 times in 1x PBS for 5min. Sections were then segmented from each other using a hydrophobic marker (Fisher Scientific, NC1490738). Sections were blocked in a solution of 5% normal donkey serum (ImmunoReagents, SP-072-VX10) and 1% bovine serum albumin (Sigma-Aldrich, A7888-100G) in 1X PBS for 30min at room temperature. Primary antibodies were diluted in blocking solution and used as follows: mCherry (Invitrogen, M11217, lot XJ359389, 1:500, RRID:AB_2536611), EGFR (Sigma-Aldrich, 06-847, lot 3173794, 1:200, RRID:AB_2096607), GFAP (Abcam, ab53554, lot 1091347-1,1:5000, RRID:AB_880202). We added 75µl primary antibody/blocking solution per section and incubated overnight at 4°C in a humidified chamber. Slides were washed 3 times for 10min each

in PBS with 0.2% Tween 20 (Sigma-Aldrich, # P1379-1L) followed by 1x PBS washes for 15min repeated twice. Secondary antibodies were diluted in blocking solution and used as follows: anti-Goat Alexa Fluor 647 (Invitrogen, A-21447, lot 2273668, 1:500, RRID:AB_141844), anti-Rat Alexa Fluor 594 (Invitrogen, A-21209, lot 2400917, 1:500, RRID:AB_2535795), and anti-Rabbit Alexa Fluor 488 (Invitrogen, A-21206, lot 2668665, 1:500, RRID:AB_2535792). Next, 75µl secondary antibody/blocking solution was added to each section and then incubated at room temperature for 2 hours. Slides were washed 3 times in PBS with 0.2% Tween 20 for 10min followed by 3 1X PBS washes for 5min. Slides were then mounted with ProLong Gold with DAPI (Invitrogen, # P36934) and allowed to dry overnight at room temperature. Slides were sealed with clear nail polish and allowed to dry and then transferred to 4 °C for storage before imaging.

Hybridization chain reaction (HCR) probe design

We performed hybridization chain reaction (HCR) to detect *Mboat2* transcript level *in situ* following the split-initiator probes design of HCR v3.0 (*44*). Specifically, 22 pairs (44 probes) of non-overlapping probe sets were tiled across the entire consensus region of all isoforms of mouse *Mboat2* gene. Each probe was 22-nucleotide long and carried half of the HCR initiator sequence (gTCCCTgCCTCTATATCTTT and TTCCACTCAACTTTAACCCg). See **Table S10** for the complete list of HCR probe sets.

HCR staining of brain sections

Slides were warmed to room temperature and washed for 5min in PBS. Samples were permeabilized in cold (-20°C) methanol with 0.1% Triton X-100 for 15min followed by a 5-min wash in PBS. Slides were then blot dried with a Kimwipe and 200µl hybridization buffer

(Molecular Instruments, HCR Probe Hybridization Buffer, lot BPH02223) was added directly to each slide to cover samples and incubated for 30min at 37°C in a humid chamber. After incubation, the hybridization buffer was removed. Pooled *Mboat2* targeting probes at 0.5pmol/µl were diluted in hybridization buffer to a final concentration of 0.01pmol/µl (1:50). Next, 100µl probe/hybridization buffer solution was added to each slide and covered with a glass coverslip to prevent drying. The samples were then incubated at 37°C in a humid chamber overnight. After overnight incubation, the coverslip and probe/hybridization buffer solution was removed followed by five 15min washes of 100% wash buffer (Molecular Instruments, HCR Probe Wash Buffer, lot BPW02323), 75% probe wash buffer/25% 5x SSCT (20X SSC (Invitrogen, AM9763) diluted to 5x with 0.1% Tween-20)), 50% probe wash buffer/50% 5x SSCT, 25% probe wash buffer/75% 5x SSCT, and 100% 5x SSCT in succession. After washes, slides were incubated in amplification buffer (Molecular Instruments, HCR Amplifier Buffer, lot BAM02223) for 30min at room temperature in a humid chamber. Alexa Fluor 546-labelled h1 and h2 hairpins (Molecular Instruments, B3-h1-546, lot S073826, and B3-h2-546, lot S073926) at 3µM were then snap-cooled by heating to 95°C for 90s in a thermal cycler and then allowed to cool to room temperature. Each hairpin was then diluted in amplification buffer to a final concentration of 60nM (1:50). Hairpin/amplification buffer solution was then added to the slides, covered with a glass coverslip, and incubated overnight at 37°C in a humidified chamber. After overnight incubation, hairpin/amplification buffer solution was removed, and slides were washed twice for 30min in 5x SSCT and washed again for 5min in 5x SSCT at room temperature. For subsequent immunofluorescent staining, sections were blocked in a solution of 5% normal donkey serum and 1% bovine serum albumin in PBS. Primary antibodies were diluted in blocking solution: EGFR (Sigma-Aldrich, 06-847, lot 3173794, 1:200, RRID:AB_2096607), GFAP (Abcam,

ab53554, lot 1091347-1, 1:5000, RRID:AB_880202). Next, 75µl primary antibody/blocking solution was added to each section and incubated overnight at 4°C in a humid chamber. Slides were washed for 3 times for 10min in PBS with 0.2% Tween 20 followed by 2 washes in PBS for 15 minutes each. Secondary antibodies were diluted in blocking solution: anti-Rabbit Alexa Fluor 647 (Invitrogen, A-31573, lot 2420695, 1:500, RRID:AB_2536183) and anti-Goat Alexa Fluor 488 (Invitrogen, A-11055, lot 2301114, 1:500, RRID:AB_2534102). Next, 75µl secondary antibody/blocking solution was added to each section and incubated at room temperature for 2 hours in a humidified chamber. Slides were washed 3 times in PBS with 0.2% Tween 20 for 10min each followed by 3 washes in PBS for 5 minutes. Slides were mounted with ProLong Gold with DAPI and allowed to dry overnight at room temperature. Slides were sealed with clear nail polish, allowed to dry, and transferred to 4°C for storage until imaging.

Imaging of *in vivo* immunofluorescent staining or HCR of brain section

To image *in vivo* immunofluorescent staining of brain sections, we used confocal microscopy. For each section, we captured two single-plane tile images, one from the SVZ of each hemisphere, using a Zeiss LSM980 Airyscan 2 with a 40X glycerin-immersion lens. Using the polygon tool in Zeiss image capture software, we traced the outside of the SVZ to set the capture area. We used anchor points to set focal depth based on the DAPI signal to capture the middle of section while accounting for possible unevenness across tissue section.

Image quantification of *in vivo* immunofluorescent staining and HCR on brain section

Raw images were analyzed using the open-source image analysis software QuPath. During analysis, sample IDs and image names were blinded using the “mask image names” feature. Using the polygon annotation tool, we annotated the SVZ to include the areas of highest DAPI

signal along the ventricle as well as an additional cell layer. This annotation was used as the ROI for further analysis. Cell segmentation was performed using the "Cell Detection" function with DAPI as the detection channel using the default settings except for the following settings: background radius = 10μm, minimum area = 15μm^2, maximum area = 100μm^2, threshold = 35. Nuclei were expanded by 2μm. For *in vivo Mboat2* overexpression samples, single measurement classifiers for GFAP and EGFR status were made by using the cell mean intensity for the respective channels and adjusting the threshold to detect positive cells as assessed by eye. Subsequently, single measurement classifiers for GFAP and EGFR were combined into a composite classifier to assign GFAP and EGFR status to the SVZ ROI. For HCR quantification, *Mboat2* transcript signals of each individual cells (presented as puncta in HCR images) were quantified using the "Subcellular Detection" function with the following settings, detection threshold = 1250, expected spot size = 0.35 μm^2, min spot size = 0.15μm^2, max spot size = 0.6μm^2 in all SVZ cells.

Mboat2* mRNA level in qNSC/astrocytes *in vivo

We identified qNSCs/astrocytes (GFAP$^+$ and EGFR$^-$) on coronal sections of young and old mouse brains based on the single measurement classifier of GFAP and EGFR (described above). We then quantified the mean *Mboat2* transcript signals (described above) in qNSCs/astrocytes of each imaging tile to assess the *Mboat2* mRNA level in qNSC/astrocytes of young and old mice *in vivo*.

Validation of *Mboat2* overexpression *in vivo* by HCR quantification

We use the *Mboat2* transcript signals (described above) from HCR to assess *Mboat2* overexpression *in vivo.* We use the number of identified puncta on HCR staining to determine a

threshold value in identifying *Mboat2*-expressing cells. By visualizing the distribution of *Mboat2* transcript number on a histogram, we observe a distinct peak in cells with 2 or more detected *Mboat2* puncta. We then quantified the percentage of cells in each imaging tile at or above the threshold transcript level of *Mboat2* to assess the effectiveness of *Mboat2* overexpression *in vivo*.

Image quantification on aNSC numbers following *Mboat2* overexpression *in vivo*

$GFAP^+$ and $EGFR^+$ (aNSCs) cells and $GFAP^+$ and $EGFR^-$ (qNSCs/astrocytes) cells were first identified using the GFAP and EGFR classifier described above ("*Image quantification of in vivo immunofluorescent staining and HCR on brain section*") in animals injected with *Mboat2* overexpression virus. Next, the percentage of aNSCs relative to the total number of NSCs/astrocytes (aNSCs + qNSCs/astrocytes) were quantified in control cells and *Mboat2*-overexpressing cells of each animal. Control and *Mboat2*-overexpressing cells were identified based on whether *Mboat2* transcript level was below, or above the threshold transcript level of *Mboat2*, respectively, see "*Validation of Mboat2 overexpression in vivo by HCR quantification*". Note that one young animal died during the experiment, prompting the addition of 2 young control animals; 2 additional old control animals were also included to balance group sizes across age groups. All additional animals were injected with a control lentivirus expressing EGFP (see "*Lentiviral production for in vivo Mboat2 overexpression*") and are indicated by a distinct shape in the figure.

Plasma membrane lipid supplementation in recipient qNSC cultures

For plasma membrane lipid supplementation of recipient qNSC cultures, GPMVs from young and old donor qNSCs ($13x10^6$ qNSCs seeded in a 15cm plate, 90,000 cells/cm^2) were generated

using the identical protocol described above. In addition to plasma membrane lipids, GPMVs also contain proteins. We therefore used the Folch method described above to isolate the lipid constituent of the GPMV before supplementing it into cell culture. Plasma membrane lipids extracted from GPMVs were resolubilized in 100µl of 100% methanol and stored in -20°C before use. Young and old recipient qNSCs were incubated in quiescent media for 4 days before being supplemented with GPMV lipids or control solvent (100% methanol), both diluted 1:250 into "Quiescence NSC media" for 48 hours. Quiescence media was then replaced and cells were incubated in "Quiescence NSC media" for another 24 hours before being harvested for the different assays.

Imaging of plasma membrane lipid uptake by qNSCs

To image plasma membrane lipid uptake by qNSCs, the lipophilic dye Vybrant™ DiI was introduced (at a dilution of 1:2000) to fluorescently label plasma membrane lipid extracts. Labelled lipid extracts were supplemented to qNSCs for 72 hours. Live-cell confocal imaging was done to capture cellular uptake of Vybrant™ DiI-labelled plasma membrane lipids, together with nuclear dye DAPI and lipophilipic dye Laurdan to visualize all membrane compartments of cells. Live cell imaging was carried out in 37°C imaging chamber with 5% CO_2 using a Zeiss LSM980 microscope. Images were taken using 60X objective with Airyscan 2 in Multiplex mode.

Design of lipid supplementation lipidomic experiment

To assess the effects of plasma membrane lipid supplementation on the lipidome, we generated a lipidomic LC-MS/MS dataset on n=4-8 primary qNSC cultures from young and old mice, each with either control solvent or plasma membrane lipid extract as described in "*Plasma membrane*

lipid supplementation in recipient qNSC cultures". The lipidomic experiment and analysis was done exactly as described above for our "*In vitro* #1" lipidomic dataset, with the only difference being the use of new column with the same catalog number.

Effect size ranking of lipids that change with young plasma membrane supplementation

To determine whether lipids that showed a higher abundance following plasma membrane lipid supplementation were enriched at the plasma membrane, we first calculated lipid effect size between recipient qNSCs supplemented with young plasma membrane lipids and controls. We distinguished lipids that were "Higher in qNSCs with plasma membrane lipid supplementation (effect size > 0 when compared to control qNSCs)" and "Lower in qNSCs with plasma membrane lipid supplementation (effect size < 0 when compared to control qNSCs)". We then quantified the effect size between lipid from GPMV (of "GPMV" lipidomics) and from whole cell extract (from control samples of "*In vitro* #1"). We then identified overlapping lipids from both effect size analyses and ranked lipids based on the effect size comparison between whole cell extract and GPMV lipids in young and old samples. Lipids of the "Higher with plasma membrane lipid supplementation" and "Lower with plasma membrane lipid supplementation" groups were color-coded on the plot.

Comparison between the effect of young plasma membrane lipid supplementation on recipient qNSCs and age-related changes in GPMV lipids

To evaluate the effect of young plasma membrane lipid supplementation on recipient qNSCs, we calculated the effect size for individual lipids between recipient qNSCs (young or old) that were supplemented with young plasma membrane lipids and control recipient qNSCs. We then

calculated effect size for individual lipids between GPMV samples from young and old qNSCs (see "*GPMV lipidomics*"). We identified overlapping lipids from both analyses and plotted the result in a scatter plot for either young and old recipient qNSCs. Based on quadrants of the scatter plot, lipids were separated into 4 groups – Higher in recipient qNSCs with young plasma lipid supplementation and higher in young GPMVs, Higher in recipient qNSCs with young plasma lipid supplementation and higher in old GPMVs, Lower in recipient qNSCs with young plasma lipid supplementation and higher in young GPMVs, Lower in recipient qNSCs with young plasma lipid supplementation and higher in old GPMVs. We then quantified the distribution of lipids in each of these categories as a percentage of the total number of lipids and presented them in a pie chart.

Correlation between plasma membrane order and qNSC activation following plasma membrane lipid supplementation

To examine if qNSC activation is correlated with plasma membrane order, we performed qNSC activation assay by FACS (see "*NSC activation assay in vitro*") and plasma membrane order quantification (see "*Laurdan staining and quantification of plasma membrane order in primary NSC cultures*") on the same set of samples following plasma membrane lipid supplementation. Percentage of cells with positive Ki67 staining and the normalized GP ratio was plotted for each sample. Correlation coefficient and *P* value was obtained from Pearson correlation analysis in R version 4.4.2.

Statistical analyses

While we did not perform power analyses, we did use previous experiments to inform the experimental design with respect to sample size. To calculate statistical significance for

experiments, all tests were two-sided Wilcoxon rank-sum tests unless otherwise indicated. We performed multiple hypothesis correction using FDR (Benjamini-Hochberg correction for multiple comparisons). For effect size, our statistical analysis is described in detail above and also includes multiple hypothesis correction using FDR (Benjamini-Hochberg correction for multiple comparisons). To test the effect of knockout in paired samples, we performed normality test to establish that data is normally distributed before using paired Welch's *t*-test before control and knockout samples. To test age difference within knockout condition, unpaired Welch's *t*-test was used. All tests were performed by R version 4.0.2. All results from individual experiments and all statistical analyses are included in **Table S14**.

References

1. B. W. Dulken *et al.*, Single-cell analysis reveals T cell infiltration in old neurogenic niches. *Nature* **571**, 205-210 (2019).
2. D. S. Leeman *et al.*, Lysosome activation clears aggregates and enhances quiescent neural stem cell activation during aging. *Science* **359**, 1277-1283 (2018).
3. T. J. Ruetz *et al.*, CRISPR-Cas9 screens reveal regulators of ageing in neural stem cells. *Nature* **634**, 1150-1159 (2024).
4. L. Xu *et al.*, Restoration of neuronal progenitors by partial reprogramming in the aged neurogenic niche. *Nat Aging* **4**, 546-567 (2024).
5. R. W. Yeo *et al.*, Chromatin accessibility dynamics of neurogenic niche cells reveal defects in neural stem cell adhesion and migration during aging. *Nat Aging* **3**, 866-893 (2023).
6. B. Martynoga *et al.*, Epigenomic enhancer annotation reveals a key role for NFIX in neural stem cell quiescence. *Genes Dev* **27**, 1769-1786 (2013).
7. J. Folch, M. Lees, G. H. Sloane Stanley, A simple method for the isolation and purification of total lipides from animal tissues. *J Biol Chem* **226**, 497-509 (1957).
8. D. Kopczynski *et al.*, The lipidomics reporting checklist a framework for transparency of lipidomic experiments and repurposing resource data. *J Lipid Res* **65**, 100621 (2024).
9. K. Contrepois *et al.*, Cross-Platform Comparison of Untargeted and Targeted Lipidomics Approaches on Aging Mouse Plasma. *Sci Rep* **8**, 17747 (2018).
10. H. Tsugawa *et al.*, A lipidome atlas in MS-DIAL 4. *Nat Biotechnol* **38**, 1159-1163 (2020).

11. T. Cajka *et al.*, Optimization of Mobile Phase Modifiers for Fast LC-MS-Based Untargeted Metabolomics and Lipidomics. *Int J Mol Sci* **24**, (2023).
12. G. Liebisch *et al.*, Shorthand notation for lipid structures derived from mass spectrometry. *J Lipid Res* **54**, 1523-1530 (2013).
13. J. Koch *et al.*, Unequivocal Mapping of Molecular Ether Lipid Species by LC-MS/MS in Plasmalogen-Deficient Mice. *Anal Chem* **92**, 11268-11276 (2020).
14. T. E. Sweeney, W. A. Haynes, F. Vallania, J. P. Ioannidis, P. Khatri, Methods to increase reproducibility in differential gene expression via meta-analysis. *Nucleic Acids Res* **45**, e1 (2017).
15. F. M. Feringa *et al.*, The Neurolipid Atlas: a lipidomics resource for neurodegenerative diseases *Nature Metabolism* **7**, 2142–2164 (2024).
16. H. Yu *et al.*, MassCube improves accuracy for metabolomics data processing from raw files to phenotype classifiers. *Nat Commun* **16**, 5487 (2025).
17. L. V. Hedges, Distribution Theory for Glass's Estimator of Effect size and Related Estimators. *Journal of Educational Statistics* **6**, 107-128 (1981).
18. L. V. Hedges, I. Olkin, *Statistical Methods for Meta-Analysis*. (Elsevier Science, 1985).
19. P. Codega *et al.*, Prospective identification and purification of quiescent adult neural stem cells from their in vivo niche. *Neuron* **82**, 545-559 (2014).
20. X. Yan *et al.*, Cell-Type-Specific Metabolic Profiling Achieved by Combining Desorption Electrospray Ionization Mass Spectrometry Imaging and Immunofluorescence Staining. *Anal Chem* **92**, 13281-13289 (2020).
21. N. Otsu, A Threshold Selection Method from Gray-Level Histograms. *IEEE Transactions on Systems, Man, and Cybernetics* **9**, 62-66 (1979).
22. S. S. Shen-Orr *et al.*, Cell type-specific gene expression differences in complex tissues. *Nat Methods* **7**, 287-289 (2010).
23. D. Fitzner *et al.*, Cell-Type- and Brain-Region-Resolved Mouse Brain Lipidome. *Cell Rep* **32**, 108132 (2020).
24. J. Bartel, J. Krumsiek, F. J. Theis, Statistical methods for the analysis of high-throughput metabolomics data. *Comput Struct Biotechnol J* **4**, e201301009 (2013).
25. Q. Shen *et al.*, Adult SVZ stem cells lie in a vascular niche: a quantitative analysis of niche cell-cell interactions. *Cell Stem Cell* **3**, 289-300 (2008).
26. M. Tavazoie *et al.*, A specialized vascular niche for adult neural stem cells. *Cell Stem Cell* **3**, 279-288 (2008).
27. Z. Mirzadeh, F. T. Merkle, M. Soriano-Navarro, J. M. Garcia-Verdugo, A. Alvarez-Buylla, Neural stem cells confer unique pinwheel architecture to the ventricular surface in neurogenic regions of the adult brain. *Cell Stem Cell* **3**, 265-278 (2008).
28. Z. Gerstle, R. Desai, S. L. Veatch, Giant Plasma Membrane Vesicles: An Experimental Tool for Probing the Effects of Drugs and Other Conditions on Membrane Domain Stability. *Methods Enzymol* **603**, 129-150 (2018).
29. T. Baumgart *et al.*, Large-scale fluid/fluid phase separation of proteins and lipids in giant plasma membrane vesicles. *Proc Natl Acad Sci U S A* **104**, 3165-3170 (2007).
30. S. Mazeres, E. Joly, A. Lopez, C. Tardin, Characterization of M-laurdan, a versatile probe to explore order in lipid membranes. *F1000Res* **3**, 172 (2014).
31. D. M. Owen, C. Rentero, A. Magenau, A. Abu-Siniyeh, K. Gaus, Quantitative imaging of membrane lipid order in cells and organisms. *Nat Protoc* **7**, 24-35 (2011).

32. S. A. Sanchez, M. A. Tricerri, E. Gratton, Laurdan generalized polarization fluctuations measures membrane packing micro-heterogeneity in vivo. *Proc Natl Acad Sci U S A* **109**, 7314-7319 (2012).
33. P. Carravilla *et al.*, Measuring plasma membrane fluidity using confocal microscopy. *Nat Protoc* **20**, 1976-2004 (2025).
34. K. Gaus, T. Zech, T. Harder, Visualizing membrane microdomains by Laurdan 2-photon microscopy. *Mol Membr Biol* **23**, 41-48 (2006).
35. D. M. Owen *et al.*, Fluorescence lifetime imaging provides enhanced contrast when imaging the phase-sensitive dye di-4-ANEPPDHQ in model membranes and live cells. *Biophys J* **90**, L80-82 (2006).
36. Y. Wu *et al.*, Molecular rheometry: direct determination of viscosity in Lo and Ld lipid phases via fluorescence lifetime imaging. *Phys Chem Chem Phys* **15**, 14986-14993 (2013).
37. J. M. Kwiatek *et al.*, Characterization of a new series of fluorescent probes for imaging membrane order. *PLoS One* **8**, e52960 (2013).
38. A. Margineanu *et al.*, Visualization of membrane rafts using a perylene monoimide derivative and fluorescence lifetime imaging. *Biophys J* **93**, 2877-2891 (2007).
39. M. T. Stockl, A. Herrmann, Detection of lipid domains in model and cell membranes by fluorescence lifetime imaging microscopy. *Biochim Biophys Acta* **1798**, 1444-1456 (2010).
40. B. Moesgaard, G. Petersen, J. W. Jaroszewski, H. S. Hansen, Age dependent accumulation of N-acyl-ethanolamine phospholipids in ischemic rat brain. A (31)P NMR and enzyme activity study. *J Lipid Res* **41**, 985-990 (2000).
41. J. Ding *et al.*, A metabolome atlas of the aging mouse brain. *Nat Commun* **12**, 6021 (2021).
42. D. W. Morgens *et al.*, Genome-scale measurement of off-target activity using Cas9 toxicity in high-throughput screens. *Nat Commun* **8**, 15178 (2017).
43. N. E. Sanjana, O. Shalem, F. Zhang, Improved vectors and genome-wide libraries for CRISPR screening. *Nat Methods* **11**, 783-784 (2014).
44. H. M. T. Choi *et al.*, Third-generation in situ hybridization chain reaction: multiplexed, quantitative, sensitive, versatile, robust. *Development* **145**, (2018).

Figure 1

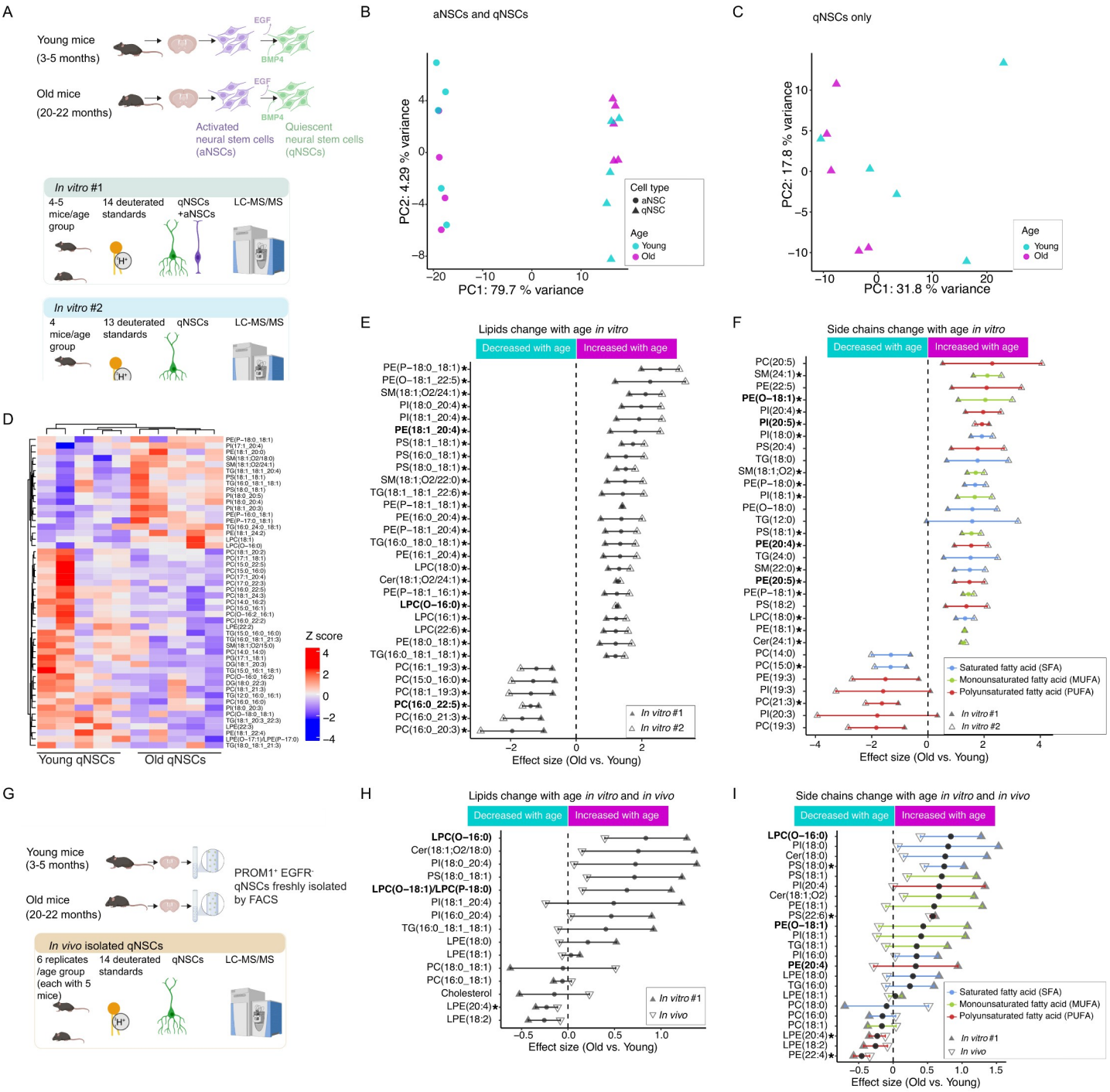
A
Young mice
(3-5 months)
Old mice
(20-22 months)
EGF
BMP4
Activated
neural stem cells
(aNSCs)
Quiescent
neural stem cells
(qNSCs)
In vitro #1
4-5
mice/age
group
14 deuterated
standards
qNSCs
+aNSCs
LC-MS/MS
In vitro #2
4
mice/age
group
13 deuterated
standards
qNSCs
LC-MS/MS
B
aNSCs and qNSCs
PC2: 4.29 % variance
PC1: 79.7 % variance
Cell type
aNSC
qNSC
Age
Young
Old
C
qNSCs only
PC2: 17.8 % variance
PC1: 31.8 % variance
Age
Young
Old
D
Z score
Young qNSCs
Old qNSCs
E
Lipids change with age in vitro
Decreased with age
Increased with age
PE(P−18:0_18:1)★
PE(O−18:1_22:5)★
SM(18:1;O2/24:1)★
PI(18:0_20:4)★
PI(18:1_20:4)★
PE(18:1_20:4)★
PS(18:1_18:1)★
PS(16:0_18:1)★
PS(18:0_18:1)★
SM(18:1;O2/22:0)★
TG(18:1_18:1_22:6)★
PE(P−18:1_18:1)★
PE(16:0_20:4)★
PE(P−18:1_20:4)★
TG(16:0_18:0_18:1)★
PE(16:1_20:4)★
LPC(18:0)★
Cer(18:1;O2/24:1)★
PE(P−18:1_16:1)★
LPC(O−16:0)★
LPC(16:1)★
LPC(22:6)★
PE(18:0_18:1)★
TG(16:0_18:1_18:1)★
PC(16:1_19:3)★
PC(15:0_16:0)★
PC(18:1_19:3)★
PC(16:0_22:5)★
PC(16:0_21:3)★
PC(16:0_20:3)★
In vitro #1
In vitro #2
Effect size (Old vs. Young)
F
Side chains change with age in vitro
Decreased with age
Increased with age
PC(20:5)
SM(24:1)★
PE(22:5)
PE(O−18:1)★
PI(20:4)★
PI(20:5)★
PI(18:0)★
PS(20:4)
TG(18:0)
SM(18:1;O2)★
PE(P−18:0)★
PI(18:1)★
PE(O−18:0)
TG(12:0)
PS(18:1)★
PE(20:4)★
TG(24:0)
SM(22:0)★
PE(20:5)★
PE(P−18:1)★
PS(18:2)
LPC(18:0)★
PE(18:1)★
Cer(24:1)★
PC(14:0)
PC(15:0)★
PE(19:3)
PI(19:3)
PC(21:3)★
PI(20:3)
PC(19:3)
Saturated fatty acid (SFA)
Monounsaturated fatty acid (MUFA)
Polyunsaturated fatty acid (PUFA)
In vitro #1
In vitro #2
Effect size (Old vs. Young)
G
Young mice
(3-5 months)
Old mice
(20-22 months)
PROM1+ EGFR-
qNSCs freshly isolated
by FACS
In vivo isolated qNSCs
6 replicates
/age group
(each with 5
mice)
14 deuterated
standards
qNSCs
LC-MS/MS
H
Lipids change with age in vitro and in vivo
Decreased with age
Increased with age
LPC(O−16:0)
Cer(18:1;O2/18:0)
PI(18:0_20:4)
PS(18:0_18:1)
LPC(O−18:1)/LPC(P-18:0)
PI(18:1_20:4)
PI(16:0_20:4)
TG(16:0_18:1_18:1)
LPE(18:0)
LPE(18:1)
PC(18:0_18:1)
PC(16:0_18:1)
Cholesterol
LPE(20:4)★
LPE(18:2)
In vitro #1
In vivo
Effect size (Old vs. Young)
I
Side chains change with age in vitro and in vivo
Decreased with age
Increased with age
LPC(O−16:0)
PI(18:0)
Cer(18:0)
PS(18:0)★
PS(18:1)
PI(20:4)
Cer(18:1;O2)
PE(18:1)
PS(22:6)★
PE(O−18:1)
PI(18:1)
TG(18:1)
PI(16:0)
PE(20:4)
LPE(18:0)
TG(16:0)
LPE(18:1)
PC(18:0)
PC(16:0)
PC(18:1)
LPE(20:4)★
LPE(18:2)
PE(22:4)★
Saturated fatty acid (SFA)
Monounsaturated fatty acid (MUFA)
Polyunsaturated fatty acid (PUFA)
In vitro #1
In vivo
Effect size (Old vs. Young)

Fig. 1. Lipidomics on young and old qNSCs *in vitro* and *in vivo* identifies changes in membrane lipid and side chain composition with age.
(A) Overview of 2 lipidomic studies *in vitro* (for *in vivo* design, see **G**). Primary NSC cultures were established from n=4-5 young (3-5 months) and n=4-5 old (20-22 months) C57BL/6JN male mice. Each culture was from an individual mouse. In each experiment, activated NSCs (aNSCs) were expanded. In parallel, quiescent NSCs (qNSCs) were generated by the addition of bone morphogenetic protein 4 (BMP4) and the removal of epidermal growth factor (EGF). For each experiment (*In vitro* #1 and *In vitro* #2), number of individual mice per age group used, number of internal deuterated lipidomic standards used, neural stem cell type (qNSCs, aNSCs) included are indicated. **(B to C)** Principal component analysis (PCA) on log2 transformed concentration of all lipids from *In vitro* #1 lipidomics (see **fig. S2A** for *In vitro* #2 and **fig. S1E** for overlapping lipids from *In vitro* #1 and *In vitro* #2). PCA was performed on aNSCs and qNSCs (**B**) or qNSCs only (**C**). Each symbol represents an individual primary aNSC culture (dot) or qNSC culture (triangle), established from individual young (cyan) or old (purple) mice. **(D)** Heatmap with clustering on the Z score of lipid concentration on 50 lipids with significant change with age (FDR-adjusted $P<0.1$) in qNSCs from *In vitro* #1 lipidomics (see **fig. S2B** for heatmaps of *In vitro* #2). **(E)** Lipids change with age in qNSCs of *In vitro* #1 and *In vitro* #2. Significant lipids that change with age by effect size in both *in vitro* studies are plotted. Only lipids that exhibit the top 30% overall effect size (either increase or decrease with age) are included (all significant lipids are in **fig. S1F**). Effect size for each lipid from *In vitro* #1 (filled triangle) and *In vitro* #2 (empty triangle) is shown together with mean effect size (black dot) and s.e.m. (error bar) from 2 studies. Significance is identified when FDR-adjusted $P<0.05$ (see Methods for details). Black asterisk indicates significance. Bold labels indicate lipids of interest that significantly change with age and with *Mboat2* interventions (see **Fig. 4**). **(F)** Side chain composition changes with age in qNSCs of *In vitro* #1 and *In vitro* #2. Only side chain features that exhibit the top 20% overall effect size (either increase or decrease with age) are included (all side chain features are in **fig. S4B**). Effect size for each lipid class/side chain from *In vitro* #1 (filled triangle) and *In vitro* #2 (empty triangle) is shown together with mean effect size (solid dot) in blue, green and red that represents saturated fatty acid (SFA), monounsaturated fatty acid (MUFA) and polyunsaturated fatty acid (PUFA), respectively. Error bar represents s.e.m. from 2 studies. Significance is identified when FDR-adjusted $P<0.05$ (see Methods for details). Black asterisk indicates significance. Abbreviations are: PI: phosphatidylinositol, LPC: lysophosphatidylcholine, TG: triacylglycerol, PS: phosphatidylserine, LPE: lysophosphatidylethanolamine, PG: phosphatidylglycerol, SM: sphingomyelin, PS: phosphatidylserine, PE: phosphatidylethanolamine, Cer: ceramide. Bold labels indicate side chain features of interest that significantly change with age and with *Mboat2* interventions (see **Fig. 4**). **(G)** Schematic of lipidomic profiling on qNSCs *in vivo*. Quiescent NSCs were freshly isolated from the brain of n=30 young (3-5 months) or n=30 old (20-22 months) C57BL/6JN male mice (n=6 qNSC samples, each from 5 pooled mice) using fluorescence-activated cell sorting (FACS) based on the positive staining of Prominin-1 ($PROM1^+$) and negative staining of epidermal growth factor receptor ($EGFR^-$). Number of animals used, number of internal deuterated lipidomic standards used, neural stem cell type included are indicated. **(H)** Lipids change with age in qNSCs *in vitro* and *in vivo*. Effect size of lipids from *In vitro* #1 (filled triangle) and *In vivo* isolated qNSCs (upside-down triangle) is plotted together with mean effect size (black dot) and s.e.m. (error bar) from 2 studies. Significance is identified when $P<0.05$ (see Methods for details). Black asterisk indicates significance. Bold labels indicate lipids of interest

that significantly change with age and with *Mboat2* interventions (see **Fig. 4**) *in vitro*. **(I)** Side chain composition changes with age in qNSCs *in vitro* and *in vivo*. Effect size of side chain composition features from *In vitro* #1 (filled triangle) and *In vivo* isolated qNSCs (upside-down triangle) is plotted together with mean effect size (solid dot) in blue, green, and red that represents saturated fatty acid (SFA), monounsaturated fatty acid (MUFA), and polyunsaturated fatty acid (PUFA), respectively. Error bar represents s.e.m. from 2 studies. Significance is identified when $P<0.05$ (see Methods for details). Black asterisk indicates significance. Bold labels indicate side chain features of interest that significantly change with age and with *Mboat2* interventions (see **Fig. 4**) *in vitro*. Abbreviations as in F. For statistical test of age-related effect sizes on lipids (**E and H**) and side chain compositions (**F and I**), statistical significance was assessed based on the *P*-value from test statistics using the 95% confidence interval of the data, and multiple hypothesis correction was done by FDR.

Figure 2

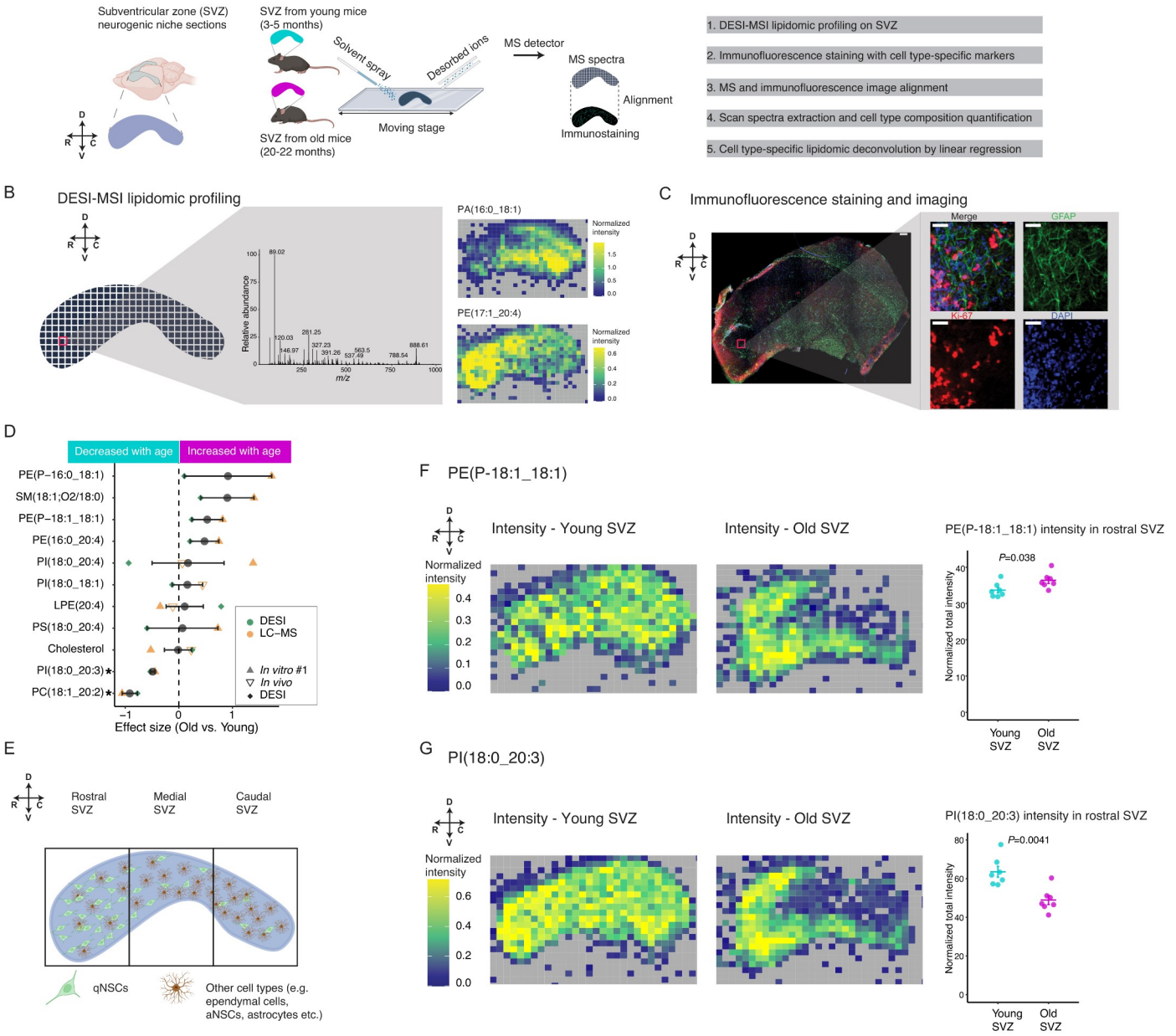
A
Subventricular zone (SVZ) neurogenic niche sections
SVZ from young mice (3-5 months)
SVZ from old mice (20-22 months)
Solvent spray
Desorbed ions
Moving stage
MS detector
MS spectra
Alignment
Immunostaining
1. DESI-MSI lipidomic profiling on SVZ
2. Immunofluorescence staining with cell type-specific markers
3. MS and immunofluorescence image alignment
4. Scan spectra extraction and cell type composition quantification
5. Cell type-specific lipidomic deconvolution by linear regression
B
DESI-MSI lipidomic profiling
Relative abundance
m/z
PA(16:0_18:1)
PE(17:1_20:4)
Normalized intensity
C
Immunofluorescence staining and imaging
Merge
GFAP
Ki-67
DAPI
D
Decreased with age
Increased with age
PE(P−16:0_18:1)
SM(18:1;O2/18:0)
PE(P−18:1_18:1)
PE(16:0_20:4)
PI(18:0_20:4)
PI(18:0_18:1)
LPE(20:4)
PS(18:0_20:4)
Cholesterol
PI(18:0_20:3)
PC(18:1_20:2)
DESI
LC–MS
In vitro #1
In vivo
DESI
Effect size (Old vs. Young)
E
Rostral SVZ
Medial SVZ
Caudal SVZ
qNSCs
Other cell types (e.g. ependymal cells, aNSCs, astrocytes etc.)
F
PE(P-18:1_18:1)
Intensity - Young SVZ
Intensity - Old SVZ
PE(P-18:1_18:1) intensity in rostral SVZ
P=0.038
Normalized total intensity
Young SVZ
Old SVZ
G
PI(18:0_20:3)
Intensity - Young SVZ
Intensity - Old SVZ
PI(18:0_20:3) intensity in rostral SVZ
P=0.0041
Normalized total intensity
Young SVZ
Old SVZ

Fig. 2. *In situ* lipidomic profiling on the subventricular zone neurogenic niche of young and old mice validates specific complex membrane lipids change with aging.
(A) Overview of lipidomic study *in situ* using desorption electrospray ionization mass spectrometry imaging (DESI-MSI). Subventricular zone (SVZ) neurogenic niche sections of whole mount preparation from n=7 young (3-5 months) and n=7 old (20-22 months) C57BL/6JN male mice were placed onto a moving stage. Solvent spray was introduced with a 200μm nozzle, and desorbed ions across the entire SVZ neurogenic niche were detected by mass spectrometry (MS) in an array. Arrows indicate orientation axes, with R: rostral, C: caudal, D: dorsal, and V: ventral. Sections are analyzed by DESI-MSI and then stained by immunofluorescence staining for cell type markers. The mass spectra and immunofluorescence images are then aligned, and deconvolution for cell type-specific lipidomic profile is done computationally using a linear regression method on each individual animal (see Methods for details). **(B)** Left panel: representative mass spectra from an individual DESI-MSI scan showing the abundance of metabolites (including lipids) with *m/z* between 50-1000. Each individual pixel represents a separate scan by DESI-MSI. Right panel: representative DESI-MSI image showing the tissue distribution of PA(16:0_18:1) (*m/z*: 673.5) (top) and PE(17:1_20:4) (*m/z*: 750.5) (bottom) across the SVZ neurogenic niche. Heatmap generated based on normalized lipid intensity. **(C)** Left panel: immunofluorescence staining of SVZ section from whole mount preparation, post-lipidomic profiling by DESI-MSI. Staining with GFAP (NSC and astrocyte marker, green), Ki67 (proliferation marker, red) and DAPI (nuclei, blue). Scale bar: 200μm. Right panel: enlarged immunofluorescence images covering the area of one individual DESI-MSI scan. Same set of markers as left panel. Scale bar: 50μm. **(D)** Age-associated change in lipids from qNSCs *in vitro* and *in vivo,* and from qNSCs/astrocytes *in situ*. Effect size of lipids from *In vitro* qNSCs (filled triangle), *In vivo* isolated qNSCs (upside-down triangle), and qNSCs/astrocytes from DESI-MSI (diamond) is plotted together with mean effect size (black dot) and s.e.m. (error bar) from 3 studies. Statistical significance was assessed based on the *P*-value from test statistics using the 95% confidence interval of the data, and multiple hypothesis correction was done by FDR. Significance is identified when FDR-adjusted $P < 0.05$ (see Methods for details). Black asterisk indicates significance. **(E)** Schematic diagram showing the spatial distribution of qNSCs (green) vs. other cell types (purple) across the SVZ neurogenic niche. SVZ is divided into 3 equally-size regions along the rostral – caudal axis for spatially-defined quantification of lipid abundance. The rostral region of the SVZ contains more NSCs than other regions. **(F to G)** Lipid abundance *in situ*. Left, middle: Heatmaps with normalized intensity of PE(P-18:1_18:1) (**F**) and PI(18:0_20:3) (**G**) in a representative young (left) and old (middle) SVZ is shown. Right: Quantification of the normalized lipid intensity in the rostral region of the SVZ (right) was done on PE(P-18:1_18:1) (**F**) and PI(18:0_20:3) (**G**). Dot and whisker plot with each individual dot representing the normalized intensity of specified lipids in the rostral region of SVZ from an individual animal. Whisker: +/- s.e.m.. *P*-values from Wilcoxon rank-sum test.

Figure 3

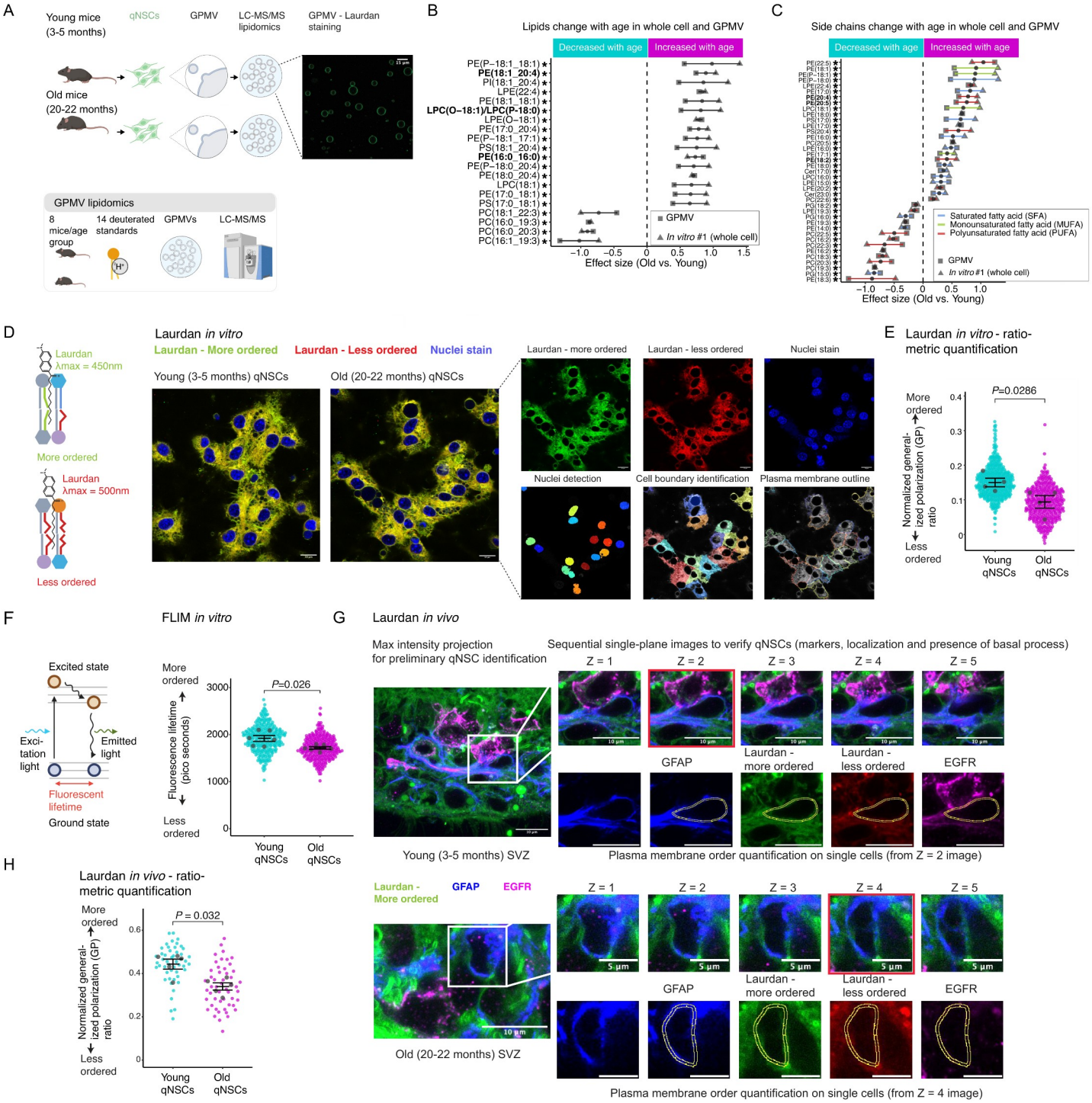
A
Young mice (3-5 months)
qNSCs
GPMV
LC-MS/MS lipidomics
GPMV - Laurdan staining
Old mice (20-22 months)
GPMV lipidomics
8 mice/age group
14 deuterated standards
GPMVs
LC-MS/MS
B
Lipids change with age in whole cell and GPMV
Decreased with age
Increased with age
PE(P-18:1_18:1)
PE(18:1_20:4)
PI(18:1_20:4)
LPE(22:4)
PE(18:1_18:1)
LPC(O-18:1)/LPC(P-18:0)
LPE(O-18:1)
PE(17:0_20:4)
PE(P-18:1_17:1)
PS(18:1_20:4)
PE(16:0_16:0)
PE(P-18:0_20:4)
PE(18:0_20:4)
LPC(18:1)
PE(17:0_18:1)
PS(17:0_18:1)
PC(18:1_22:3)
PC(16:0_19:3)
PC(16:0_20:3)
PC(16:1_19:3)
GPMV
In vitro #1 (whole cell)
Effect size (Old vs. Young)
C
Side chains change with age in whole cell and GPMV
Decreased with age
Increased with age
Saturated fatty acid (SFA)
Monounsaturated fatty acid (MUFA)
Polyunsaturated fatty acid (PUFA)
GPMV
In vitro #1 (whole cell)
Effect size (Old vs. Young)
D
Laurdan λmax = 450nm
More ordered
Laurdan λmax = 500nm
Less ordered
Laurdan in vitro
Laurdan - More ordered
Laurdan - Less ordered
Nuclei stain
Young (3-5 months) qNSCs
Old (20-22 months) qNSCs
Laurdan - more ordered
Laurdan - less ordered
Nuclei stain
Nuclei detection
Cell boundary identification
Plasma membrane outline
E
Laurdan in vitro - ratio-metric quantification
P=0.0286
More ordered
Normalized general-ized polarization (GP) ratio
Less ordered
Young qNSCs
Old qNSCs
F
FLIM in vitro
Excited state
Exci-tation light
Emitted light
Fluorescent lifetime
Ground state
More ordered
Fluorescence lifetime (pico seconds)
Less ordered
P=0.026
Young qNSCs
Old qNSCs
G
Laurdan in vivo
Max intensity projection for preliminary qNSC identification
Sequential single-plane images to verify qNSCs (markers, localization and presence of basal process)
Z = 1
Z = 2
Z = 3
Z = 4
Z = 5
GFAP
Laurdan - more ordered
Laurdan - less ordered
EGFR
Young (3-5 months) SVZ
Plasma membrane order quantification on single cells (from Z = 2 image)
Laurdan - More ordered
GFAP
EGFR
Old (20-22 months) SVZ
Plasma membrane order quantification on single cells (from Z = 4 image)
H
Laurdan in vivo - ratio-metric quantification
P = 0.032
More ordered
Normalized general-ized polarization (GP) ratio
Less ordered
Young qNSCs
Old qNSCs

Fig. 3. Plasma membrane lipids and plasma membrane order change with age in qNSCs. **(A)** Giant plasma membrane vesicles (GPMVs) were generated from quiescent neural stem cell (qNSC) primary cultures from n=8 young (3-5 months) and n=8 old (20-22 months) C57BL/6JN male mice. Lipids extracted from GPMVs were analyzed by lipidomics using LC-MS/MS. Confocal image showing isolated GPMVs visualized by staining with Laurdan (a dye that incorporates into membranes). Number of animals used, number of internal deuterated lipidomic standards used, and the lipidomic platform (LC-MS/MS) are indicated. **(B)** Lipids change with age in whole cells and GPMVs from qNSC primary cultures. Effect size of lipids from *In vitro* #1 (filled triangle) and GPMV from qNSCs (square) is plotted together with mean effect size (black dot) and s.e.m. (error bar) from both studies. Only significant lipids that exhibit the top 30% overall effect size (either increase or decrease with age) are included (all significant lipids are in **fig. S9D**). Significance is identified when FDR-adjusted P <0.05 (see Methods for details). Black asterisk indicates significance. Bold labels indicate lipids of interest that significantly change with age and with *Mboat2* interventions (see **Fig. 4**) *in vitro*. **(C)** Side chain composition changes with age in whole cells and GPMVs from qNSC primary cultures. Effect size of side chain composition features from *In vitro* #1 (filled triangle) and GPMV (square) is plotted together with mean effect size (solid dot) in blue, green, and red that represents saturated fatty acid (SFA), monounsaturated fatty acid (MUFA), and polyunsaturated fatty acid (PUFA), respectively. Error bar represents s.e.m. from 2 studies. Significance is identified when FDR-adjusted P<0.05 (see Methods for details). Black asterisk indicates significance. Bold labels indicate side chain features of interest that significantly change with age and with *Mboat2* interventions (see **Fig. 4**) *in vitro*. For statistical test of age-related effect sizes on lipids (**B**) and side chain compositions (**C**), statistical significance was assessed based on the P-value from test statistics using the 95% confidence interval of the data, and multiple hypothesis correction was done by FDR. **(D)** Plasma membrane order assessed *in vitro* by ratiometric quantification of Laurdan staining on primary qNSC cultures from n=4 young (3-5 months) and n=4 old (20-22 months) mice. Left: Schematics of the membrane order assessment by Laurdan. Lipophilic dye Laurdan is incorporated into the membrane and can shift its emission spectrum from ~450nm (in ordered lipid environment) to ~500nm (in less ordered lipid environment. Middle: Image from Laurdan rigid wavelength (more ordered, green) overlaid with Laurdan fluid wavelength (less ordered, red) and nuclei staining (blue) is shown from young qNSCs (left-middle) and old qNSCs (right-middle). Right: confocal images captured from individual wavelength (top) and steps of automated image analysis pipeline for plasma membrane order quantification (bottom). Scale bar represents 10μm. **(E)** Plasma membrane order quantified by generalized polarization ratio (GP ratio) from ratiometric quantification of Laurdan staining of young and old qNSCs. SuperPlots showing data from individual cells (cyan/purple dots), as well as the mean of each primary culture from individual mice (gray dots) +/- s.e.m.. Results from one independent experiment, n=4 primary cultures. P-value from Wilcoxon rank-sum test. Results from a second independent experiment are in **Table S14**. **(F)** Plasma membrane order examined *in vitro* by fluorescence lifetime imaging (FLIM) on primary qNSC cultures established from young (3-5 months) and old (20-22 months) mice. Left: Schematics of the membrane order assessment by FLIM. Fluorescent lifetime (the time a fluorophore spends in the excited state before emitting a photon and returning to the ground state) is used to quantify membrane order. Right: Quantification of plasma membrane order by FLIM. SuperPlots showing data from individual cells (cyan/purple dots), as well as the mean of each primary culture from individual mice (gray dots) +/- s.e.m.. Results from two independent experiments combined, n=6 primary cultures. P-

value from Wilcoxon rank-sum test. **(G)** Plasma membrane order assessed *in vivo* by ratiometric quantification of Laurdan staining of qNSCs in brain sections from n=5 young (3-5 months) and n=5 old (20-22 months) mice. Left: Max intensity projection from a Z stack of confocal images showing Laurdan rigid wavelength (more ordered, green) overlaid with GFAP (NSC and astrocyte marker, blue) and EGFR (proliferation marker, purple) staining. Right: Sequential single-plane images from the Z stack image enlarged to show the image analysis pipeline for plasma membrane order quantification on a single cell *in vivo* (top) and images from individual wavelength from a single-plane (Z=2) of the Z stack (bottom). qNSCs were identified as $GFAP^{+}EGFR^{-}$ cells that immediately adjacent to ependymal cells that line the lateral ventricles and show the presence of a basal process. Plasma membrane is outlined in yellow. Scale bar represents 10μm. A representative imaging sample from young SVZ and old SVZ is shown in the top and bottom panel of the figure, respective. **(H)** Plasma membrane order quantified by generalized polarization ratio (GP ratio) from ratiometric quantification of Laurdan staining of qNSCs from n=5 young (3-5 months) and n=5 old (20-22 months) male mice. SuperPlots showing data from individual cells (cyan/purple dots), as well as the mean of each mouse brain (gray dots) +/- s.e.m. Results from one independent experiment, n=5 mice. *P*-value from Wilcoxon rank-sum test. Results from a second independent experiment are in **Table S14**.

Figure 4

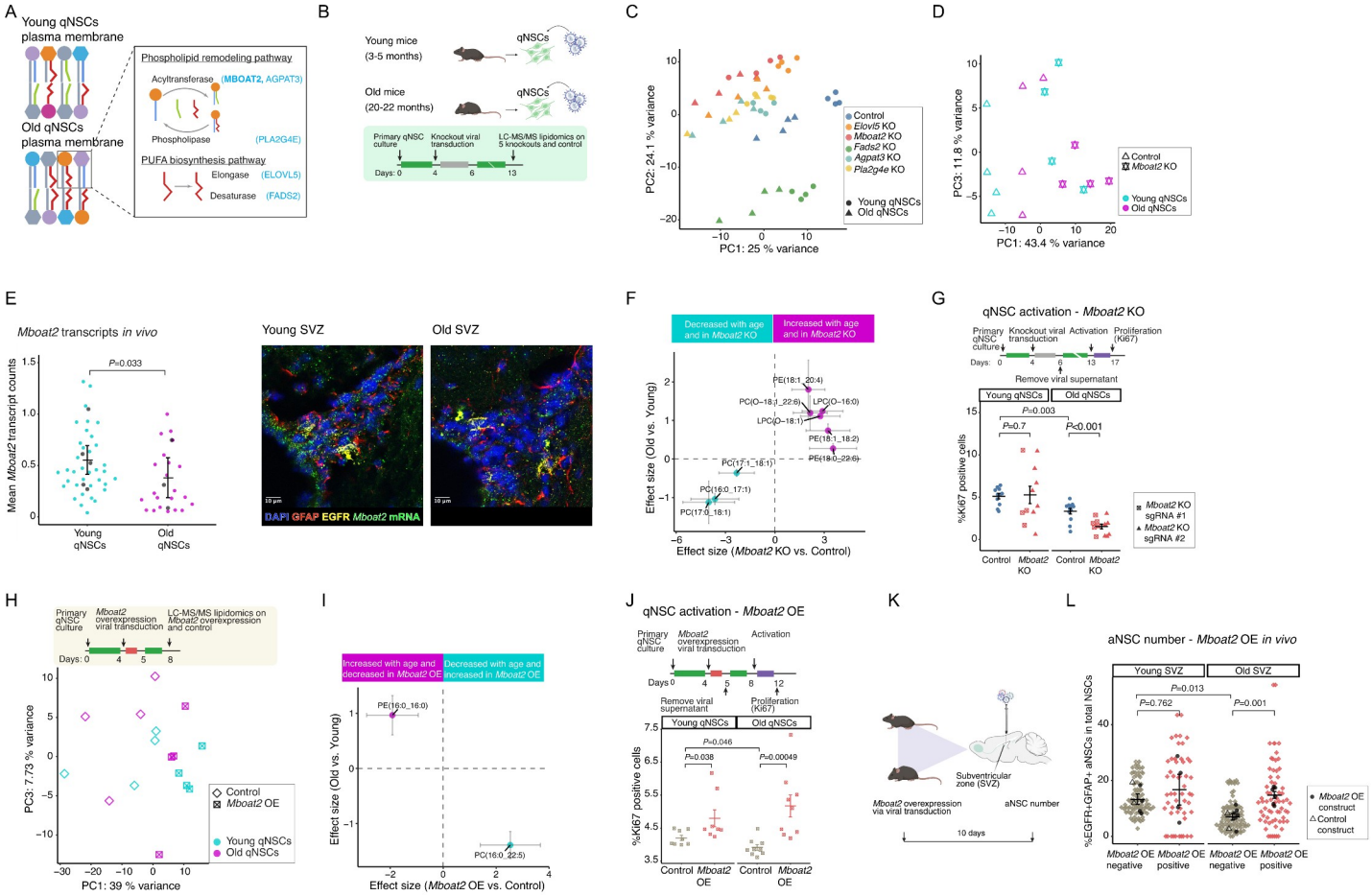
A
Young qNSCs plasma membrane
Old qNSCs plasma membrane
Phospholipid remodeling pathway
Acyltransferase (MBOAT2, AGPAT3)
Phospholipase (PLA2G4E)
PUFA biosynthesis pathway
Elongase (ELOVL5)
Desaturase (FADS2)
B
Young mice (3-5 months)
Old mice (20-22 months)
qNSCs
Primary qNSC culture
Knockout viral transduction
LC-MS/MS lipidomics on 5 knockouts and control
Days: 0 4 6 13
C
PC2: 24.1 % variance
PC1: 25 % variance
Control
Elovl5 KO
Mboat2 KO
Fads2 KO
Agpat3 KO
Pla2g4e KO
Young qNSCs
Old qNSCs
D
PC3: 11.8 % variance
PC1: 43.4 % variance
Control
Mboat2 KO
Young qNSCs
Old qNSCs
E
Mboat2 transcripts in vivo
Mean Mboat2 transcript counts
P=0.033
Young qNSCs
Old qNSCs
Young SVZ
Old SVZ
DAPI GFAP EGFR Mboat2 mRNA
F
Decreased with age and in Mboat2 KO
Increased with age and in Mboat2 KO
Effect size (Old vs. Young)
Effect size (Mboat2 KO vs. Control)
PE(18:1_20:4)
PC(O-18:1_22:6)
LPC(O-16:0)
LPC(O-18:1)
PE(18:1_18:2)
PE(18:0_22:6)
PC(17:1_18:1)
PC(16:0_17:1)
PC(17:0_18:1)
G
qNSC activation - Mboat2 KO
Primary qNSC culture
Knockout viral transduction
Activation
Proliferation (Ki67)
Days: 0 4 6 13 17
Remove viral supernatant
Young qNSCs
Old qNSCs
P=0.003
P=0.7
P<0.001
%Ki67 positive cells
Control
Mboat2 KO
Mboat2 KO sgRNA #1
Mboat2 KO sgRNA #2
H
Primary qNSC culture
Mboat2 overexpression viral transduction
LC-MS/MS lipidomics on Mboat2 overexpression and control
Days: 0 4 5 8
PC3: 7.73 % variance
PC1: 39 % variance
Control
Mboat2 OE
Young qNSCs
Old qNSCs
I
Increased with age and decreased in Mboat2 OE
Decreased with age and increased in Mboat2 OE
Effect size (Old vs. Young)
Effect size (Mboat2 OE vs. Control)
PE(16:0_16:0)
PC(16:0_22:5)
J
qNSC activation - Mboat2 OE
Primary qNSC culture
Mboat2 overexpression viral transduction
Activation
Days 0 4 5 8 12
Remove viral supernatant
Proliferation (Ki67)
Young qNSCs
Old qNSCs
P=0.046
P=0.038
P=0.00049
%Ki67 positive cells
Control
Mboat2 OE
K
Subventricular zone (SVZ)
Mboat2 overexpression via viral transduction
aNSC number
10 days
L
aNSC number - Mboat2 OE in vivo
Young SVZ
Old SVZ
P=0.013
P=0.762
P=0.001
%EGFR+GFAP+ aNSCs in total NSCs
Mboat2 OE negative
Mboat2 OE positive
Mboat2 OE construct
Control construct

Fig. 4. *Mboat2* acyltransferase regulates old qNSC activation *in vitro* and *in vivo*.
(A) Overview of the categories of enzymes involved in phospholipid remodeling pathway and poly-unsaturated fatty acid (PUFA) biosynthesis pathway. Proteins selected for corresponding genetic knockout (KO) are highlighted in blue (see Methods for more details). Protein selected for overexpression is in bold. **(B)** Knockout and overexpression experimental setup. For knockout experiment, primary NSC cultures from n=4 young (3-5 months) and n=4 old (20-22 months) mice were induced into quiescence for 4 days (qNSCs) and then transduced with lentiviruses for CRISPR/Cas9 knockout of individual target genes for 2 consecutive days. qNSCs were given a 7-day period to establish knockout before being harvested for lipidomic analysis with LC-MS/MS (same experiment as *In vitro* #2, **Fig. 1A**). **(C)** Principal component analysis (PCA) on log2-transformed concentration of all lipids. Each symbol represents an individual primary qNSC culture established from young (dot) or old (triangle) mice. Cultures were either transduced with a control lentivirus with a non-targeting sgRNAs (blue), or sgRNAs targeting *Elovl5* (orange), *Mboat2* (red), *Fads2* (green), *Agpat3* (turquoise) or *Pla2g4e* (yellow). **(D)** Principal component analysis (PCA) on log2-transformed concentration of all lipids from young (cyan) and old (purple) cultures that are transduced with lentivirus carrying control sgRNAs (triangle) or sgRNAs targeting *Mboat2* (double triangle). Each symbol represents an individual primary qNSC culture established from young or old mice. n=4 primary cultures (see **fig. S2A** for PCA of all KOs). **(E)** *Mboat2* mRNA level in qNSC/astrocytes *in vivo*. *In situ* hybridization of *Mboat2* mRNA was done on brain coronal sections from young (middle panel) and old (right panel) mice. Left: Quantification of *Mboat2* transcripts in qNSC/astrocytes. SuperPlots showing data from individual tiled images (colored dots), as well as the mean of each individual animal (gray dots) +/- s.e.m.. n=3-5 mice per age group. *P*-values from Wilcoxon rank-sum test on quantification of individual tiles. Right: Confocal images showing *Mboat2* transcripts (green) together with GFAP staining (red), EGFR staining (yellow) and DAPI. Scale bar represents 10μm. **(F)** Lipids change with *Mboat2* knockout in old qNSCs. Significant lipids that change with *Mboat2* knockout by effect size are plotted. X axis indicates the effect size of individual lipids (individual dots) between *Mboat2* KO vs. control in old qNSCs. Y axis indicates the effect size between young and old qNSCs (from **Fig. 1**). For each lipid, mean effect size is shown together with s.e.m. (error bar). Dashed lines indicated effect size of 0. **(G)** Activation (proliferation) ability of young and old qNSCs with *Mboat2* KO. Primary qNSC cultures from n=11-12 young (3-5 months) and n=11-12 old (20-22 months) mice were transduced with control lentivirus (sgRNAs targeting an unannotated region of the genome) or with sgRNAs targeting *Mboat2* (2 independent sgRNAs) for 2 consecutive days. After a 7-day recovery period, qNSCs were switched to proliferative NSC media for 4 days. The percentage of young and old control qNSCs (blue) and qNSCs with *Mboat2* KO (red) that successfully activated was assessed by intracellular FACS analysis for Ki67, a proliferation marker. Dot and whisker plot from 4 independent experiments, n=11-12 primary cultures. Horizontal bar: mean. Whisker: +/- s.e.m.. *P*-values from Wilcoxon rank-sum test. Squares: sgRNA #1, Triangles: sgRNA #2. **(H)** Principal component analysis (PCA) on log2-transformed concentration of all lipids from young (cyan) and old (purple) cells that are transduced with control lentivirus (diamond) or lentivirus overexpressing *Mboat2* (square with x). Each symbol represents an individual primary qNSC culture established from young or old mice. n=4 primary cultures. **(I)** Lipids change with *Mboat2* overexpression in old qNSCs. Significant lipids that change with *Mboat2* overexpression by effect size are plotted. X axis indicates the effect size of individual lipids (individual dots) between *Mboat2* OE vs. control in old qNSCs. Y axis indicates the effect size between young

and old qNSCs (from **Fig. 1**). For each lipid, mean effect size is shown together with s.e.m. (error bar). Dashed lines indicated effect size of 0. **(J)** Activation (proliferation) ability of young and old qNSCs with *Mboat2* overexpression. Primary qNSC cultures from n=8-9 young (3-5 months) and n=8-9 old (20-22 months) mice were transduced with control lentivirus (grey) or lentivirus overexpressing *Mboat2* (red). After a 3-day period to establish the effect of overexpression, qNSCs were switched to proliferative NSC media for 4 days. The percentage of young and old control qNSCs (grey) and qNSCs with *Mboat2* overexpression (red) that successfully activated was assessed by intracellular FACS analysis for Ki67, a proliferation marker. Dot and whisker plot from 2 independent experiments, n=8-9 primary cultures. Data from a third independent experiment (with lower overall activation) are also included in **Table S14.** Horizontal bar: mean. Whisker: +/- s.e.m.. Each dot represents a primary culture from an individual mouse. *P*-values from Wilcoxon rank-sum test. **(K)** Schematic of *Mboat2* overexpression experiment *in vivo*. For this experiment, n=4-5 young (3-4 months) and n=3-6 old (17-18 months) mice were transduced with control lentivirus or lentivirus overexpressing *Mboat2* via stereotaxic injection. NSC proliferation was assessed 10 days post-injection. **(L)** Activated NSC number in young and old mice with *Mboat2* overexpression *in vivo*. Percentage of aNSCs relative to the total number of NSC in *Mboat2* overexpression negative (grey) and *Mboat2* overexpression positive cells (red) of young and old mice was quantified. SuperPlots showing data from individual tiled images (colored dots), as well as the mean of each individual animal (gray dots) +/- s.e.m.. n=4-8 animals. In the *Mboat2* overexpression negative group, we included 2 additional young animals and 2 additional old animals that were injected with a control lentivirus that expresses an EGFP construct (empty triangle, see Methods for more details). *P*-values from Wilcoxon rank-sum test on quantification of individual animals.

Figure 5

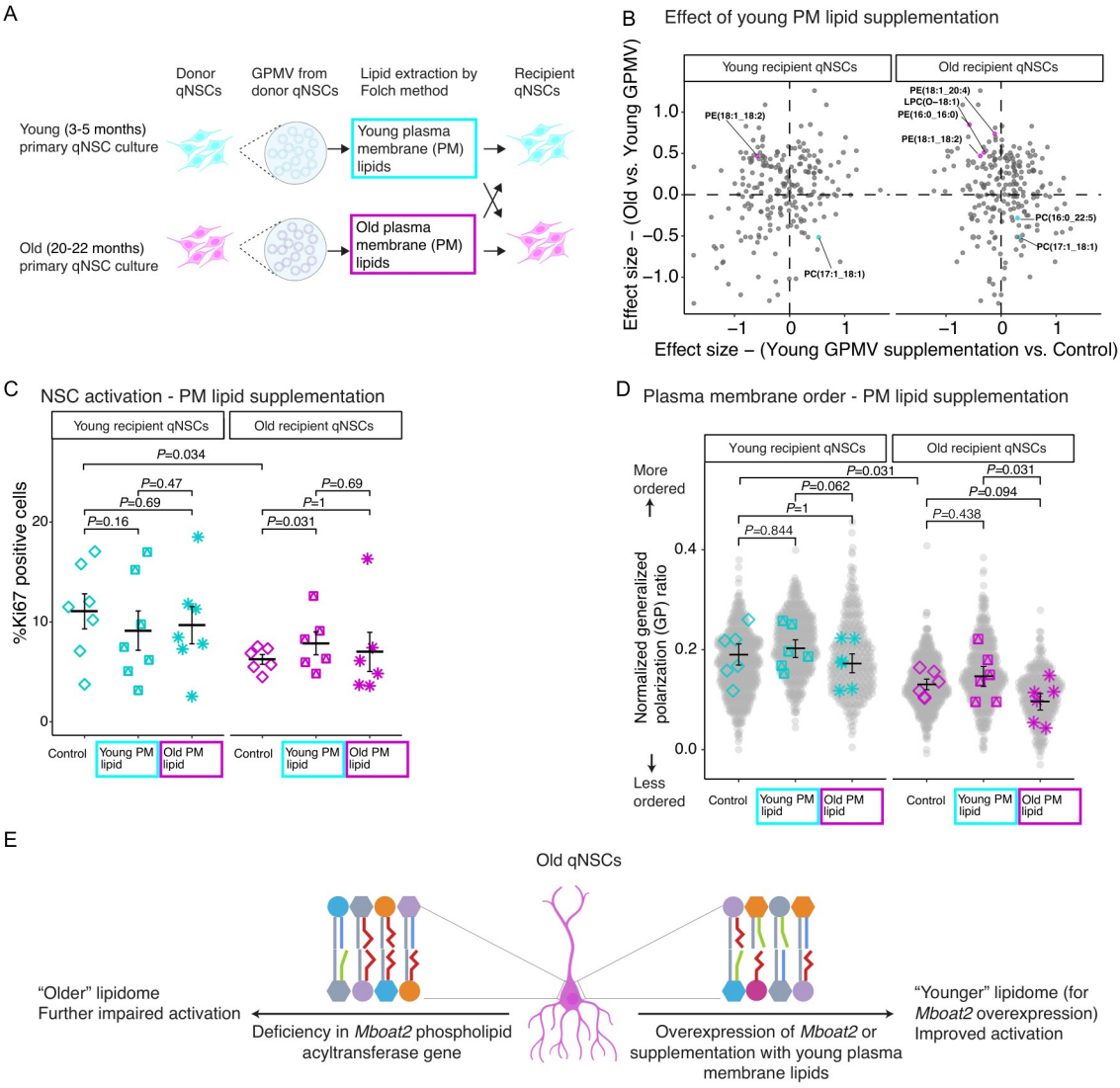
A
Donor qNSCs
GPMV from donor qNSCs
Lipid extraction by Folch method
Recipient qNSCs
Young (3-5 months) primary qNSC culture
Young plasma membrane (PM) lipids
Old (20-22 months) primary qNSC culture
Old plasma membrane (PM) lipids
B
Effect of young PM lipid supplementation
Young recipient qNSCs
Old recipient qNSCs
Effect size – (Old vs. Young GPMV)
Effect size – (Young GPMV supplementation vs. Control)
PE(18:1_18:2)
PC(17:1_18:1)
PE(18:1_20:4)
LPC(O-18:1)
PE(16:0_16:0)
PC(16:0_22:5)
C
NSC activation - PM lipid supplementation
%KI67 positive cells
P=0.034
P=0.47
P=0.69
P=0.16
P=0.69
P=1
P=0.031
Control
Young PM lipid
Old PM lipid
D
Plasma membrane order - PM lipid supplementation
More ordered
Less ordered
Normalized generalized polarization (GP) ratio
P=0.031
P=0.062
P=1
P=0.844
P=0.031
P=0.094
P=0.438
E
Old qNSCs
"Older" lipidome
Further impaired activation
Deficiency in Mboat2 phospholipid acyltransferase gene
Overexpression of Mboat2 or supplementation with young plasma membrane lipids
"Younger" lipidome (for Mboat2 overexpression)
Improved activation

Fig. 5. Supplementation with plasma membrane lipids from young cells boosts the activation ability of old qNSCs.
(A) Overview of the experimental scheme: GPMVs were generated from n=6-7 young (3-5 months) or n=6-7 old (20-22 months) qNSC primary cultures (donor cells). Plasma membrane lipids from respective donor cells were extracted using a modified Folch method (see Methods for details) and then supplemented to a different set of n=6-7 young (3-5 months) or n=6-7 old (20-22 months) qNSC cultures (recipient cells) for assessment of lipidomic changes (experiment with young plasma membrane lipid supplementation) or NSC activation and plasma membrane order (experiment with both young and old plasma membrane lipid supplementation). **(B)** Effect of plasma membrane lipid supplementation is visualized on a scatter plot for young (left) and old (right) recipient qNSCs. X axis indicates the effect size of individual lipids (individual dots) between cells supplemented with young plasma membrane lipids and control recipient cells. Y axis indicates the effect size of individual lipids (individual dots) between young and old GPMV lipids (from **Fig. 3**). Labeled lipids indicate lipids that significantly change with age (**Fig. 1**) and with *Mboat2* interventions (see **Fig. 4**). Annotated lipids are color-coded to indicate significant increase and decrease with age in purple and cyan, respectively. **(C)** Activation (proliferation) ability of qNSCs with plasma membrane lipid supplementation. Primary culture of qNSCs from n=6-7 young (3-5 months) and n=6-7 old (20-22 months) mice were incubated with either vehicle control (methanol) or plasma membrane lipids from young (3-5 months) or old (20-22 months) donor qNSCs for 3 days. qNSCs were then switched to proliferative NSC media for 4 days. The percentage of young and old qNSCs that successfully activated was assessed by intracellular FACS analysis for Ki67, a proliferation marker. Dot and whisker plot from 2 independent experiments, n=6-7 primary cultures. Horizontal bar: mean. Whisker: +/- s.e.m.. Each dot represents a primary culture from an individual mouse. *P*-values from Wilcoxon signed-rank test (because of paired control and lipid supplementation) and from Wilcoxon rank-sum test between young and old control recipient cells. **(D)** Plasma membrane order of young and old qNSCs upon plasma membrane lipid supplementation. Primary qNSC cultures from n=6 young (3-5 months) and n=6 old (20-22 months) mice were incubated with either vehicle control (methanol), plasma membrane lipids from young (3-5 months) or old (20-22 months) donor qNSCs for 3 days. Plasma membrane order was quantified by generalized polarization ratio (GP ratio) from Laurdan staining. SuperPlots showing data from individual cells (grey dots), as well as the mean of each primary culture (colored dots) +/- s.e.m.. Results from two independent experiments, n=6 primary cultures. *P*-values from Wilcoxon signed-rank test (because of paired control and lipid supplementation), and from Wilcoxon rank-sum test between young and old control recipient cells. **(E)** Model for the functional impact of membrane lipids in quiescent neural stem cell aging.

Figure S1

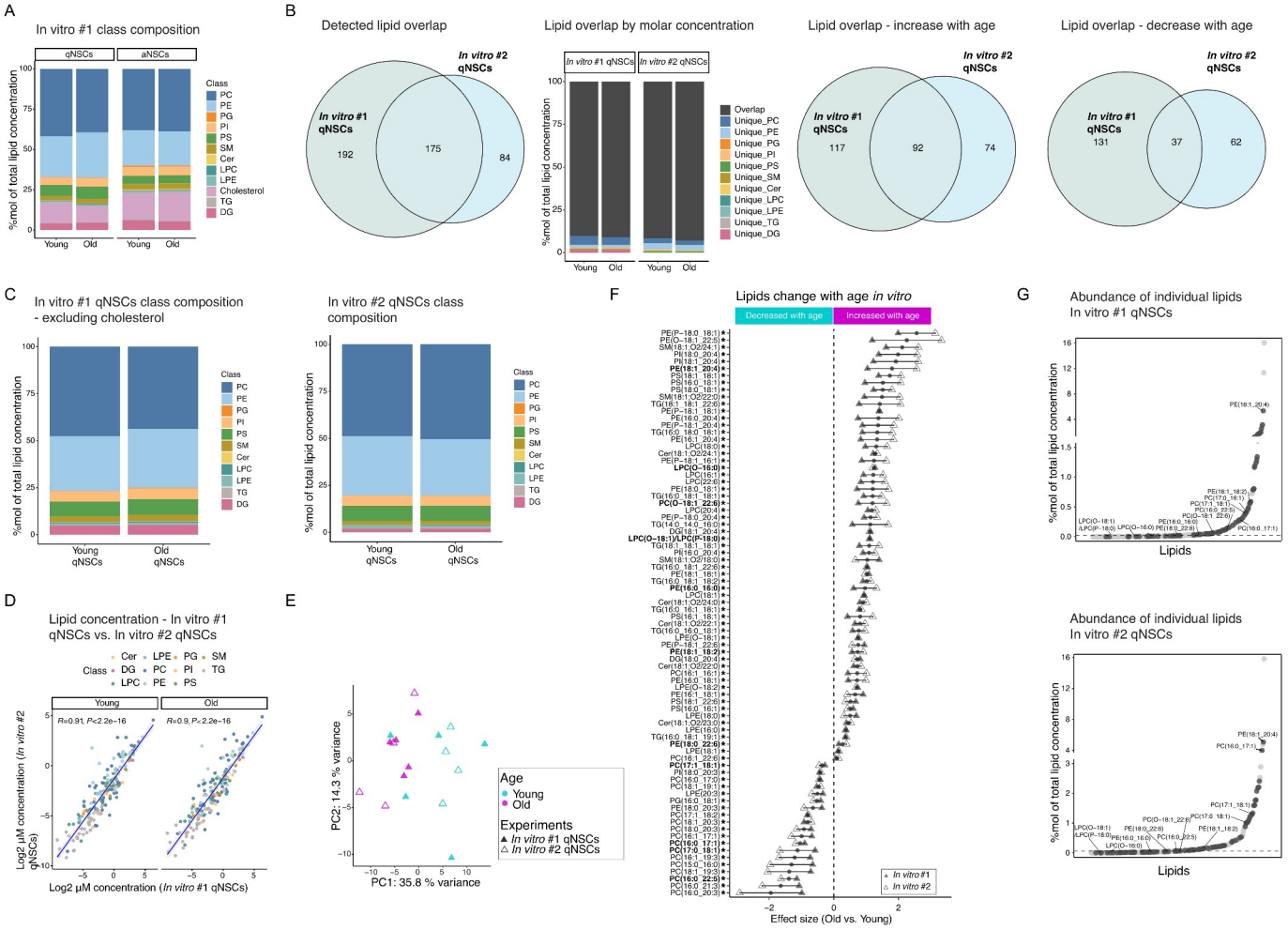
A
In vitro #1 class composition
qNSCs
aNSCs
%mol of total lipid concentration
Class
PC
PE
PG
PI
PS
SM
Cer
LPC
LPE
Cholesterol
TG
DG
Young
Old
B
Detected lipid overlap
In vitro #2 qNSCs
In vitro #1 qNSCs
192
175
84
Lipid overlap by molar concentration
Overlap
Unique_PC
Unique_PE
Unique_PG
Unique_PI
Unique_PS
Unique_SM
Unique_Cer
Unique_LPC
Unique_LPE
Unique_TG
Unique_DG
Lipid overlap - increase with age
117
92
74
Lipid overlap - decrease with age
131
37
62
C
In vitro #1 qNSCs class composition - excluding cholesterol
Young qNSCs
Old qNSCs
In vitro #2 qNSCs class composition
D
Lipid concentration - In vitro #1 qNSCs vs. In vitro #2 qNSCs
R=0.91, P<2.2e−16
R=0.9, P<2.2e−16
Log2 µM concentration (In vitro #2 qNSCs)
Log2 µM concentration (In vitro #1 qNSCs)
E
PC2: 14.3 % variance
PC1: 35.8 % variance
Age
Young
Old
Experiments
In vitro #1 qNSCs
In vitro #2 qNSCs
F
Lipids change with age in vitro
Decreased with age
Increased with age
Effect size (Old vs. Young)
G
Abundance of individual lipids In vitro #1 qNSCs
Abundance of individual lipids In vitro #2 qNSCs
Lipids

Fig. S1. Reproducibility of lipidomic changes at individual lipid level in primary neural stem cell cultures *in vitro* from independent lipidomic experiments.
(A) Concentration composition (%mol) of each lipid class on young and old qNSCs (left) and aNSCs (right) from *In vitro* #1 lipidomics. **(B)** Shared lipids from qNSCs of *In vitro* #1and *In vitro* #2. Venn diagram showing all overlapping lipids (left panel), lipids that increase with age (right-middle panel) and decrease with age (right panel) across 2 experiments. Lipid overlap by molar concentration is presented (left-middle panel) in a stacked bar plot, with individual block corresponding to the concentration composition (%mol) of commonly detected lipids across both datasets (dark grey block) and uniquely detected lipids from each dataset (colored blocks). **(C)** Concentration composition (%mol) of each lipid class on young and old qNSCs from *In vitro* #1 lipidomics excluding cholesterol (left) and *In vitro* #2 (right). **(D)** Correlation between lipid concentration (μM) in young (left panel) and old (right panel) qNSCs from *In vitro* #1 and *In vitro* #2. Pearson correlation was performed on concentration of individual lipids (solid dots colored by lipid classes) from each dataset. *R* and *P*-values from Pearson correlation are shown. Linear regression line (blue line) with 95% confidence interval (grey shade) is shown. **(E)** Principal component analysis (PCA) on log2 transformed lipid molar concentration of overlapping lipids from *In vitro* #1 (filled triangle) and *In vitro* #2 (empty triangle). PCA was performed on qNSCs only. Each symbol represents an individual primary qNSC culture established from individual young (cyan) or old (purple) mice. **(F)** Lipids change with age in qNSCs of *In vitro* #1 and *In vitro* #2. Significant lipids that change with age by effect size in both *in vitro* studies are plotted. Effect size for each lipid from *In vitro* #1 (filled triangle) and *In vitro* #2 (empty triangle) is shown together with mean effect size (black dot) and s.e.m. (error bar) from 2 studies. Statistical significance was assessed based on the *P*-value from test statistics using the 95% confidence interval of the data, and multiple hypothesis correction was done by FDR. Significance is identified when FDR-adjusted $P<0.05$ (see Methods for details). Black asterisk indicates significance. Bold labels indicate lipids of interest that significantly change with age and with *Mboat2* interventions (see **Fig. 4**). **(G)** Abundance of individual lipids across *in vitro* datasets. Dot plot of all detected lipids in *In vitro* #1 and *In vitro* #2 is ordered in %mol of total lipid concentration. Each dot represents an individual lipid species (light grey). Significant lipids with age from both studies (as listed in **Fig. 1E**) are highlighted in dark grey. Labeled lipids indicate lipids that significantly change with age (**Fig. 1**) and with *Mboat2* interventions (see **Fig. 4**). Dashed line indicates median lipid abundance of each dataset.

Figure S2

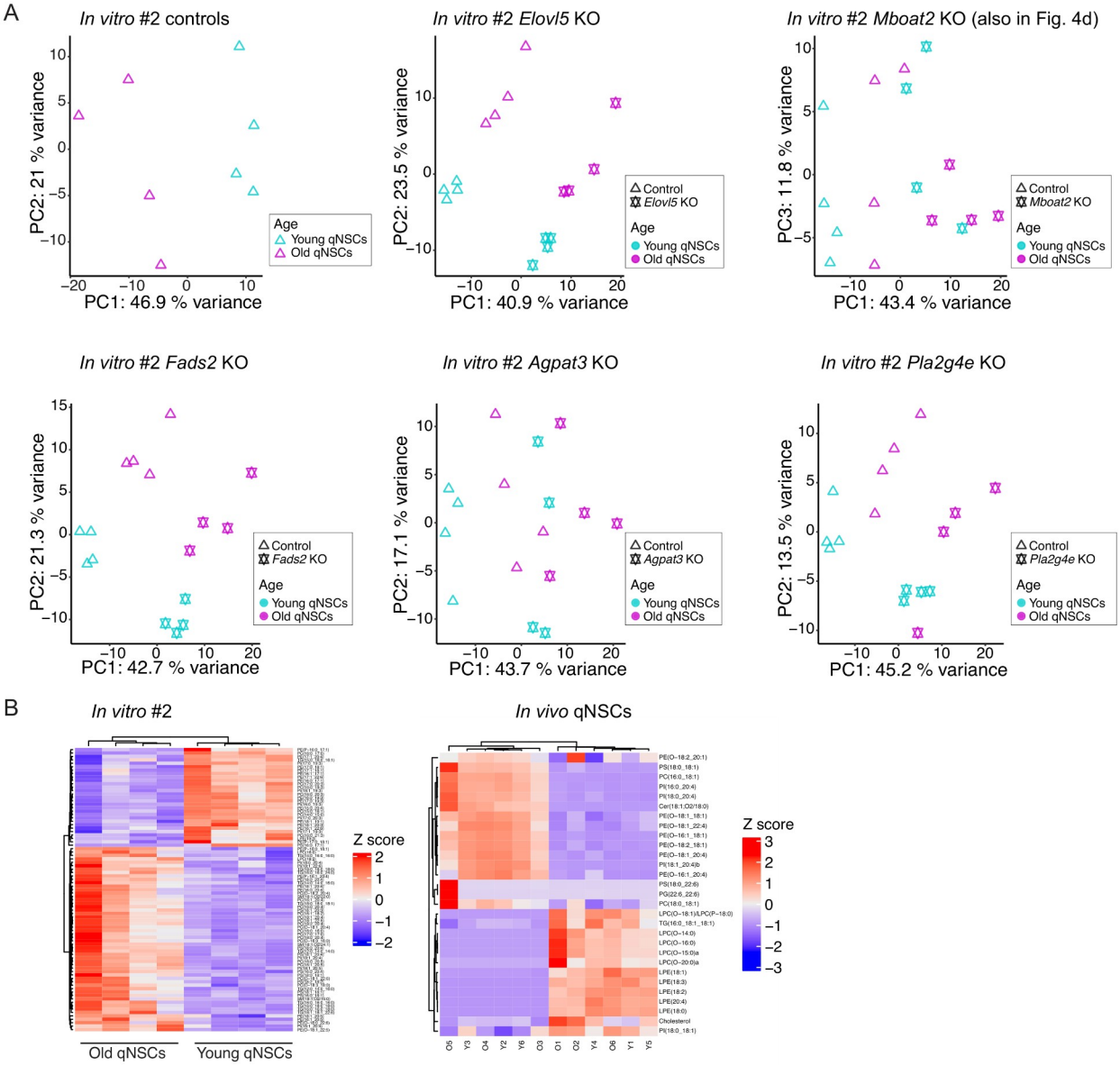
A
In vitro #2 controls
In vitro #2 Elovl5 KO
In vitro #2 Mboat2 KO (also in Fig. 4d)
In vitro #2 Fads2 KO
In vitro #2 Agpat3 KO
In vitro #2 Pla2g4e KO
PC1: 46.9 % variance
PC2: 21 % variance
PC1: 40.9 % variance
PC2: 23.5 % variance
PC1: 43.4 % variance
PC3: 11.8 % variance
PC1: 42.7 % variance
PC2: 21.3 % variance
PC1: 43.7 % variance
PC2: 17.1 % variance
PC1: 45.2 % variance
PC2: 13.5 % variance
Control
Elovl5 KO
Mboat2 KO
Fads2 KO
Agpat3 KO
Pla2g4e KO
Age
Young qNSCs
Old qNSCs
B
In vitro #2
In vivo qNSCs
Z score
Old qNSCs
Young qNSCs

Fig. S2. Principal component analysis and heatmaps on lipids with significant change with age *in vitro* and all lipids from *in vivo* lipidomics experiments.
(A) Principal component analysis (PCA) on log2 transformed lipid concentration (*In vitro* #2). PCA on *Mboat2* KO from *In vitro* #2 is also shown in **Fig. 4D**. **(B)** Left: Heatmap with clustering on the Z score of lipids with significant change (FDR-adjusted $P<0.1$) with age in qNSCs of *In vitro* #2. Right: Heatmap with clustering on the Z score of all identified lipids from *in vivo* isolated qNSC lipidomics.

Figure S3

Odd chain lipids with the top 30% largest effect size in Fig. 1E and fig. S1F

PC(15:0_16:0) positive mode

In vitro #1

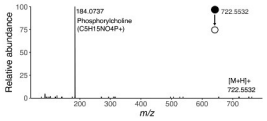

PC(15:0_16:0) negative mode

In vitro #1

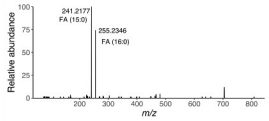

PC(15:0_16:0) positive mode

In vitro #2

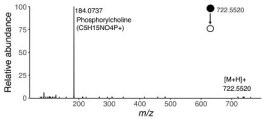

PC(15:0_16:0) negative mode

In vitro #2

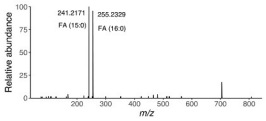

PC(18:1_19:3) positive mode

In vitro #1

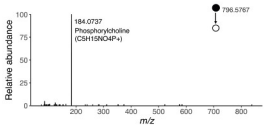

PC(18:1_19:3) negative mode

In vitro #1

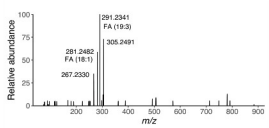

PC(18:1_19:3) positive mode

In vitro #2

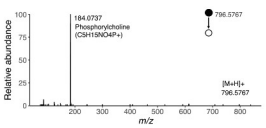

PC(18:1_19:3) negative mode

In vitro #2

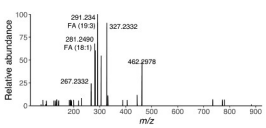

Odd chain lipids in Fig. 3B

PE(17:0_20:4) positive mode

In vitro #1

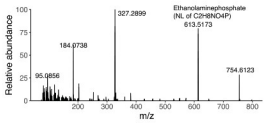

PE(17:0_20:4) negative mode

In vitro #1

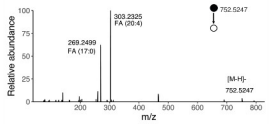

PE(17:0_20:4) positive mode

GPMV

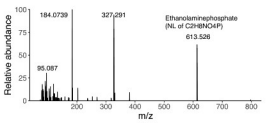

PE(17:0_20:4) negative mode

GPMV

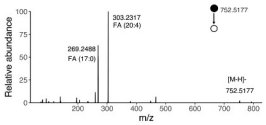

PE(P-18:1_17:1) positive mode

In vitro #1

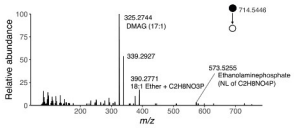

PE(P-18:1_17:1) positive mode

GPMV

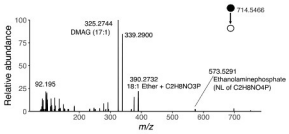

PS(17:0_18:1) positive mode

In vitro #1

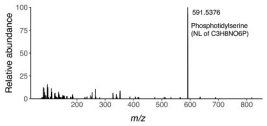

PS(17:0_18:1) negative mode

In vitro #1

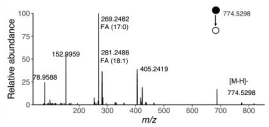

PS(17:0_18:1) positive mode

GPMV

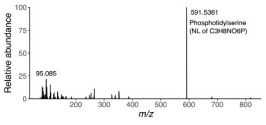

PS(17:0_18:1) negative mode

GPMV

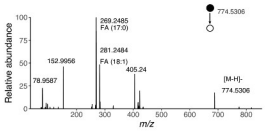

PE(17:0_18:1) positive mode

In vitro #1

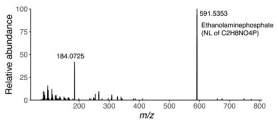

PE(17:0_18:1) negative mode

In vitro #1

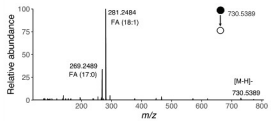

PE(17:0_18:1) positive mode

GPMV

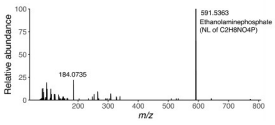

PE(17:0_18:1) negative mode

GPMV

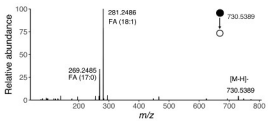

PC(16:0_19:3) positive mode

In vitro #1

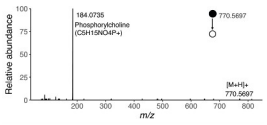

PC(16:0_19:3) negative mode

In vitro #1

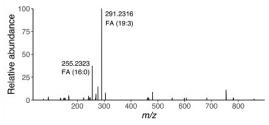

PC(16:0_19:3) positive mode

GPMV

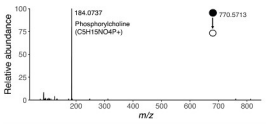

PC(16:0_19:3) negative mode

GPMV

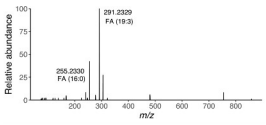

PC(16:1_19:3) positive mode

In vitro #1

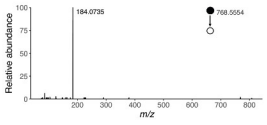

PC(16:1_19:3) negative mode

In vitro #1

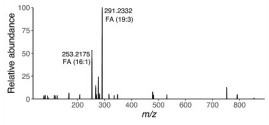

PC(16:1_19:3) positive mode

GPMV

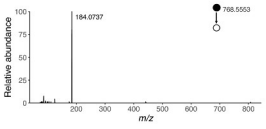

PC(16:1_19:3) negative mode

GPMV

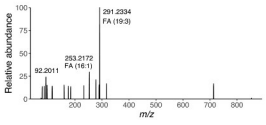

Fig. S3. Spectra validation on identified odd chain-containing lipids from 2 *in vitro* lipidomic studies and GPMV lipidomics.
Top: Tandem mass spectra of odd chain-containing lipids with the top 30% largest effect size in 2 *in vitro* lipidomic studies - PC(15:0_16:0) and PC(18:1_19:3). Bottom: Tandem mass spectra of odd chain-containing lipids in *In vitro* #1 and GPMV lipidomic studies - PE(17:0_20:4) and PE(P-18:1_17:1), PS(17:0_18:1), PE(17:0_18:1), PC(16:0_19:3), PC(16:1_19:3). Solid dot in all spectra represents molecular mass used to identify each molecule (precursor ion).

Figure S4

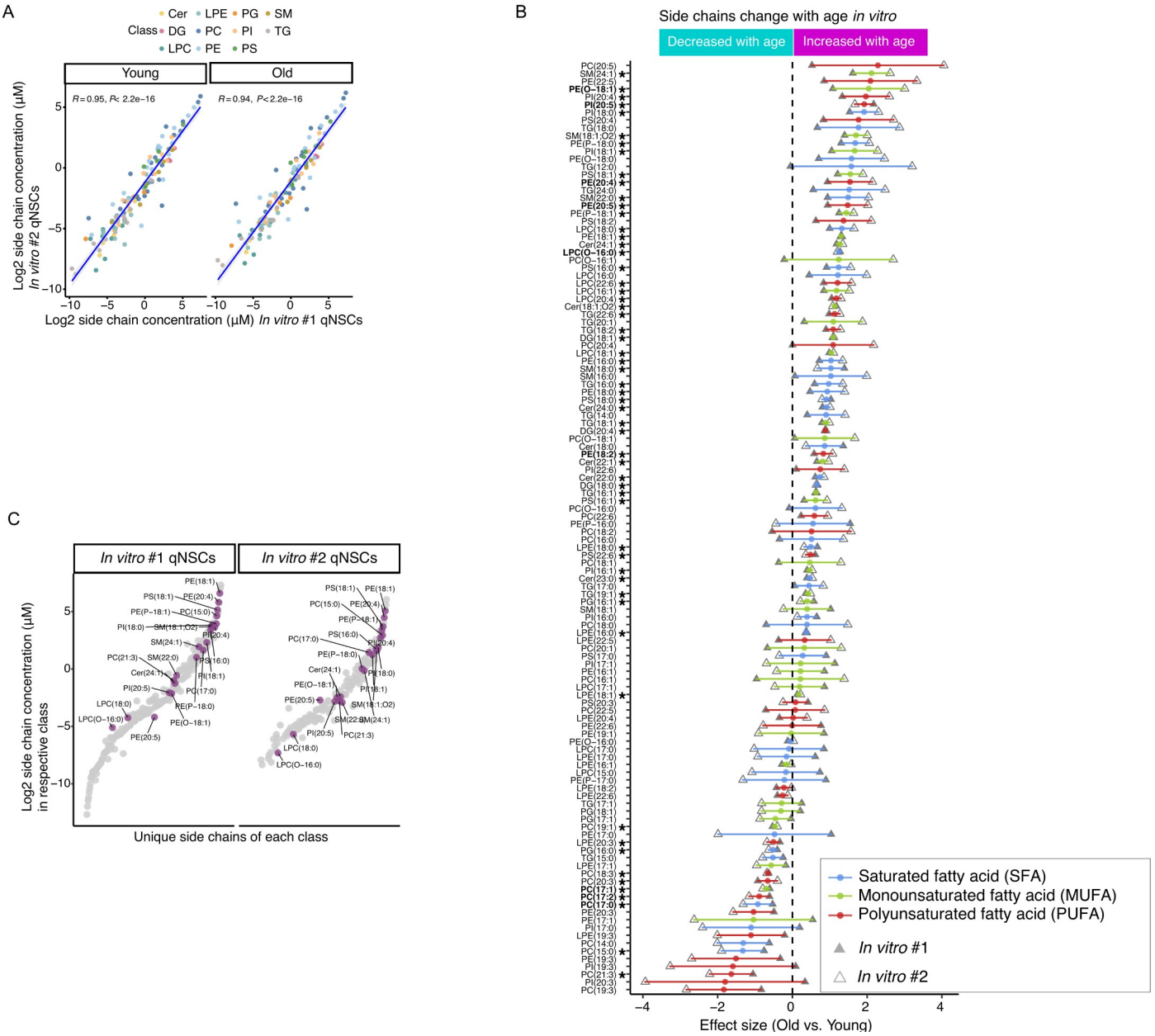
A
Cer
LPE
PG
SM
Class
DG
PC
PI
TG
LPC
PE
PS
Young
Old
R = 0.95, P< 2.2e−16
R = 0.94, P< 2.2e−16
Log2 side chain concentration (μM) In vitro #2 qNSCs
Log2 side chain concentration (μM) In vitro #1 qNSCs
B
Side chains change with age in vitro
Decreased with age
Increased with age
Saturated fatty acid (SFA)
Monounsaturated fatty acid (MUFA)
Polyunsaturated fatty acid (PUFA)
In vitro #1
In vitro #2
Effect size (Old vs. Young)
C
In vitro #1 qNSCs
In vitro #2 qNSCs
Log2 side chain concentration (μM) in respective class
Unique side chains of each class

Fig. S4. Reproducibility of lipidomic changes at side chain composition level in primary neural stem cell cultures *in vitro* from independent lipidomic experiments.
(A) Correlation between side chain composition in young (left panel) and old (right panel) qNSCs between *In vitro* #1 and *In vitro* #2. Pearson correlation was performed on side chain abundance in log2-transformed molar concentration of each lipid class/side chain (solid dots colored by lipid classes) from each dataset. *R* and *P*-values from Pearson correlation are shown. Linear regression line (blue line) with 95% confidence interval (grey shade) is shown. **(B)** Side chain composition changes with age in qNSCs from *In vitro* #1 and *In vitro* #2. All side chain composition features from both studies are plotted. Effect size for changes with age of each feature from *In vitro* #1 (filled triangle) and *In vitro* #2 (empty triangle) is shown together with mean effect size (solid dot) in blue, green and red that represents saturated fatty acid (SFA), monounsaturated fatty acid (MUFA), and polyunsaturated fatty acid (PUFA), respectively. Error bar represents s.e.m. from 2 studies. Statistical significance was assessed based on the *P*-value from test statistics using the 95% confidence interval of the data, and multiple hypothesis correction was done by FDR. Significance is identified when FDR-adjusted $P<0.05$ (see Methods for details). Black asterisk indicates significance. **(C)** Abundance of side chain features with significant change across *in vitro* datasets. Dot plot of side chain features detected in *In vitro* #1 and *In vitro* #2 ordered in molar concentration. Each dot represents a unique lipid class/side chain combination. Significant side chain composition features from both *in vitro* studies are highlighted in purple. Labeled features indicate side chain features that exhibit the top 30% most significant effect size (either increase or decrease with age).

Figure S5

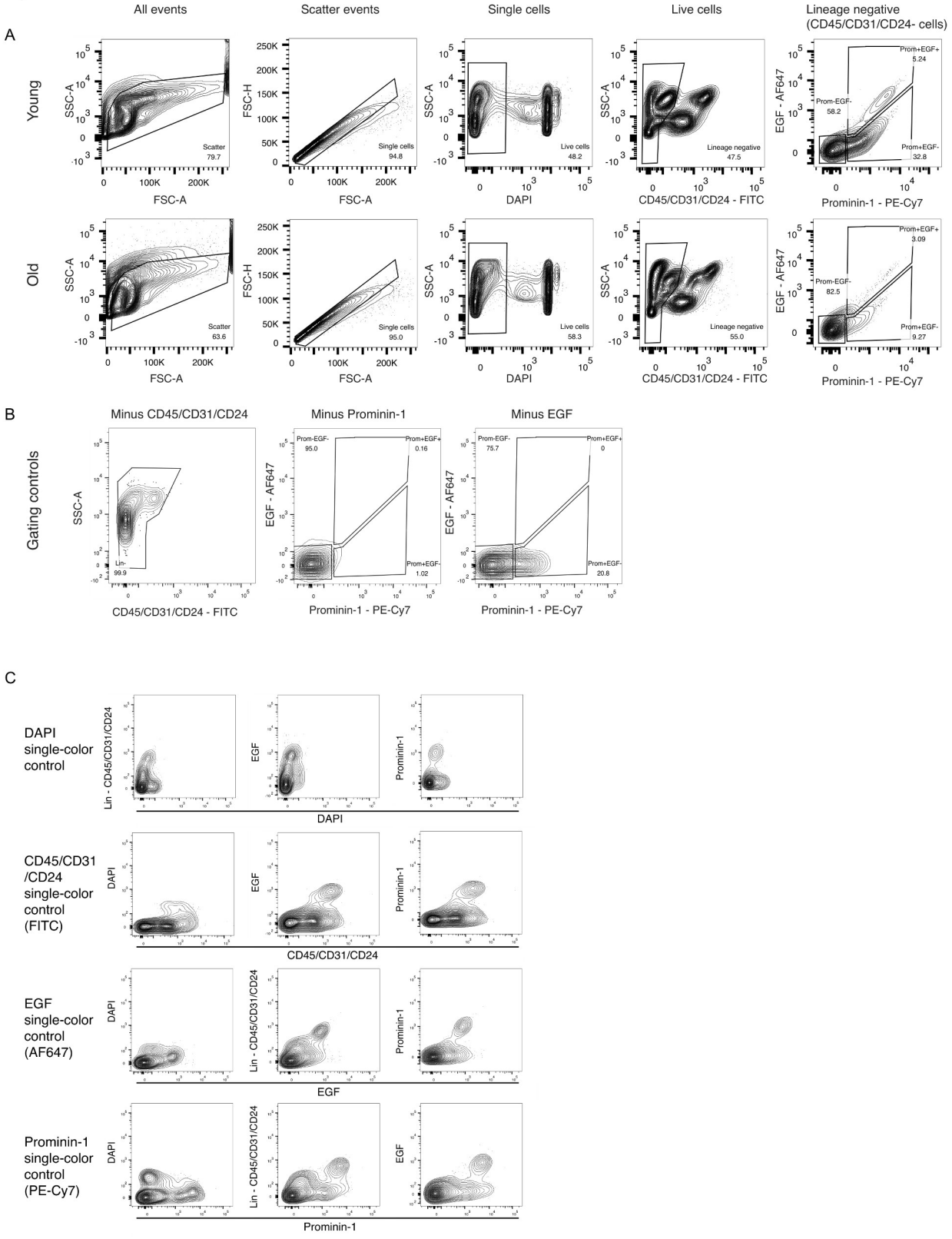
A
All events
Scatter events
Single cells
Live cells
Lineage negative
(CD45/CD31/CD24- cells)
Young
Old
SSC-A
FSC-A
FSC-H
DAPI
CD45/CD31/CD24 - FITC
EGF - AF647
Prominin-1 - PE-Cy7
Scatter
79.7
Single cells
94.8
Live cells
48.2
Lineage negative
47.5
Prom+EGF+
5.24
Prom-EGF-
58.2
Prom+EGF-
32.8
Scatter
63.6
Single cells
95.0
Live cells
58.3
Lineage negative
55.0
Prom+EGF+
3.09
Prom-EGF-
82.5
Prom+EGF-
9.27
B
Gating controls
Minus CD45/CD31/CD24
Minus Prominin-1
Minus EGF
Lin-
99.9
Prom-EGF-
95.0
Prom+EGF+
0.16
Prom+EGF-
1.02
Prom-EGF-
75.7
Prom+EGF+
0
Prom+EGF-
20.8
C
DAPI
single-color
control
CD45/CD31
/CD24
single-color
control
(FITC)
EGF
single-color
control
(AF647)
Prominin-1
single-color
control
(PE-Cy7)
Lin - CD45/CD31/CD24
EGF
Prominin-1
DAPI

Fig. S5. FACS gating scheme of freshly isolated qNSCs.
(A) FACS gating strategy used to freshly isolate quiescent NSCs from the SVZ neurogenic niches of young and old mice. **(B)** Negative gating controls for each staining are indicated. For gating controls, cells were stained with all antibodies except the one for which it is a negative control. **(C)** Single-color staining controls of DAPI, CD45/CD31/CD24 (FITC), EGF (AF647) and Prominin-1 (PE-Cy7) are shown after spectral compensation.

Figure S6

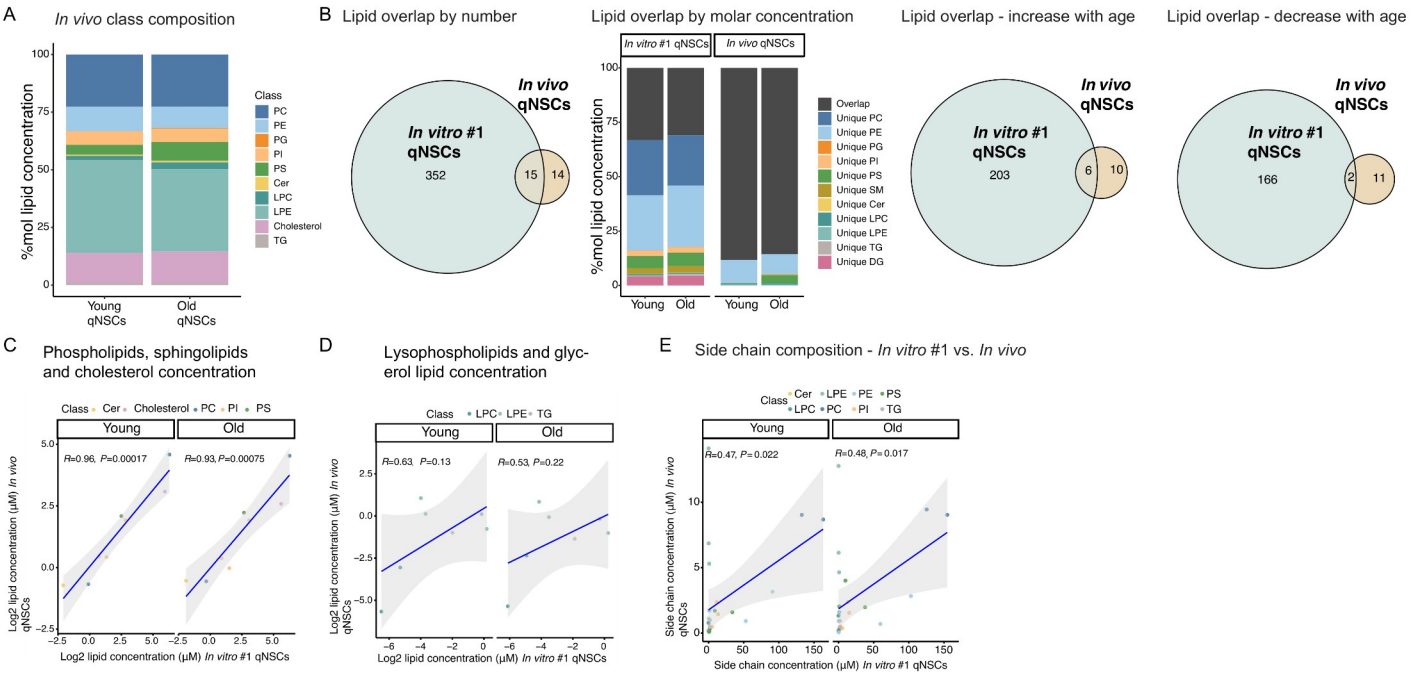
A
In vivo class composition
%mol lipid concentration
Class
PC
PE
PG
PI
PS
Cer
LPC
LPE
Cholesterol
TG
Young qNSCs
Old qNSCs
B
Lipid overlap by number
In vitro #1 qNSCs
352
In vivo qNSCs
15
14
Lipid overlap by molar concentration
In vitro #1 qNSCs
In vivo qNSCs
Overlap
Unique PC
Unique PE
Unique PG
Unique PI
Unique PS
Unique SM
Unique Cer
Unique LPC
Unique LPE
Unique TG
Unique DG
Young
Old
Lipid overlap - increase with age
In vitro #1 qNSCs
203
In vivo qNSCs
6
10
Lipid overlap - decrease with age
In vitro #1 qNSCs
166
In vivo qNSCs
2
11
C
Phospholipids, sphingolipids and cholesterol concentration
Class Cer Cholesterol PC PI PS
Young
Old
R=0.96, P=0.00017
R=0.93, P=0.00075
Log2 lipid concentration (µM) In vivo qNSCs
Log2 lipid concentration (µM) In vitro #1 qNSCs
D
Lysophospholipids and glycerol lipid concentration
Class LPC LPE TG
Young
Old
R=0.63, P=0.13
R=0.53, P=0.22
Log2 lipid concentration (µM) In vivo qNSCs
Log2 lipid concentration (µM) In vitro #1 qNSCs
E
Side chain composition - In vitro #1 vs. In vivo
Class Cer LPE PE PS LPC PC PI TG
Young
Old
R=0.47, P=0.022
R=0.48, P=0.017
Side chain concentration (µM) In vivo qNSCs
Side chain concentration (µM) In vitro #1 qNSCs

Fig. S6. Lipidomic changes of in vivo isolated qNSCs compared to in vitro qNSC primary cultures.
(A) Concentration composition (%mol) of each lipid class on young and old samples from *in vivo* isolated qNSCs. **(B)** Shared lipids from qNSCs *in vitro* and *in vivo*. Venn diagram showing all overlapping lipids (left panel), lipids that increase with age (right-middle panel) and decrease with age (right panel) from *in vitro* #1 and *in vivo* lipidomics. Lipid overlap by molar concentration is presented (left-middle panel) in a stacked bar plot, with individual block corresponding to the concentration composition (%mol) of commonly detected lipids from *in vitro* #1 and *in vivo* (dark grey block) and uniquely detected lipids from each dataset (colored blocks). **(C to D)** Correlation between phospholipids, sphingolipids and cholesterol concentration (**C**) and lysophospholipids and glycerol lipid concentration (**D**) (μM) in young (left panel) and old (right panel) qNSCs from *in vitro* #1 and *in vivo*. Pearson correlation was performed on concentration of individual lipids (solid dots colored by lipid classes) from each dataset. *R* and *P*-values from Pearson correlation are shown. Linear regression line (blue line) with 95% confidence interval (grey shade) is shown. **(E)** Correlation between side chain composition in young (left panel) and old (right panel) qNSCs between *in vitro* #1 and *in vivo*. Pearson correlation was performed on side chain abundance (in molar concentration) of each lipid class/ side chain (solid dots colored by lipid classes) from each dataset. *R* and *P*-values from Pearson correlation are shown. Linear regression line (blue line) with 95% confidence interval (grey shade) is shown.

Figure S7

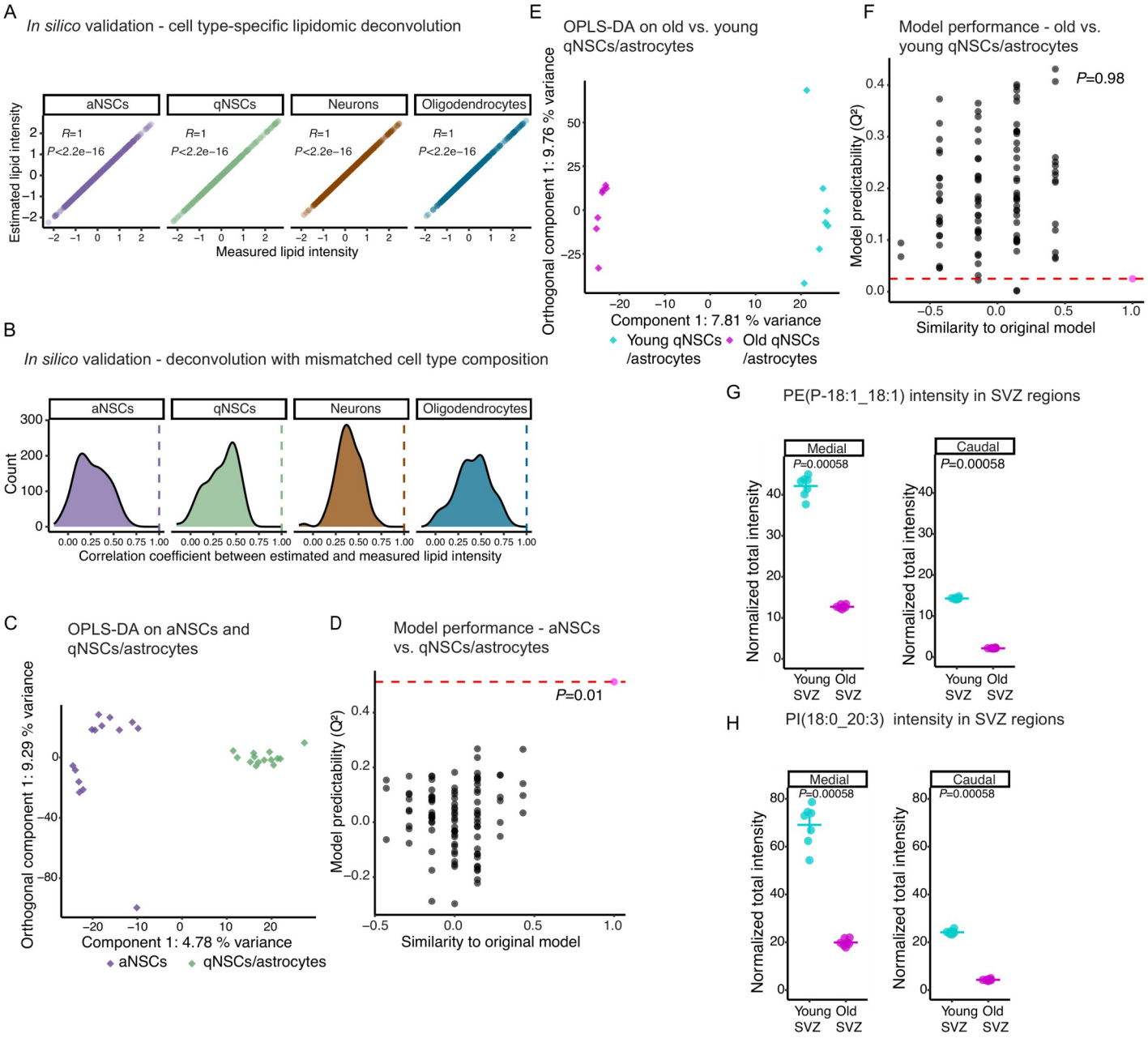
A
In silico validation - cell type-specific lipidomic deconvolution
aNSCs
qNSCs
Neurons
Oligodendrocytes
R=1
P<2.2e-16
Estimated lipid intensity
Measured lipid intensity
B
In silico validation - deconvolution with mismatched cell type composition
Count
Correlation coefficient between estimated and measured lipid intensity
C
OPLS-DA on aNSCs and qNSCs/astrocytes
Orthogonal component 1: 9.29 % variance
Component 1: 4.78 % variance
aNSCs
qNSCs/astrocytes
D
Model performance - aNSCs vs. qNSCs/astrocytes
P=0.01
Model predictability (Q²)
Similarity to original model
E
OPLS-DA on old vs. young qNSCs/astrocytes
Orthogonal component 1: 9.76 % variance
Component 1: 7.81 % variance
Young qNSCs /astrocytes
Old qNSCs /astrocytes
F
Model performance - old vs. young qNSCs/astrocytes
P=0.98
Model predictability (Q²)
Similarity to original model
G
PE(P-18:1_18:1) intensity in SVZ regions
Medial
Caudal
P=0.00058
Normalized total intensity
Young SVZ
Old SVZ
H
PI(18:0_20:3) intensity in SVZ regions
Medial
Caudal
P=0.00058
Normalized total intensity
Young SVZ
Old SVZ

Fig. S7. Metabolomic profiling on young and old subventricular zone neurogenic niches by DESI-MSI.

(A) Cell type-specific deconvolution from *in silico* mixture lipidomic data. Pearson correlation was performed between the Z score of measured lipid intensity and Z score of estimated lipid intensity of activated NSC (aNSC), quiescent NSC (qNSC), neurons and oligodendrocytes from a reconstituted mixture lipidomic dataset (see Methods for details). Each dot represents a lipid species detected from an individual culture of brain cell type. *R* and *P*-values from Pearson correlation are shown. **(B)** Deconvolution from *in silico* mixture lipidomic data with mismatched cell type proportions using randomly-generated cell type compositions (see Methods for details). Density plot shows the number of occurrence (Y axis) of the Pearson correlation coefficient (X axis) of each lipid species between measured and estimated lipid intensity for each individual cell type after deconvolution. Dashed line indicates the correlation coefficient obtained from deconvolution when the matching cell proportions were used (same as panel a). **(C and E)** Orthogonal partial least squares-discriminant analysis (OPLS-DA) on DESI-MSI metabolomic profiling of SVZ cells from n=7 young (3-5 months) and n=7 old (20-22 months) C57BL/6JN male mice. OPLS-DA was performed to obtain cell type-specific metabolic signatures between aNSCs and qNSCs/astrocytes (**C**), and age-related metabolic signatures between young and old qNSCs/astrocytes (**E**). Each data point represents a deconvolved metabolomic profile of a specific cell type from an individual young or old mouse. Data points are plotted based on the predictive score (Component 1, X axis) and the orthogonal predictive score (Orthogonal component 1, Y axis). **(D and F)** Predictability of OPLS-DA model was assessed by permutation test. Similarity to the original model (X axis) and model predictability index (Q^2) (Y axis) from the original model (pink dot on the right of the red dashed line) and individual permutation tests (black dots) are plotted for OPLS-DA model identifying cell type-specific metabolic signatures (**D**) and OPLS-DA model identifying age-related metabolic signatures between young and old qNSCs/astrocytes (**F**). *P*-values were calculated on Q^2 between the original and permutated models. Red dashed line represents the Q^2 index from the original model. **(G and H)** Quantification of the normalized lipid intensity in the medial (left) and caudal (right) region of the SVZ on PE(P-18:1_18:1) (**G**) and PI(18:0_20:3) (**H**). Dot and whisker plot with each individual dot representing the normalized intensity of specified lipids in the medial (left) and caudal (right) region of SVZ from an individual animal. Whisker: +/- s.e.m.. *P*-values from Wilcoxon rank-sum test.

Figure S8

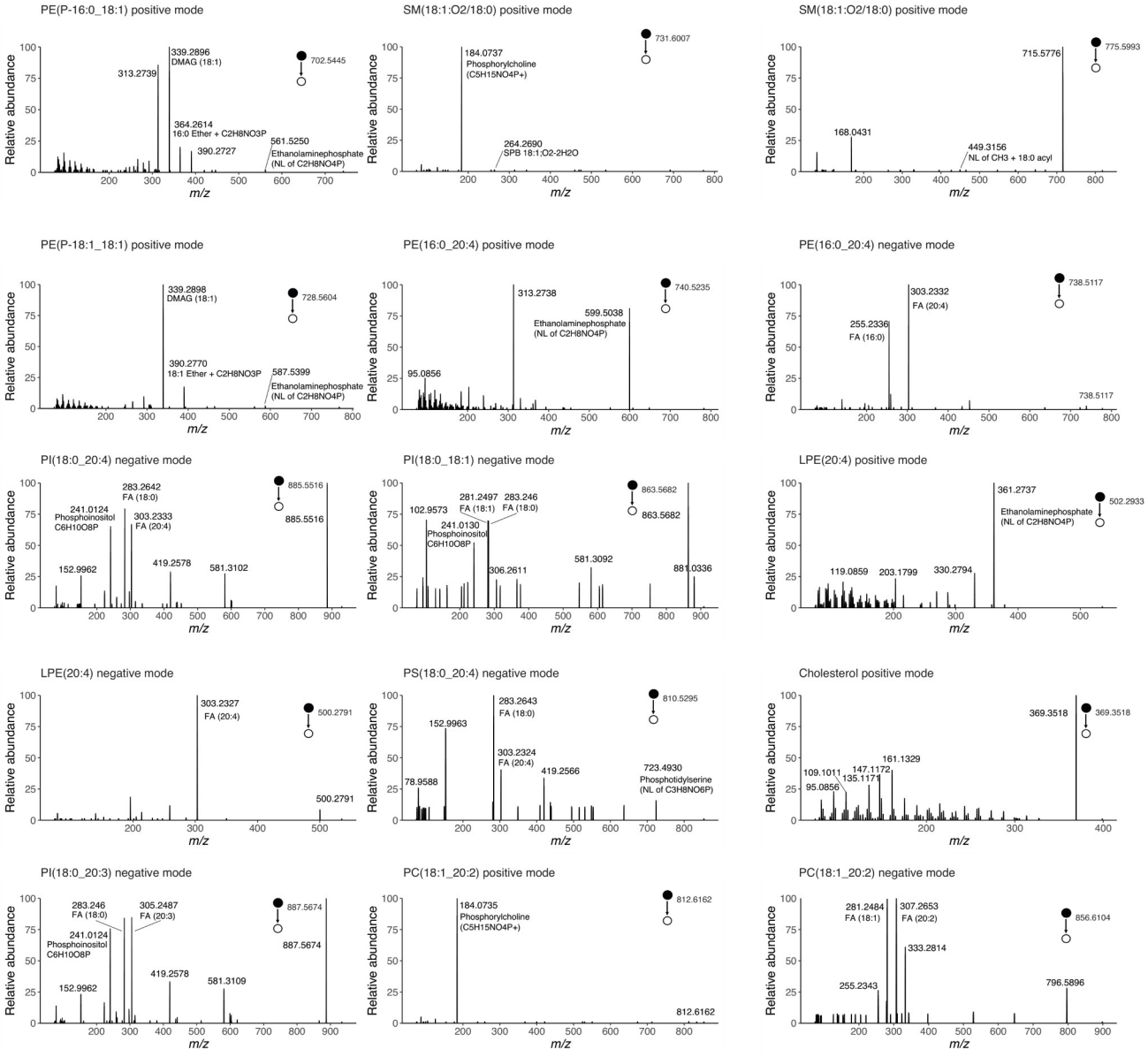
PE(P-16:0_18:1) positive mode
339.2896
DMAG (18:1)
313.2739
702.5445
364.2614
16:0 Ether + C2H8NO3P
390.2727
561.5250
Ethanolaminephosphate
(NL of C2H8NO4P)
SM(18:1:O2/18:0) positive mode
731.6007
184.0737
Phosphorylcholine
(C5H15NO4P+)
264.2690
SPB 18:1:O2-2H2O
SM(18:1:O2/18:0) positive mode
775.5993
715.5776
168.0431
449.3156
NL of CH3 + 18:0 acyl
PE(P-18:1_18:1) positive mode
339.2898
DMAG (18:1)
728.5604
390.2770
18:1 Ether + C2H8NO3P
587.5399
Ethanolaminephosphate
(NL of C2H8NO4P)
PE(16:0_20:4) positive mode
740.5235
313.2738
599.5038
Ethanolaminephosphate
(NL of C2H8NO4P)
95.0856
PE(16:0_20:4) negative mode
738.5117
303.2332
FA (20:4)
255.2336
FA (16:0)
738.5117
PI(18:0_20:4) negative mode
885.5516
283.2642
FA (18:0)
241.0124
Phosphoinositol
C6H10O8P
303.2333
FA (20:4)
885.5516
152.9962
419.2578
581.3102
PI(18:0_18:1) negative mode
863.5682
281.2497
FA (18:1)
283.246
FA (18:0)
102.9573
241.0130
Phosphoinositol
C6H10O8P
863.5682
581.3092
306.2611
881.0336
LPE(20:4) positive mode
361.2737
502.2933
Ethanolaminephosphate
(NL of C2H8NO4P)
119.0859
203.1799
330.2794
LPE(20:4) negative mode
303.2327
FA (20:4)
500.2791
500.2791
PS(18:0_20:4) negative mode
810.5295
283.2643
FA (18:0)
152.9963
303.2324
FA (20:4)
78.9588
419.2566
723.4930
Phosphotidylserine
(NL of C3H8NO6P)
Cholesterol positive mode
369.3518
369.3518
161.1329
109.1011
147.1172
135.1171
95.0856
PI(18:0_20:3) negative mode
887.5674
283.246
FA (18:0)
305.2487
FA (20:3)
241.0124
Phosphoinositol
C6H10O8P
887.5674
152.9962
419.2578
581.3109
PC(18:1_20:2) positive mode
812.6162
184.0735
Phosphorylcholine
(C5H15NO4P+)
812.6162
PC(18:1_20:2) negative mode
856.6104
281.2484
FA (18:1)
307.2653
FA (20:2)
333.2814
255.2343
796.5896
Relative abundance
m/z

Fig. S8. Spectra validation on identified lipids in DESI-MSI.
Tandem mass spectrometry validation following DESI-MSI. Validation of lipid annotation by tandem mass spectrometry for PE(P-16:0_18:1), SM(18:1;O2/18:0), PE(P-18:1_18:1), PE(16:0_20:4), PI(18:0_20:4), PI(18:0_18:1), LPE(20:4), PS(18:0_20:4), Cholesterol, PI(18:0_20:3) and PC(18:1_20:2). Solid dot in all spectra represents molecular mass used to identify each molecule (precursor ion).

Figure S9

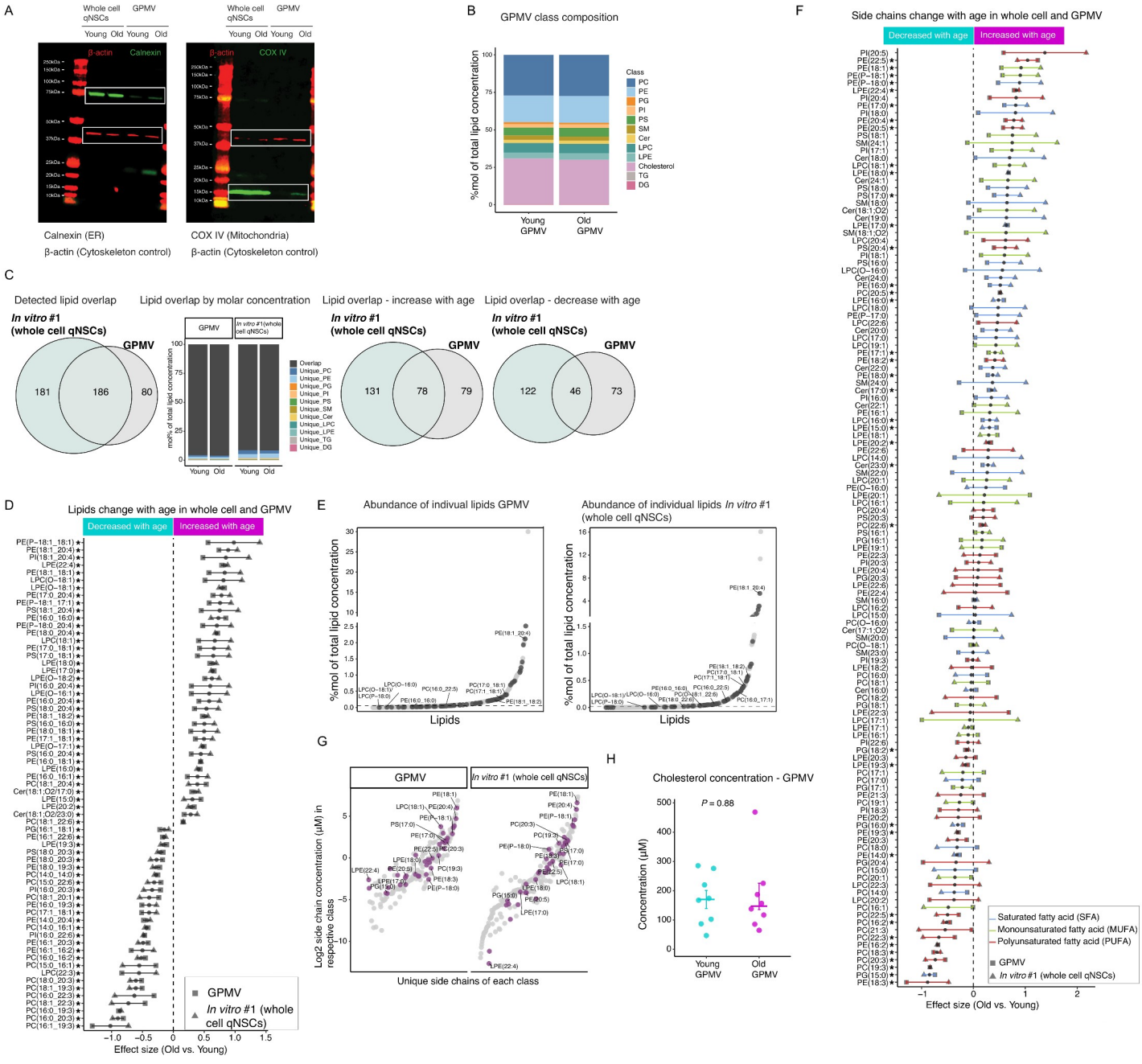
A
Whole cell qNSCs
GPMV
Young Old Young Old
β-actin
Calnexin
COX IV
Calnexin (ER)
β-actin (Cytoskeleton control)
COX IV (Mitochondria)
β-actin (Cytoskeleton control)
B
GPMV class composition
%mol of total lipid concentration
Young GPMV
Old GPMV
Class
PC
PE
PG
PI
PS
SM
Cer
LPC
LPE
Cholesterol
TG
DG
C
Detected lipid overlap
Lipid overlap by molar concentration
Lipid overlap - increase with age
Lipid overlap - decrease with age
In vitro #1 (whole cell qNSCs)
GPMV
181
186
80
131
78
79
122
46
73
Overlap
Unique_PC
Unique_PE
Unique_PG
Unique_PI
Unique_PS
Unique_SM
Unique_Cer
Unique_LPC
Unique_LPE
Unique_TG
Unique_DG
D
Lipids change with age in whole cell and GPMV
Decreased with age
Increased with age
GPMV
In vitro #1 (whole cell qNSCs)
Effect size (Old vs. Young)
E
Abundance of indivual lipids GPMV
Abundance of individual lipids In vitro #1 (whole cell qNSCs)
%mol of total lipid concentration
Lipids
PE(18:1_20:4)
F
Side chains change with age in whole cell and GPMV
Decreased with age
Increased with age
Saturated fatty acid (SFA)
Monounsaturated fatty acid (MUFA)
Polyunsaturated fatty acid (PUFA)
GPMV
In vitro #1 (whole cell qNSCs)
Effect size (Old vs. Young)
G
GPMV
In vitro #1 (whole cell qNSCs)
Log2 side chain concentration (μM) in respective class
Unique side chains of each class
H
Cholesterol concentration - GPMV
P = 0.88
Concentration (μM)
Young GPMV
Old GPMV

Fig. S9. Plasma membrane lipids change with age in quiescent neural stem cells.
(A) Western blot on protein extracts from whole cell lysates or giant plasma membrane vesicles (GPMVs) generated from primary qNSC cultures from young (3-5 months) and old (20-22 months) mice. Membranes were incubated with antibodies to cytoskeleton control β-actin (red), endoplasmic reticulum marker Calnexin (green), and mitochondria marker COX IV (green). **(B)** Concentration composition (%mol) of each lipid class on GPMVs from young and old primary qNSC cultures. **(C)** Shared lipids from qNSCs of GPMV and *In vitro* #1 lipidomics. Venn diagram showing all overlapping lipids (left panel), lipids that increase with age (right-middle panel) and decrease with age (right panel) in GPMV and *In vitro* #1. Lipid overlap by molar concentration is presented (left-middle panel) in a stacked bar plot, with individual block corresponding to the concentration composition (%mol) of commonly detected lipids in GPMV and *In vitro* #1 (dark grey block) and uniquely detected lipids from each dataset (colored blocks). **(D)** Lipids change with age in qNSCs of GPMV and *In vitro* #1. Significant lipids that change with age by effect size in GPMV and *In vitro* #1 are plotted. Effect size for each lipid from *In vitro* #1 (filled triangle) and GPMV (square) is shown together with mean effect size (black dot) and s.e.m. (error bar) from 2 studies. Significance is identified when FDR-adjusted $P<0.05$ (see Methods for details). Black asterisk indicates significance. **(E)** Abundance of individual lipids in GPMV and *In vitro* #1. Dot plot of all detected lipids in GPMV and *In vitro* #1 is ordered in %mol of total lipid concentration. Each dot represents an individual lipid species (light grey). Significant lipids from both studies (as listed in **D**) are highlighted in dark grey. Text label indicates lipids of interest that significantly change with age (**Figure 1**) and with intervention (**Figure 4**). Dashed line indicates median lipid abundance of each dataset. **(F)** Side chain composition changes with age in whole cell and GPMV from qNSC primary cultures. Effect size on changes with age of side chain composition features from GPMV (square) and *In vitro* #1 (filled triangle) is plotted together with mean effect size (solid dot) in blue, green and red that represents saturated fatty acid (SFA), monounsaturated fatty acid (MUFA), and polyunsaturated fatty acid (PUFA), respectively. Error bar represents s.e.m. from GPMV and *In vitro* #1. Significance is identified when FDR-adjusted $P<0.05$ (see Methods for details). Black asterisk indicates significance. For statistical test of age-related effect sizes on lipids (**D**) and side chain compositions (**F**), statistical significance was assessed based on the *P*-value from test statistics using the 95% confidence interval of the data, and multiple hypothesis correction was done by FDR. **(G)** Abundance of side chain features with significant changes in GPMV and *In vitro* #1. Dot plot of side chain composition features detected in GPMV and *In vitro* #1 is ordered in molar concentration. Each dot represents a unique lipid class/side chain combination. Significant side chain composition features from both studies (as listed in **Fig. 3C**) are highlighted in purple. Labeled features indicate side chain features that exhibit the top 30% most significant effect size (either increase or decrease with age). **(H)** Cholesterol concentration from plasma membrane of young and old qNSCs. Cholesterol concentration from GPMV lipidomics of primary qNSC cultures of n=8 young (3-5 months) and n=8 old (20-22 months) mice. Each dot represents a GPMV sample, generated from a primary qNSC culture that was established with an individual mouse. Bar plot represents mean +/- s.e.m.. *P*-value from Wilcoxon rank-sum test.

Figure S10

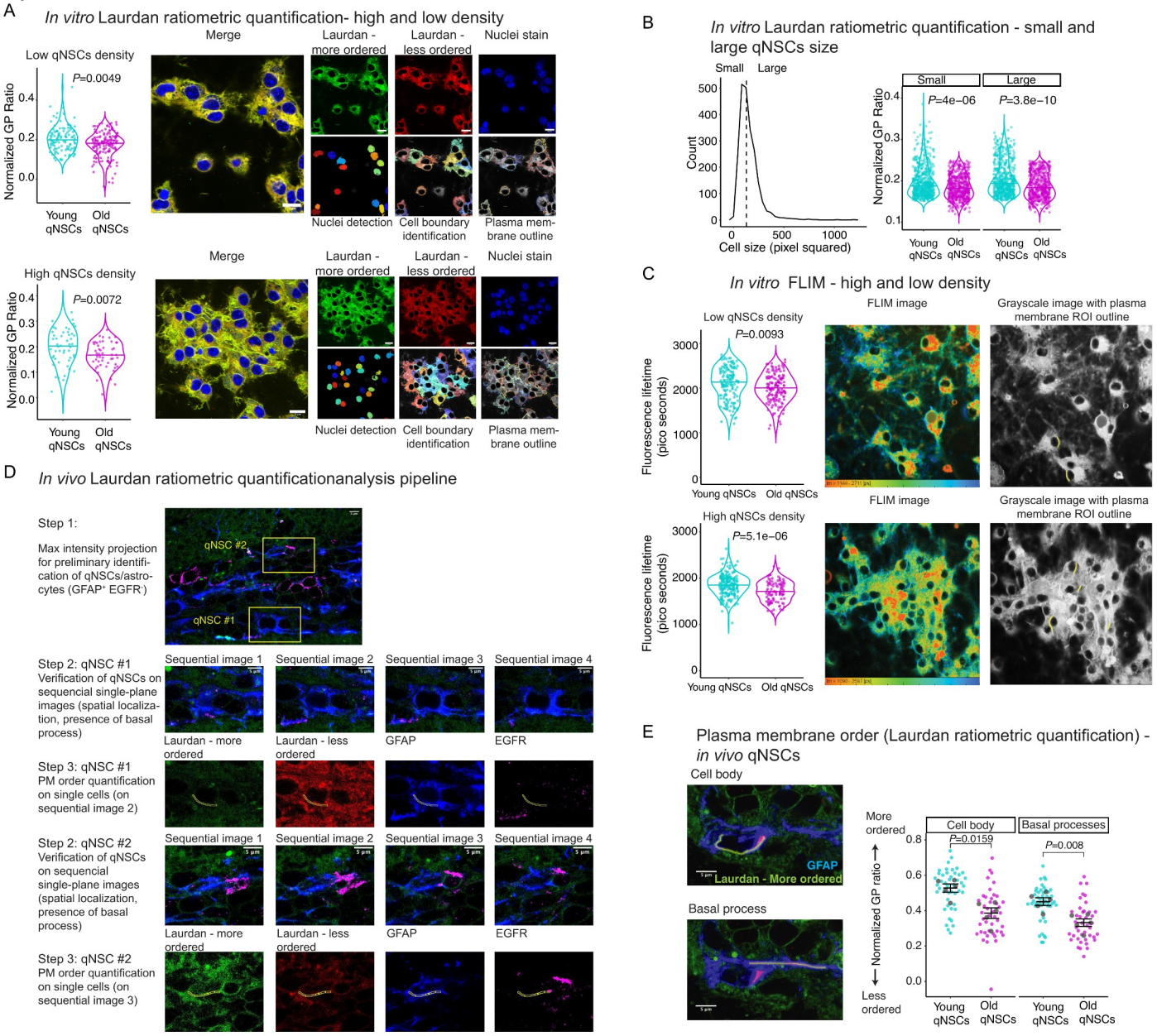
A
In vitro Laurdan ratiometric quantification- high and low density
Merge
Laurdan - more ordered
Laurdan - less ordered
Nuclei stain
Low qNSCs density
P=0.0049
Normalized GP Ratio
Young qNSCs
Old qNSCs
Nuclei detection
Cell boundary identification
Plasma membrane outline
High qNSCs density
P=0.0072
B
In vitro Laurdan ratiometric quantification - small and large qNSCs size
Small
Large
Count
Cell size (pixel squared)
P=4e−06
P=3.8e−10
C
In vitro FLIM - high and low density
FLIM image
Grayscale image with plasma membrane ROI outline
Low qNSCs density
P=0.0093
Fluorescence lifetime (pico seconds)
High qNSCs density
P=5.1e−06
D
In vivo Laurdan ratiometric quantificationanalysis pipeline
Step 1:
Max intensity projection for preliminary identification of qNSCs/astrocytes (GFAP+ EGFR-)
qNSC #2
qNSC #1
Step 2: qNSC #1
Verification of qNSCs on sequencial single-plane images (spatial localization, presence of basal process)
Sequential image 1
Sequential image 2
Sequential image 3
Sequential image 4
Laurdan - more ordered
Laurdan - less ordered
GFAP
EGFR
Step 3: qNSC #1
PM order quantification on single cells (on sequential image 2)
Step 2: qNSC #2
Verification of qNSCs on sequencial single-plane images (spatial localization, presence of basal process)
Step 3: qNSC #2
PM order quantification on single cells (on sequential image 3)
E
Plasma membrane order (Laurdan ratiometric quantification) - in vivo qNSCs
Cell body
GFAP
Laurdan - More ordered
Basal process
More ordered
Less ordered
Normalized GP ratio
Cell body
Basal processes
P=0.0159
P=0.008

Fig. S10. Plasma membrane order change with age in qNSCs *in vitro* and *in vivo*.
(A) Plasma membrane order assessed *in vitro* by Laurdan staining in low cell density (top) and high cell density (bottom). Left: Plasma membrane order quantified by generalized polarization ratio (GP ratio) from Laurdan staining of young and old qNSCs. Violin plot showing data from individual cells (cyan/purple dots). Results from one independent experiment, n=4 primary cultures. *P*-value from Wilcoxon rank-sum test. Middle: Image from Laurdan rigid wavelength (more ordered, green) overlaid with Laurdan fluid wavelength (less ordered, red) and nuclei staining (blue) is shown. Right: Confocal images captured from individual wavelength (top) and steps of automated image analysis pipeline for plasma membrane order quantification (bottom). Scale bar represents 10μm. **(B)** Plasma membrane order assessed *in vitro* by Laurdan staining based on cell size. Left: Cell size distribution of individual qNSCs from primary young and old qNSC culture. Vertical dashed line indicates the median size of all cells quantified. Right: Plasma membrane order quantified by generalized polarization ratio (GP ratio) from Laurdan staining of young and old qNSCs. Violin plot showing data from individual cells (cyan/purple dots) that are either smaller or larger than the median cell size. Results from one independent experiment, n=4 primary cultures. *P*-values from Wilcoxon rank-sum test. **(C)** Plasma membrane order assessed *in vitro* by FLIM imaging in low cell density (top) and high cell density (bottom). Left: Plasma membrane order quantified by FLIM imaging of young and old qNSCs. Volin plots showing data from individual cells (cyan/purple dots). Results from two experiments combined, n=6 primary cultures. *P*-values from Wilcoxon rank-sum test. Middle: Representative FLIM image. Color scale corresponds to fluorescent lifetime throughout the cell. Right: Grayscale image with plasma membrane outlined in yellow for plasma membrane order quantification. **(D)** Additional examples of *in vivo* qNSC plasma membrane order quantification by Laurdan staining and ratiometric quantification. Row 1: Max intensity projection from a Z stack of confocal images showing Laurdan rigid wavelength (more ordered, green) overlaid with GFAP (NSC and astrocyte marker, blue) and EGFR (proliferation marker, purple) staining. Two individual qNSCs (qNSC #1 and #2), based on markers ($GFAP^+EGFR^-$), spatial localization (immediately adjacent to ependymal cells that line the lateral ventricles) and the presence of a basal process, are highlighted for the analysis pipeline below. Rows 2-5: Sequential single-plane images from the Z stack image enlarged to demonstrate the image analysis pipeline of plasma membrane order quantification on 2 single cells *in vivo* (rows 2 and 4) and images from individual wavelength from a single-plane (Z=2 for qNSC #1 and Z=3 for qNSC #2, rows 3 and 5) of the Z stack. Scale bar represents 10μm. **(E)** Plasma membrane lipid order assessed by Laurdan ratiometric quantification of different subcellular regions in qNSCs *in vivo* from n=5 young (3-5 months) and n=5 old (20-22 months) mice. Left: representative Laurdan staining on *in vivo* qNSCs from SVZ. Image taken from rigid wavelength (more ordered, green) is overlaid with GFAP (NSC and astrocyte marker, blue). Plasma membrane segment around the cell body as well as around the basal process is outlined in yellow. Right: Membrane order quantified by generalized polarization ratio (GP ratio) from Laurdan staining. SuperPlots showing data from individual cells (cyan/purple dots), as well as the mean of each mouse (gray dots) +/- s.e.m.. Results are from one independent experiment, n=5 mice. *P*-values from Wilcoxon rank-sum test. Results from a second independent experiment are in **Table S14**.

Figure S11

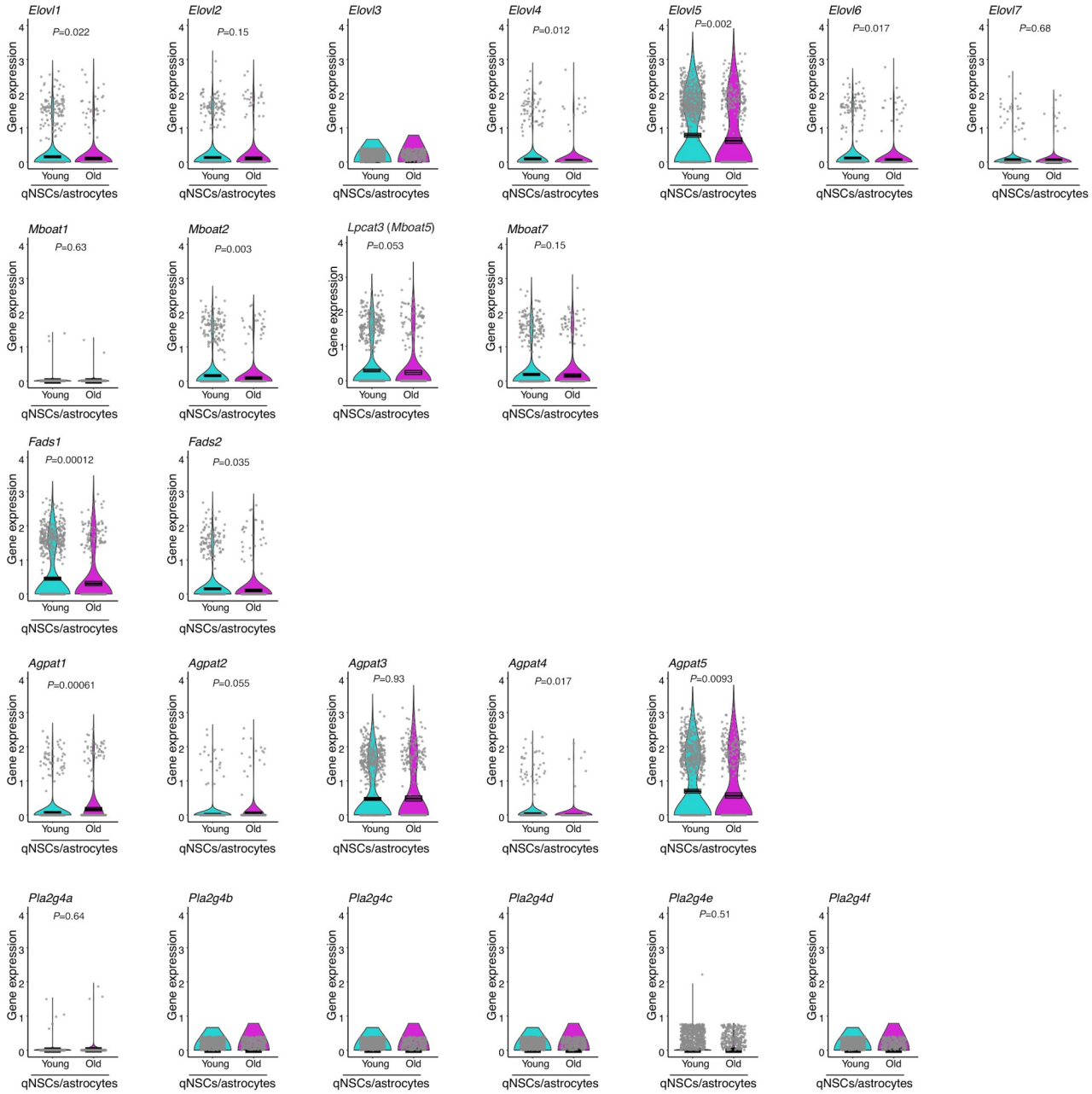
Elovl1
P=0.022
Elovl2
P=0.15
Elovl3
Elovl4
P=0.012
Elovl5
P=0.002
Elovl6
P=0.017
Elovl7
P=0.68
Mboat1
P=0.63
Mboat2
P=0.003
Lpcat3 (Mboat5)
P=0.053
Mboat7
P=0.15
Fads1
P=0.00012
Fads2
P=0.035
Agpat1
P=0.00061
Agpat2
P=0.055
Agpat3
P=0.93
Agpat4
P=0.017
Agpat5
P=0.0093
Pla2g4a
P=0.64
Pla2g4b
Pla2g4c
Pla2g4d
Pla2g4e
P=0.51
Pla2g4f
Gene expression
Young
Old
qNSCs/astrocytes

Fig. S11. *In vivo* expression level of selected genes encoding lipid modification enzymes and other genes in the same enzyme family.

Violin plots of gene expression in young and old qNSCs/astrocytes from single-cell RNA-seq datasets (see Methods for detail). Five selected genes encoding lipid modification enzymes (*Elovl5*, *Mboat2*, *Fads2*, *Agpat3*, *Pla2g4e*), and other genes in the same enzyme family (*Elovl1*, *Elovl2*, *Elovl3*, *Elovl4*, *Elovl6*, *Elovl7*, *Mboat1*, *Lpcat3 (Mboat5)*, *Mboat7*, *Fads1, Agpat1*, *Agpat2*, *Agpat4*, *Agpat5*, *Pla2g4a*, *Pla2g4b*, *Pla2g4c*, *Pla2g4d*, *Pla2g4f*) are included. Boxplot represents mean expression level +/- s.e.m.. Each individual dot represents the normalized gene expression of specified gene in a single cell. Gray bar at the bottom represents cells with gene expression level below detection limit. *P*-values from Wilcoxon rank-sum test. No *P*-value is indicated if expression was not detected in any cells from young or old samples.

Figure S12

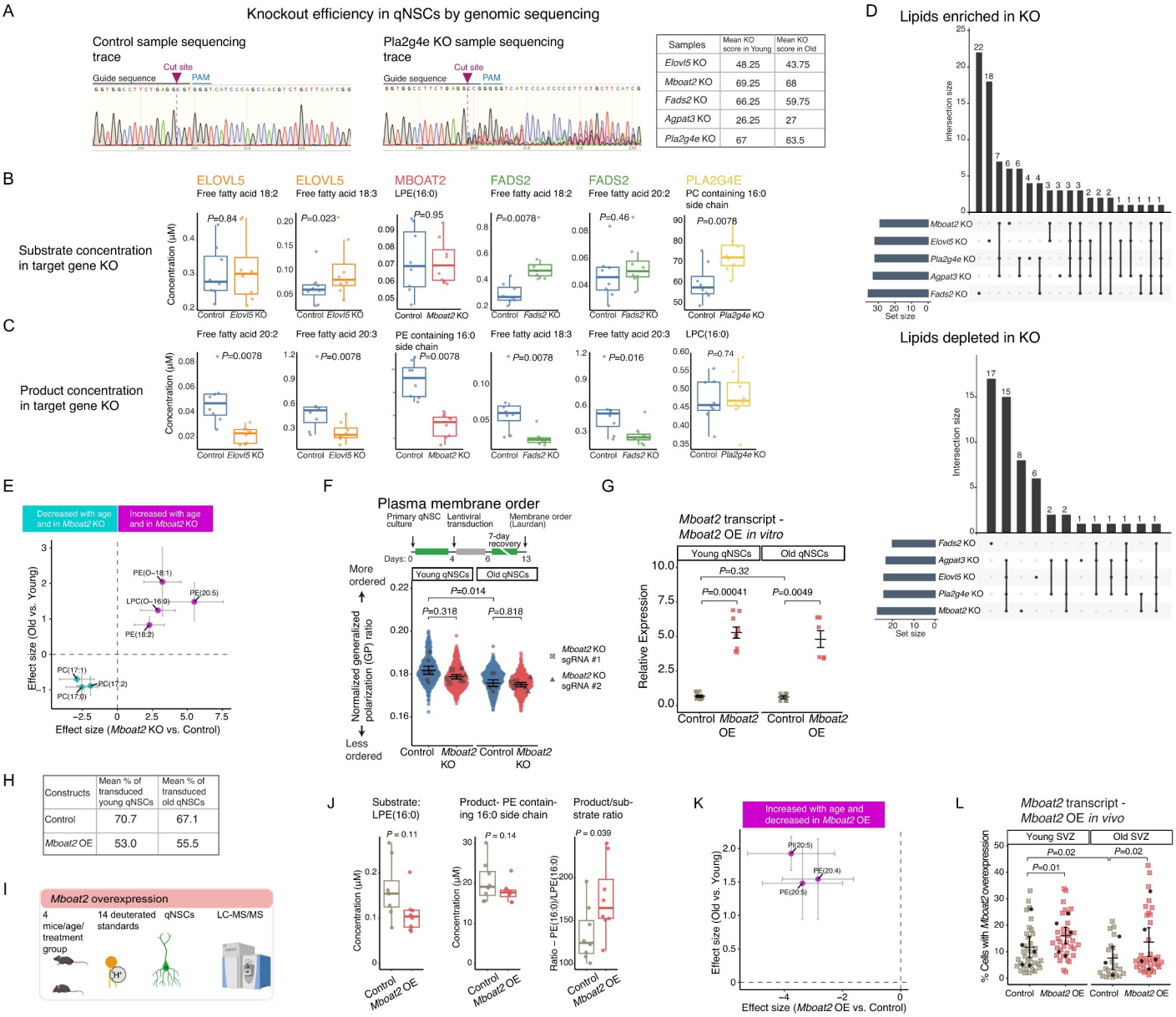
A
Knockout efficiency in qNSCs by genomic sequencing
Control sample sequencing trace
Cut site
Guide sequence
PAM
Pla2g4e KO sample sequencing trace
Cut site
Guide sequence
PAM
Samples | Mean KO score in Young | Mean KO score in Old
Elovl5 KO | 48.25 | 43.75
Mboat2 KO | 69.25 | 68
Fads2 KO | 66.25 | 59.75
Agpat3 KO | 26.25 | 27
Pla2g4e KO | 67 | 63.5
B
Substrate concentration in target gene KO
ELOVL5 Free fatty acid 18:2
ELOVL5 Free fatty acid 18:3
MBOAT2 LPE(16:0)
FADS2 Free fatty acid 18:2
FADS2 Free fatty acid 20:2
PLA2G4E PC containing 16:0 side chain
Concentration (μM)
P=0.84
P=0.023
P=0.95
P=0.0078
P=0.46
P=0.0078
Control Elovl5 KO
Control Elovl5 KO
Control Mboat2 KO
Control Fads2 KO
Control Fads2 KO
Control Pla2g4e KO
C
Product concentration in target gene KO
Free fatty acid 20:2
Free fatty acid 20:3
PE containing 16:0 side chain
Free fatty acid 18:3
Free fatty acid 20:3
LPC(16:0)
Concentration (μM)
P=0.0078
P=0.0078
P=0.0078
P=0.0078
P=0.016
P=0.74
Control Elovl5 KO
Control Elovl5 KO
Control Mboat2 KO
Control Fads2 KO
Control Fads2 KO
Control Pla2g4e KO
D
Lipids enriched in KO
Intersection size
Mboat2 KO
Elovl5 KO
Pla2g4e KO
Agpat3 KO
Fads2 KO
Set size
Lipids depleted in KO
Intersection size
Fads2 KO
Agpat3 KO
Elovl5 KO
Pla2g4e KO
Mboat2 KO
Set size
E
Decreased with age and in Mboat2 KO
Increased with age and in Mboat2 KO
Effect size (Old vs. Young)
PE(O−18:1)
PE(20:5)
LPC(O−16:0)
PE(18:2)
PC(17:1)
PC(17:2)
PC(17:0)
Effect size (Mboat2 KO vs. Control)
F
Plasma membrane order
Primary qNSC culture
Lentiviral transduction
Membrane order (Laurdan)
7-day recovery
Days: 0 4 6 13
More ordered
Young qNSCs
Old qNSCs
P=0.014
P=0.318
P=0.818
Normalized generalized polarization (GP) ratio
Less ordered
Mboat2 KO sgRNA #1
Mboat2 KO sgRNA #2
Control Mboat2 KO
Control Mboat2 KO
G
Mboat2 transcript - Mboat2 OE in vitro
Young qNSCs
Old qNSCs
P=0.32
P=0.00041
P=0.0049
Relative Expression
Control Mboat2 OE
Control Mboat2 OE
H
Constructs | Mean % of transduced young qNSCs | Mean % of transduced old qNSCs
Control | 70.7 | 67.1
Mboat2 OE | 53.0 | 55.5
I
Mboat2 overexpression
4 mice/age/treatment group
14 deuterated standards
qNSCs
LC-MS/MS
J
Substrate: LPE(16:0)
Product- PE containing 16:0 side chain
Product/substrate ratio
P = 0.11
P = 0.14
P = 0.039
Concentration (μM)
Concentration (μM)
Ratio - PE(16:0)/LPE(16:0)
Control Mboat2 OE
Control Mboat2 OE
Control Mboat2 OE
K
Increased with age and decreased in Mboat2 OE
Effect size (Old vs. Young)
PE(20:5)
PE(20:4)
PE(20:5)
Effect size (Mboat2 OE vs. Control)
L
Mboat2 transcript - Mboat2 OE in vivo
Young SVZ
Old SVZ
P=0.02
P=0.02
P=0.01
% Cells with Mboat2 overexpression
Control Mboat2 OE
Control Mboat2 OE

Fig. S12. Validation of in vitro genetic manipulations and their effects on the global lipidome of neural stem cells.

(A) Validation of knockout efficiency by genomic DNA sequencing. Representative sequencing traces from control and knockout (KO) samples of the *Pla2g4e* gene with CRISPR editing are shown (left). Mean KO scores in young and old qNSCs are obtained from Inference of CRISPR Edits (ICE) analysis (see Methods for details) (right). **(B to C)** Substrate (**B**) and product (**C**) level in control and knockout (KO) for each target genes in qNSCs. Data are obtained from untargeted lipidomic analysis. Each dot represents a primary culture from an individual young (3-5 months old) or old (20-22 months old) male mouse. Results are from 1 independent experiment, n=4 primary cultures. *P*-values from Wilcoxon rank-sum test. Substrates are: *Elovl5* KO: free fatty acid 18:2 and 18:3, *Mboat2* KO: LPE(16:0), *Fads2* KO: free fatty acid 18:2 and 20:2 and *Pla2g4e* KO: PC containing 16:0 side chain. Products are: *Elovl5* KO: free fatty acid 20:2 and 20:3, *Mboat2* KO: PE containing 16:0 side chain, *Fads2* KO: free fatty acid 18:3 and 20:3 and *Pla2g4e* KO: LPC(16:0). **(D)** Effects on global lipidome of individual gene knockouts. Sets of overlapping lipids and the number of lipids per set in individual knockouts are shown using UpSet plots. Lipids are divided into ones that are enriched in knockout (top) or depleted in knockout (bottom) when compared to control. **(E)** Side chain composition change with *Mboat2* knockout in old qNSCs. Significant side chain features that change with *Mboat2* knockout by effect size are plotted. X axis indicates the effect size of side chain features (individual dots) between *Mboat2* KO vs. control in old qNSCs. Y axis indicates the effect size between young and old qNSCs (from **Fig. 1**). For each side chain feature, mean effect size is shown together with s.e.m. (error bar). Dashed lines indicated effect size of 0. **(F)** Plasma membrane order as assessed by Laurdan *in vitro* on young and old qNSCs with *Mboat2* knockout. Primary qNSC cultures from n=6=7 young (3-5 months) and n=6-7 old (20-22 months) mice were transduced with control lentivirus (sgRNAs targeting an unannotated region of the genome) or with sgRNAs targeting *Mboat2* (2 independent sgRNAs) for 2 consecutive days. Plasma membrane order was assessed at the end of a 7-day recovery period following genetic KO. Plasma membrane order was quantified by generalized polarization ratio (GP ratio) from Laurdan staining on young and old control (blue) or *Mboat2* (red) KO qNSCs. SuperPlots showing data from individual cells (colored dots), as well as the mean of each primary culture (gray dots) +/- s.e.m.. Results from 3 independent experiments, n=6-7 primary cultures. *P*-values from Wilcoxon rank-sum test on quantification of individual animals. **(G)** Validation of *Mboat2* overexpression *in vitro* by RT-qPCR. Relative expression level of *Mboat2* by RT-qPCR is shown for young and old qNSCs with control (grey) or *Mboat2* (red) overexpression. Dot and whisker plot from 2 independent experiments, n=6-9 primary cultures. Horizontal bar: mean. Whisker: +/- s.e.m.. Each dot represents a primary culture from an individual mouse. *P*-values from Wilcoxon rank-sum test. **(H)** Lentiviral transduction efficiency of *Mboat2* overexpression *in vitro*. Mean percentage of transduced cells based on co-expressed reporters in young and old qNSCs are presented. **(I)** Schematic of lipidomic profiling on qNSCs with *Mboat2* overexpression. Number of animals used, number of internal deuterated lipidomic standards used and neural stem cell type included are indicated. **(J)** Validation of *Mboat2* overexpression *in vitro* by the substrate and product level from lipidomic analysis. Lipid concentration of LPE(16:0) (substrate of MBOAT2, left panel), PE containing 16:0 side chain (product of MBOAT2, middle panel), and the ratio between PE containing 16:0 side chain and LPE(16:0) (product to substrate ratio, right panel) are shown. Box and whisker plot from 1 independent experiment, n=4 primary qNSC cultures. Horizontal bar: median. Whisker: Distance between the first/third quartile to the highest/lowest value,

respectively, or 1.5 times the distance between the first/third quartile, whichever is smaller. Each dot represents a primary culture from an individual mouse. *P*-values from Wilcoxon rank-sum test. **(K)** Side chain composition change with *Mboat2* overexpression in old qNSCs. Significant side chain features that change with *Mboat2* overexpression by effect size are plotted. X axis indicates the effect size of side chain features (individual dots) between *Mboat2* OE vs. control in old qNSCs. Y axis indicates the effect size between young and old qNSCs (from **Fig. 1**). For each side chain feature, mean effect size is shown together with s.e.m. (error bar). Dashed lines indicated effect size of 0. **(L)** Validation of *Mboat2* overexpression *in vivo* by *in situ* mRNA hybridization. Percentage of all SVZ cells containing positive staining of *Mboat2* transcripts is quantified in young and old mice transduced with control lentivirus (grey) or lentivirus overexpressing *Mboat2* (red). SuperPlots showing data from individual tiled images (colored legend), as well as the mean of each individual animal (gray dots) +/- s.e.m.. n=3-5 animals. *P*-values from Wilcoxon rank-sum test on quantification of individual animals.

Figure S13

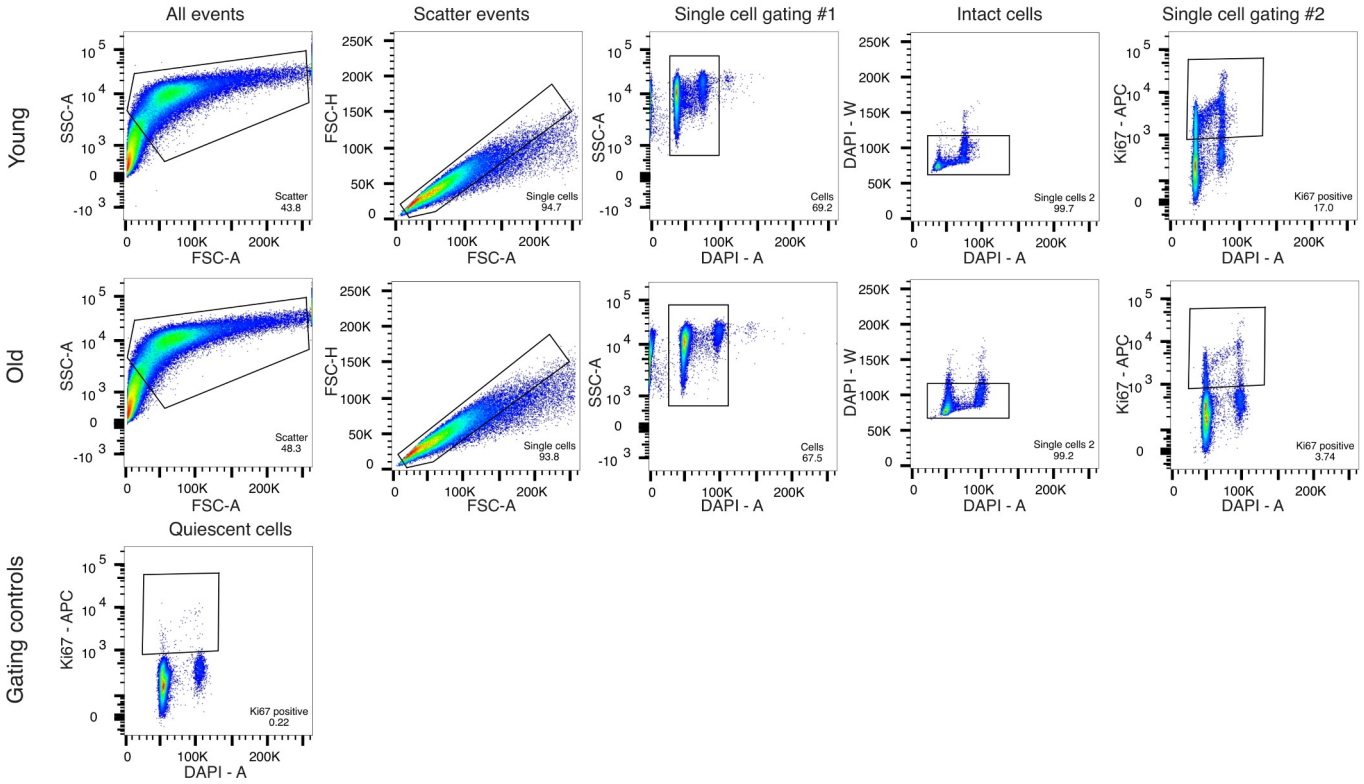
All events
Scatter events
Single cell gating #1
Intact cells
Single cell gating #2
Young
Old
Gating controls
Quiescent cells
SSC-A
FSC-A
FSC-H
DAPI - A
DAPI - W
Ki67 - APC
Scatter
43.8
Single cells
94.7
Cells
69.2
Single cells 2
99.7
Ki67 positive
17.0
Scatter
48.3
Single cells
93.8
Cells
67.5
Single cells 2
99.2
Ki67 positive
3.74
Ki67 positive
0.22

Fig. S13. FACS gating to assess qNSC activation *in vitro*.
FACS gating strategy to assess the ability of young and old quiescent NSCs to activate *in vitro*. Quiescent (non-proliferating) NSCs were used as negative control for the proliferation marker Ki67. The cell population on which each respective FACS gating was done is indicated above each plot.

Figure S14

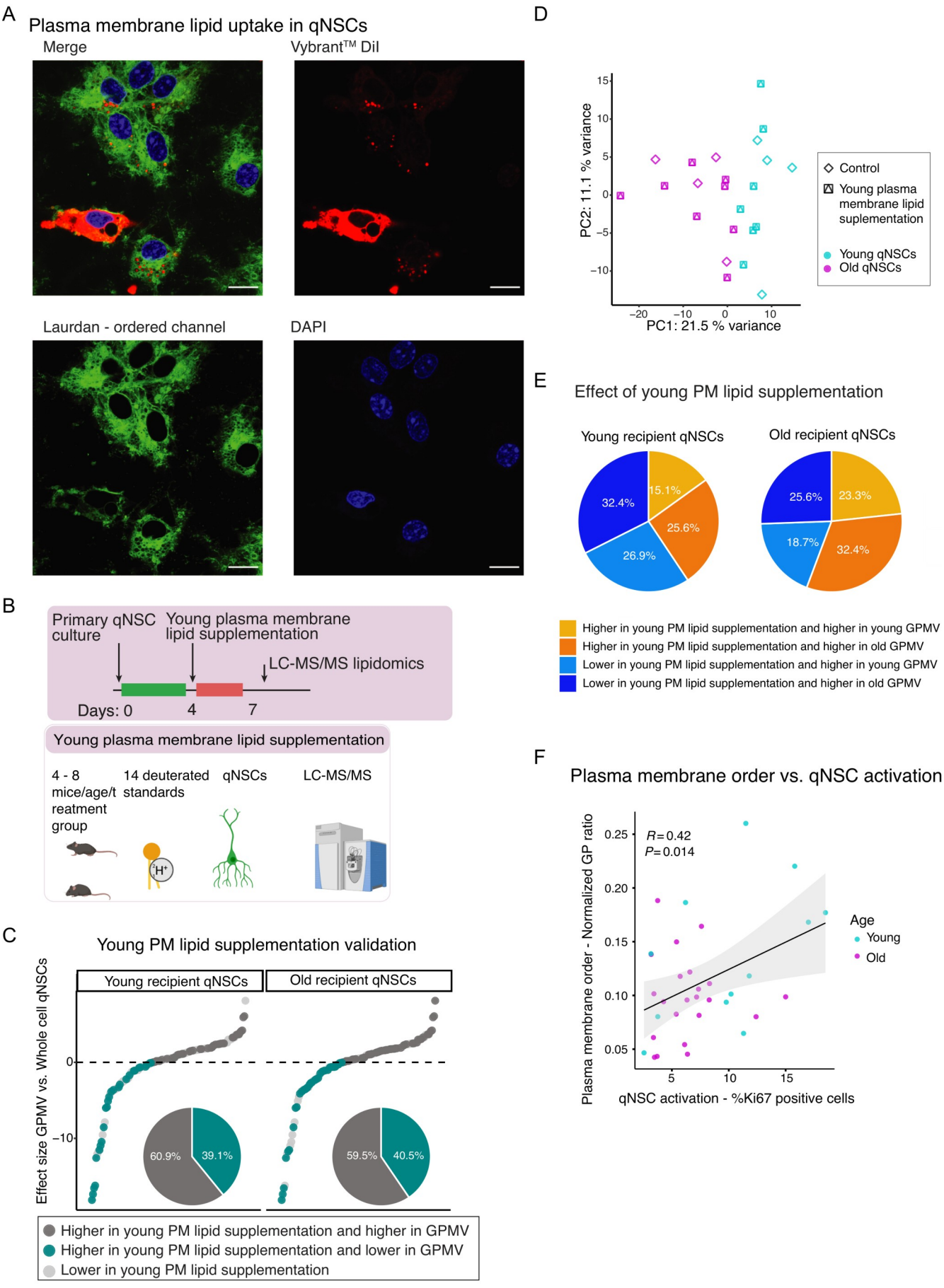
A
Plasma membrane lipid uptake in qNSCs
Merge
Vybrant™ DiI
Laurdan - ordered channel
DAPI
B
Primary qNSC culture
Young plasma membrane lipid supplementation
LC-MS/MS lipidomics
Days: 0
4
7
Young plasma membrane lipid supplementation
4 - 8 mice/age/treatment group
14 deuterated standards
qNSCs
LC-MS/MS
C
Young PM lipid supplementation validation
Young recipient qNSCs
Old recipient qNSCs
Effect size GPMV vs. Whole cell qNSCs
60.9%
39.1%
59.5%
40.5%
Higher in young PM lipid supplementation and higher in GPMV
Higher in young PM lipid supplementation and lower in GPMV
Lower in young PM lipid supplementation
D
PC2: 11.1 % variance
PC1: 21.5 % variance
Control
Young plasma membrane lipid suplementation
Young qNSCs
Old qNSCs
E
Effect of young PM lipid supplementation
Young recipient qNSCs
Old recipient qNSCs
32.4%
15.1%
25.6%
26.9%
25.6%
23.3%
18.7%
32.4%
Higher in young PM lipid supplementation and higher in young GPMV
Higher in young PM lipid supplementation and higher in old GPMV
Lower in young PM lipid supplementation and higher in young GPMV
Lower in young PM lipid supplementation and higher in old GPMV
F
Plasma membrane order vs. qNSC activation
R=0.42
P=0.014
Plasma membrane order - Normalized GP ratio
qNSC activation - %Ki67 positive cells
Age
Young
Old

Fig. S14. Supplementation of plasma membrane lipids from young cells boosts the activation ability of old quiescent neural stem cells.
(A) Representative confocal fluorescence images of primary qNSC cultures after plasma membrane lipid supplementation for 72 hours. Cells were imaged with Laurdan rigid wavelength (green), lipophilic dye Vybrant™ DiI for labelling lipid extract (red), and DAPI (blue). Scale bar: 10μm. Labelled supplemented lipids were found in puncta, indicating successful uptake by the cell through the endocytic system. Endocytosed lipids can then be used by different compartments, including plasma membranes. Excess intracellular Vybrant™ DiI can diffuse laterally and stain the entire cell. **(B)** Experimental set up for lipidomics on plasma membrane lipid supplementation of recipient qNSCs. Primary qNSC cultures (recipient cells) from n=4-7 young (3-5 months) and n=4-7 old (20-22 months) mice were induced into quiescence for 4 days and then supplemented with young plasma membrane lipids for 3 consecutive days. Cells were then harvested for untargeted lipidomic analysis by LC-MS/MS. Number of animals used, number of internal deuterated lipidomic standards used and lipidomic platform (LC-MS/MS) are indicated. **(C)** Validation of plasma membrane lipid supplementation by lipidomic analysis. Individual lipids (individual dots) are ranked based on the effect size calculated between GPMV lipidomic dataset (**Fig. 3**) and whole cell lipidomic dataset in young and old qNSCs (*In vitro* #1, **Fig. 1**). Lipids are color-coded based on whether they have a lower abundance (light grey) or higher abundance in cells supplemented with young plasma membrane lipids. The latter group is further labelled based on whether they are more abundant (dark grey) or less abundant (dark green) in GPMV than whole cell extract. Pie chart summarizes the percentage of 2 categories of lipids that has a higher abundance in cells supplemented with young plasma membrane lipids. **(D)** Principal component analysis (PCA) on log2 transformed concentration of all lipids from young (cyan) and old (purple) cultures with (square with triangle inside) or without (diamond) young plasma membrane lipid supplementation. n=4-7 primary cultures. **(E)** Effect of plasma membrane lipid supplementation by lipid category. Pie chart summarizing the effects on lipids following young plasma membrane (PM) lipid supplementation. Percentage of lipids in the following 4 categories are shown: Higher in young PM lipid supplementation and higher in young GPMV, Higher in young PM lipid supplementation and higher in old GPMV, Lower in young PM lipid supplementation and higher in young GPMV, Lower in young PM lipid supplementation and higher in old GPMV. **(F)** Correlation between plasma membrane order and activation in young and old qNSCs upon plasma membrane lipid supplementation. Pearson correlation was performed on generalized polarization ratio (GP ratio) from Laurdan staining, and percentage of qNSCs that activate (% Ki67 positive) from each individual young qNSC culture (cyan dots) or old qNSC cultures (purple dots) with plasma membrane lipid supplementations. *R* and *P*-values from Pearson correlation are shown. Linear regression line (black line) with 95% confidence interval (gray shade) is shown.